UNIVERSITAT POLITÈCNICA
DE CATALUNYA
BARCELONATECH

Contributions to Radio Frequency Interference Detection and Mitigation in Earth Observation

Ph. D. Thesis Dissertation

By
Giuseppe Francesco Forte Véliz
Dept. of Signal Theory and Communications
Universitat Polytechnic de Catalunya – Barcelona Tech.

Barcelona, April 2014

Advisor:
Prof. Adriano José Camps Carmona
Dept. of Signal Theory and Communications
Universitat Politècnica de Catalunya – Barcelona Tech.

Acknowledgements

This work has been supported by the Spanish National Research and EU FEDER Projects TEC2005-06863-C02-01, and AYA2008-05906-C02-01/ESP, MIDAS 6 AYA2010-22062-C05-05, AYA2011-29183-C02-01, and MIDAS 7 (AYA2012-39356-C05-01).

I want to thank you Prof. Adriano Camps, for the opportunity he gave me to do my Ph. D. thesis in the remote sensing group. His great experience, dedication and support guided me well to complete this work. Also want to thanks for financial support that he and Mercé Vall-llosera dedicated to accomplish this project.

My gratitude to Jorge Querol, all his collaboration in developing, implementing and testing the different RFI detection and mitigation methods were vital to this work.

Thanks also to José Miguel for taking the time to introduce me to the RFI detection and mitigation topic.

Thank you also to Joaquim Giner, Josep Pastor, Rubén Tardío and Albert Marton, for their support in all the mechanical and circuit fabrication for all the developed instruments.

My gratitude also to my lab colleagues: Isaac, Alberto, Raúl, Fran and Dani, for all the support received all the time.

Special thanks to all the people in the remote sensing lab, especially to: Roger, Santi, Ali, Enric, Hyuk, Hugo, Xavi Bosch, Neri, Domenico, Vicente and Albert Aguasca, for helping me in different ways during these years.

Thank you also to Aynie, Teresa, Alicia, Josep M. Haro and Jordi Guillem for all their help solving administrative and computer problems.

Thanks to all the people that give me support in all these years, and thanks God that I had finished this venture.

Dedicated to my family,
for all the encouragement and help
given to me during all this time.

I also dedicate it to everyone that contributed
in any way to the conclusion of this work.

Preface

Radio Frequency Interference (RFI) is becoming a common problem for electronic systems. Unwanted electromagnetic radiation can harm the measurements taken from very sensitive instruments, such as microwave radiometers or navigation systems, and the accuracy and precision are compromised. A first step to mitigate those unwanted effects requires to study the properties of RFI. Different algorithms have been proposed to detect the interferences, but there is no method that works well in all cases.

The scope of this dissertation is the design, implementation and testing of different detection and mitigation methods in real-time. First, an evaluation of the existing RFI detection algorithms is performed at different radiometry and GNSS bands with real data gathered in the city of Barcelona, Turò de l'Home mountain (Montseny), and in the laboratory using an adhoc RFI generator designed and manufactured for this purpose. The surveys carried out and the characterizations of RFI sources have helped to optimize the current mitigation techniques. Then, real-time RFI mitigation hardware systems have been implemented for radiometry and navigation and a circuit to allow navigation receivers to continue operational under the effects of a jammer has been successfully implemented.

Contents

Chapter 1

INTRODUCTION

"Radio Frequency Interference (RFI) is the effect of unwanted energy due to one or a combination of emissions, radiations, or inductions upon reception in a system, manifested by any performance degradation, misinterpretation, or loss of information which could be extracted in the absence of such unwanted energy" [1].

The magnetic field strength is proportional to current, and it is also a function of the loop area defined by the conductors carrying that current. All circuits are somehow loops, even those with high impedance and low Direct Current (DC) inputs. The rapid charge and discharge of the loops formed by the transmission lines generate Electromagnetic Interference (EMI). With an increase of the loop size, a stronger magnetic field could be radiated, and it is more prone to create interferences [2].

As the signal frequency increases, grounding becomes critical to avoid RFI because more intense electromagnetic fields are present, and higher frequencies are radiated

more efficiently. This energy can escape from the circuit being radiated into space or being conducted in a cable. Enclosing the circuit in a grounded metal enclosure can block radiated emissions, but many commercial systems don't take care of energy escaping through slots and holes [2].

Good filtering between the active circuitry and the cable connector can deal with interferences conducted on those cables, but not implementing it converts the system into an RFI generator.

In Earth observation, the systems most affected by RFI are the passive ones, because their high sensitivity to the very weak signals received. In this work, the RFI problem and solutions are described for Global Navigation Satellite Systems (GNSS), and Microwave Radiometers, but most of the techniques could be applied to RFI problems in general, such as radars or communication systems. Actually, many of the studied techniques were first applied to radioastronomy.

1.1 INTERFERING SIGNALS

1.1.1 GNSS interfering signals

RFI is a significant problem for GNSS users. They are especially vulnerable to RFI because the signals from GNSS satellites are very weak when they arrive to the user. Signals that overlap the GNSS frequency bands are likely to come from transmitters much closer than the satellites and they can easily override the GNSS signals making them unusable.

There are three types of GNSS interferences:

- Naturally occurring, such as the solar storms or atmospheric parasitics.
- Unintentional, such as bad filtered signals that disturb GNSS signals.
- Intentional, such as deliberated jamming.

The problem with jamming is that GNSS satellites are very far from receivers location (more than 20,000 km, altitude for GPS case) and jammers are much closer so they need much less power to disturb the satellite signal, for example a 0.5 W Coarse/Acquisition (C/A) code jammer or a 5 W Precision (P) code jammer could interfere up to 5 km.

While jamming prevents a receiver from acquiring GNSS signals, spoofing fools the receiver's position or time, making it believe that is somewhere or sometime it is not.
Most common jamming sources are the so called Personal Privacy Devices (PPDs) and powerful signals in adjacent channels.
Reasons for jamming and spoofing can be:

- "Privacy": such as the Newark airport case [3], where a truck driver trying to avoid being tracked deliberately used a commercial jammer of 200 mW, and accidentally interfered with the airport Ground Based Augmentation System (GBAS) system.
- Financial: such as spoofing time for banking transactions or car thieves using jammers in order to avoid being tracked.
- Terrorist: is not a very likely reason, at least publicly reported, but spoofing bank transactions or jamming transport navigation signals or critical infrastructure can cause big problems.
- Military: denial of navigation to the enemy or to create confusion amongst them.

To mitigate this problem, many options have been proposed such as government programs to chase and punish these infractions, but our focus will be in the technological ones to provide the tools to locate and/or mitigate their source:

- Anti-jamming systems to analyse the interferences and subtract them from the received signal.
- Consistency checks with other navigation sensors like accelerometers, magnetometers, gyroscopes, cellular network, wireless networks, etc.
- Anti-spoofing systems based on signal spatial correlation [4].
- Three dimensional time and spectrum mapping, in order to locate the directions of the interferences or even the position by using two different positions for the survey.
- Crowd-sourcing exploiting the benefit of the massive use of smartphones that could include GPS Jam-to-Noise (J/N) ratio detectors. Having measurements from several cell phones, jammer's location can be estimated by estimating the centroid of the measured jamming power as a function of the observer positions [3].

1.1.2 RFI in Microwave Radiometry Measurements

Microwave Radiometers measure geophysical parameters from the thermal noise radiated by bodies in the microwave part of the spectrum. Therefore an RFI changing the detected power level leads to an erroneous measurement. Since the thermal noise measured is a very weak signal, even a very small RFI can make the acquired data useless.

Although passive remote sensing has "protected" frequency bands, communications in adjacent bands, out-of-band emissions, and spurious signals from other bands degrade the quality of the measurements.

A very good example of this is the Soil Moisture and Ocean Salinity (SMOS) RFI contamination case. SMOS is operating at L-band, in the "protected" window from 1400 to 1427 MHz. However, interferences from harmonics (e.g. 700 MHz UHF TV band), radars transmitting very close in frequency (e.g. 1300 to 1400 MHz), and not being filtered appropriately have led to a reduction of the instrument's sensitivity. RFI sources are located, but measurements in those places become useless, unless the sources are shut down. In Fig. 1.1a [5] shows a brightness temperature map and the locations where it cannot be retrieved because of the RFI. In Fig. 1.1b [5] the probability of RFI is shown.

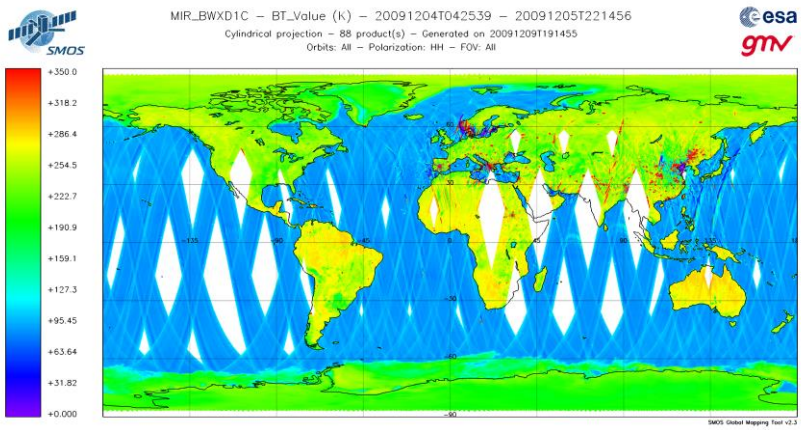

a.

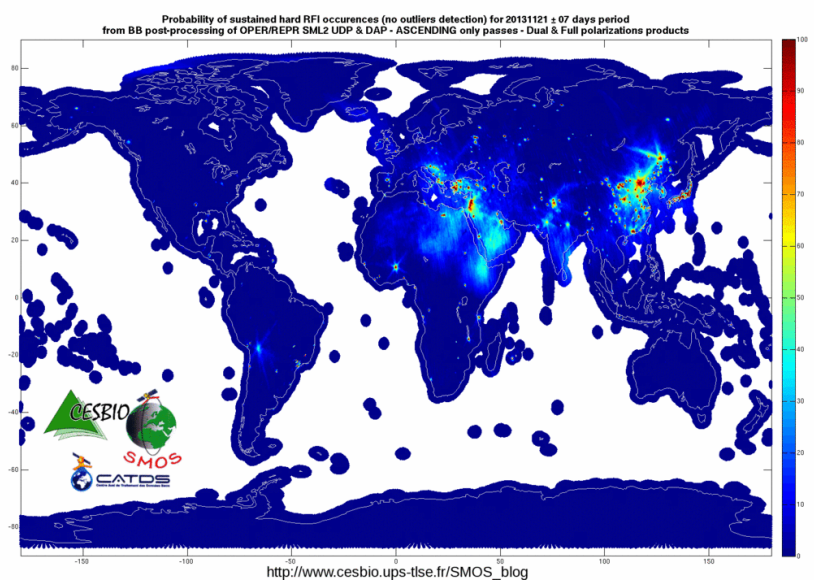

b.

Fig. 1 SMOS maps (from [5]): a) Retrieved brightness temperature map from SMOS. b) Probability of RFI in SMOS observations.

1.2 RFI SIGNAL CHARACTERIZATION

To mitigate the RFI, a study of its properties is required first. The most common properties are its power in the time and frequency domains, and for the application of statistical techniques. Another important parameter is to know the direction of the RFI source. Many surveys have been performed during this work, including space, time and frequency in different bands. Those surveys are presented in Chapter 3. The first surveys present the probability of RFI in the protected L and X bands, one month per each band. Directional surveys have also been carried out by mounting antennas on a motor controller and capturing their data in different azimuth directions. Another one was carried out using the Multi-frequency Experimental Radiometer with Interference Tracking for eXpEriments over Land and the Littoral (MERITXELL) radiometer explained in Appendix A.4, which includes frequency "protected" bands from L to W in different directions.

Jammers are a big threat as explained before, so a study of their signal type and output power in time and frequency presented in Chapter 2 have led to the anti-jamming

device designed and explained in Chapter 5. Jammers for telemetry, GNSS, and mobile phones have been studied. As a further step, at the end of Chapter 2, an RFI emulator for unintentional RFI characterization has been designed and implemented.

1.3 RFI DETECTION AND MITIGATION TECHNIQUES

Radio Frequency Interference (RFI) includes spurious signals and harmonics from lower frequency bands, spread-spectrum signals overlapping the "protected" band of operation, or out-of-band emissions not properly rejected by the pre-detection filters due to their finite rejection. The presence of RFI increases the detected power and therefore the estimated antenna temperature, leading to a degradation of the accuracy of the retrieved geophysical parameters, if they can be retrieved at all. RFI is an especially serious problem in populated land areas [6–12], although due to different spectrum regulations not all bands are affected the same way in all regions.

It is important to note that many of these methods were first devised in radio-astronomy, where RFI problems were first experienced [13-15].

Current RFI detection and –eventually– mitigation methods in remote sensing include:

1.3.1 Time-Domain

Time-domain techniques try to search for RFI components concentrated in determined parts of the time domain which present a higher power value than the clean signal. These algorithms are effective when dealing with short high power bursts of RFI. High frequency sampling and appropriate thresholding usually gives good results. However, when RFI is comparable or smaller than the noise power, it becomes more complicated to detect by thresholding and the estimated power is erroneous. An additional problem appears because the detected power is an averaged version of the instantaneous one, if the duration of the RFI peaks is shorter than the integration time they may pass undetected.

In microwave radiometry, this technique also has been used to detect and eliminate pulsed RFI in [9]; although the time-domain RFI detection algorithms are usually combined with frequency-domain RFI detection algorithms because interference may be any kind of signal [10]. A clear example of Time-domain RFI mitigation is shown

in Fig. 1.2, from t = 8 s to 14 s all data is eliminated ("blanked"). The eliminated signal during that time corresponds to a nearby CDMA mobile phone jammer being turned on.

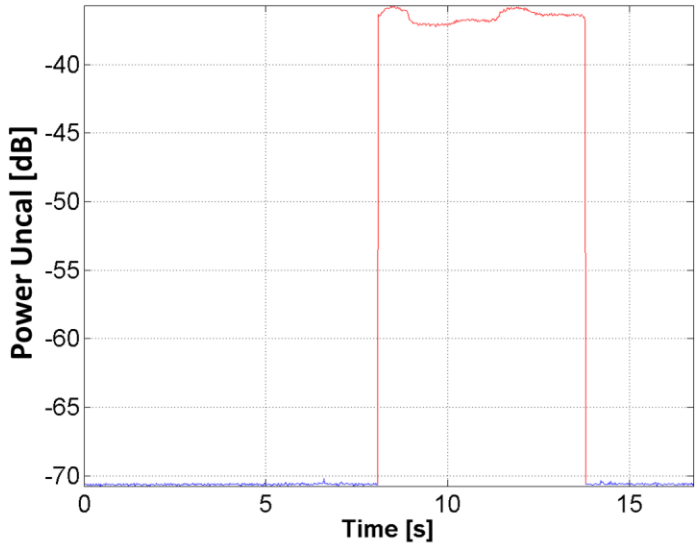

Fig. 1.2 Sample time-domain detection and mitigation of a CDMA jamming signal at 869 MHz with a bandwidth of 100 MHz. In red the removed data in time, and in blue the remaining signal.

Another example is shown in Fig. 1.3, where pulsed RFI, probably coming from the Barcelona airport radar, increases the total power captured by the LAURA 2.0 radiometer installed at Turò de l'Home located at Barcelona province (this system will be explained in detail in Chapter 3). Note that the LAURA radiometer front-end filters emissions out of the 1400 – 1427 MHz protected band.

1.3.2 Frequency-Domain

These RFI detection techniques are more complex than the ones in the time-domain, because a subbanding process is necessary. The technique consists of blanking sub-bands with power values larger than a pre-defined factor of the expected variance [9]. Therefore RFI signals narrower than the resolution bandwidth, but with an average power within the expected natural variability may pass undetected. An example of RFI

detection and mitigation is shown in Fig. 1.4 where the spectrum of a GSM jammer signal is blanked.

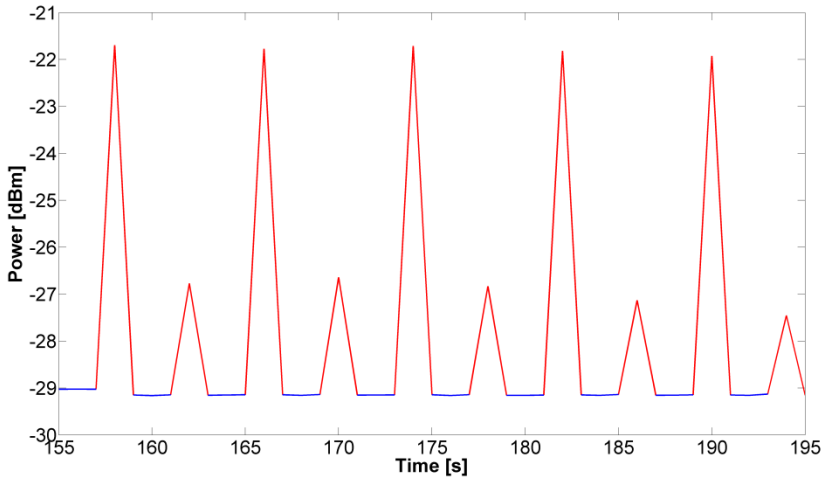

Fig. 1.3 Time-domain detection and mitigation for pulsed signal. One sample per second. In red the removed data in time, and in blue the remaining signal.

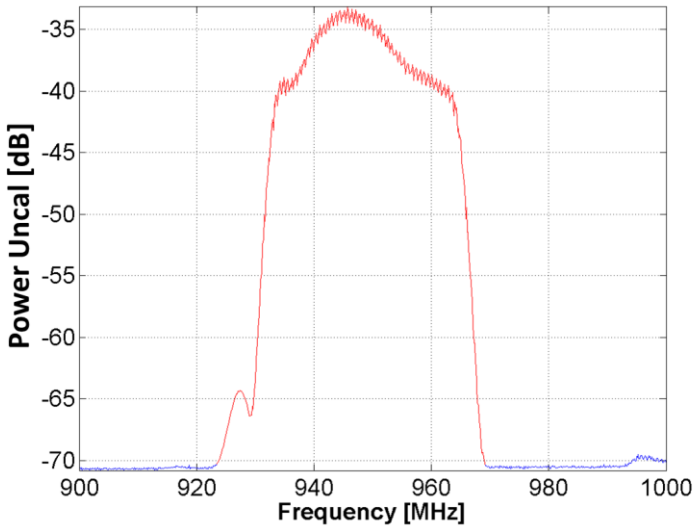

Fig. 1.4 Frequency-domain detection and mitigation for a GSM jammer interference. In red colour is the removed bandwidth, and in blue colour the remaining signal.

1.3.3 Spectrogram Techniques

Spectrogram techniques make use of image processing techniques such as the edge detection [10], and the smoothing algorithms [11] to detect the presence anomalous

features of clusters of high power time-frequency bins, which are then blanked. The image is the intensity plot of the Short-Time Fourier Transform (STFT) magnitude. The advantage of the spectrogram technique over time- or frequency domain methods is that the RFI is removed only from the occupied frequencies at the specific time they occur, and not the entire frequency band or time segment.

In the three previous cases, the signal power (observable in microwave radiometry) is estimated from the remaining (non-blanked) signal samples, sub-bands, or time-frequency bins, properly scaled. However, if the RFI lasts longer than the integration time, it extends over the whole bandwidth, or extends over the whole observation time and frequency span, it leads to an error in the estimation of the power variance and the detection threshold. Figure 1.5 shows the power of the spectrogram technique, eliminating only the RFI present in Fig. 1.5a, and removed in Fig. 1.5b. A GPS jammer covering different bands in different times is detected and mitigated.

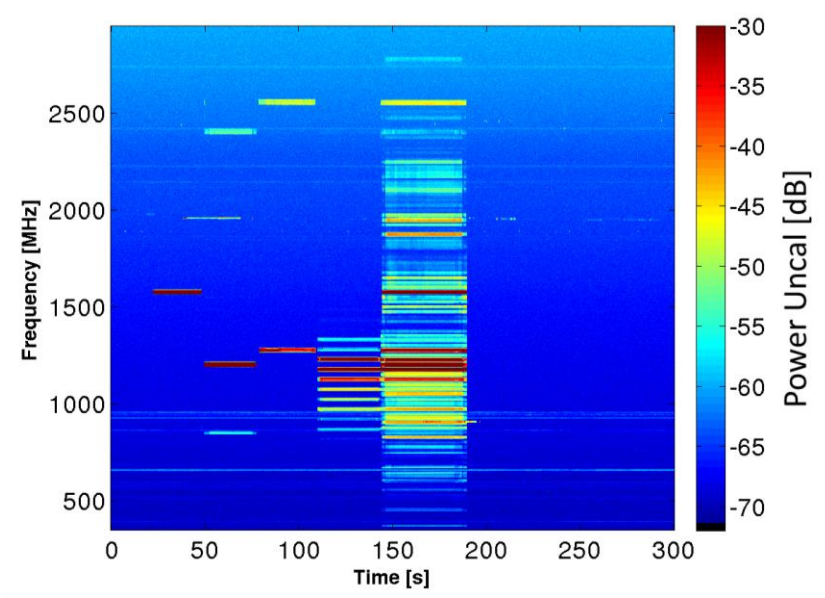

a)

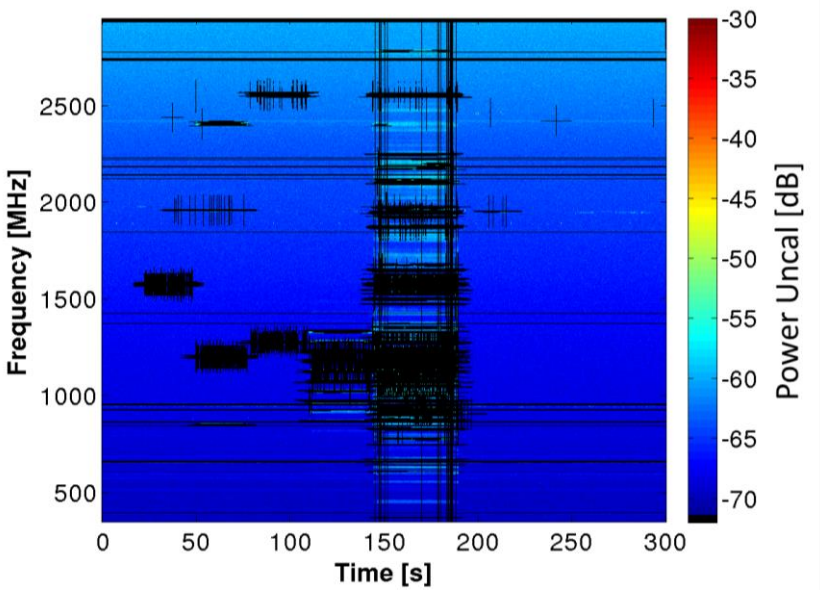

b)

Fig. 1.5 Spectrogram RFI detection and mitigation for multiple jamming signals: a) Original Spectrogram, b) Removed interferences.

1.3.4 Statistical Techniques

They are based on the fact that the RFI-free radiometric signal should be a zero-mean random Gaussian variable. Therefore, the probability density function (PDF), and the statistical parameters are perfectly known. If the normality test is not passed, the whole sequence is eliminated. There are many statistical tests, they are categorized as:

1. the properties of the statistical moments: e.g. the Kurtosis (K) [12], the skewness (S), the Jarque-Bera (JB) [16-18], or the D'Agostino K-square (K^2) test [19], or
2. the comparison of the Empirical Distribution Function (EDF) with a normal distribution: e.g. the Lilliefors (L) [20], the Anderson-Darling (AD) [21, 22], the Shapiro-Wilk (SW) [23-25], the Cramer-von Misses (CM) [26], the Lin-Mudholkar (LM) [27-29], or the Chi-square (χ^2 or CHI2) [30] tests.

In remote sensing literature, the Kurtosis (ratio of the fourth moment and the square of the second moment) method is the most widely test used, and there are time- and

frequency-domain versions of it [12, 31 and 32].

The Kurtosis is a statistical parameter defined as the 4th central moment normalized by the square of the 2nd central moment (variance):

$$K = \frac{\mu_4}{\sigma^4} = \frac{E[(X - E[X])^4]}{E[(X - E[X])^2]^2}\ , \tag{1.1}$$

where μ_4 is the fourth order moment of random process X, and σ is the standard deviation of random process X, and $E[]$ is the expectation operator. This statistical parameter has the property of having a value equal to 3 for Gaussian-distributed signals, and it is usually different from 3 for non-Gaussian signals [12]. However, it presents blind spots for some particular signals, for which the Kurtosis is also 3. In order to overcome this limitation, other methods have been studied such as the sixth order moment [33], or the Shapiro-Wilk tests [34]. Although a known limitation of this last method is the limited sample size ($N \leq 2000$) [35], longer sample lengths can only be tested by splitting the sequence in several shorter length sequences. In [36] a throughout analysis of these, and other normality tests are studied, proposing a combination of the Kurtosis and the Anderson-Darling tests as a combo test to overcome the blind spots.

The performance of the different methods is characterized by two parameters:

A. Probability of false alarm (P_{fa}), or the "detection" of RFI in the absence of RFI (*Type I error* or rejection of a true hypothesis), which leads to the blanking of correct data.

B. Probability of missed detection (P_{miss}), or "no detection" of an RFI when there is RFI present (*Type II error* or acceptance of a false hypothesis), which leads to an erroneous measurement. In our context the term probability of detection (P_{det}) is usually used and it is defined as $P_{det}=1 - P_{miss}$.

The objective is to obtain a low P_{fa} and a high P_{det}, but since both are strongly correlated, setting the value of one determines the value of the other one. To achieve a low P_{fa}, the threshold used to determine the "presence of RFI" must be high enough, but then many RFI are not detected, and P_{miss} increases. The combined performance of a given technique in terms of P_{det} and P_{fa}, depends on the probability density function (PDF) of the signal values, and it is given by the so-called Receiver Operating Characteristic (ROC) [36]: P_{det} =ROC(P_{fa}(*threshold*)).

1.3.5 Polarimetric Techniques

They look for anomalous signatures in the third and fourth Stokes parameters, and, if found, the corresponding first and second Stokes parameters are discarded. These techniques have been applied to both real [5] and synthetic aperture radiometers [37, 38]. All data is lost when RFI is detected and blanked.

1.3.6 Suppression Using Filtering Techniques

They can eliminate temporally spread and strongly correlated RFI based on the estimation of the RFI waveform (using any available filtering technique like spline-smoothing, Wiener filtering, wavelet denoising, and parametric identification), and subsequent subtraction it from the received signal.

$$\hat{x}_{CLEAN}(t) = x(t) - \hat{x}_{RFI}(t), \tag{1.2}$$

where $x(t)$ is the received signal, $\hat{x}_{RFI}(t)$ is an estimation of the RFI waveform included in the received signal, and $\hat{x}_{CLEAN}(t)$ is the estimated thermal noise only signal, free of RFI components.

A powerful filtering technique is Wavelet analysis is based on multi-resolution analysis [39]. Signals are decomposed into localized component waves of variable duration (wavelets). A discrete signal f is first decomposed into a first trend a^1, and a first fluctuation d^1: $f \rightarrow (a^1 \mid d^1)$. Then, in the second step (or level) the first trend a^1 is decomposed again into a second trend a^2, and a second fluctuation d^2: $f \rightarrow (a^2 \mid d^2 \mid d^1)$.

The process is repeated a number of steps L (levels): $f \rightarrow (a^L \mid d^L \mid d^{L-1} \mid d^{L-2} \ldots \mid d^2 \mid d^1)$. By ordering the wavelet transform coefficients by decreasing magnitude, signal compression and denoising can be performed by neglecting (or attenuating) the amplitude of the coefficients below a given threshold.

In this case, there is no signal loss, although some residual RFI may be present. Its performance depends mainly on the ratio of the sampling frequency to the signal bandwidth, the interference-to-noise ratio (INR), the wavelet family, and decomposition level. A full explanation of this method and its hardware implementation is presented in Chapter 4.

1.3.7 Adaptive Interference Cancellation Using Reference Channels

A separate, dedicated reference channel is used in order to obtain an independent estimate of the RFI signal. This technique has been widely used in digital signal processing, and it is known as adaptive noise cancellation [40].

Figure 1.6 shows the basic problem and the application of this technique. There are two data channels: a main channel pointing to the source and containing the RFI signal; and a reference channel (separated antenna pointing off source) that contains also the RFI signal. Both channels contain the RFI signals, which are different due to the different propagation paths, but correlated as they come from the same source, making it possible to eliminate the RFI from the received signal [41].

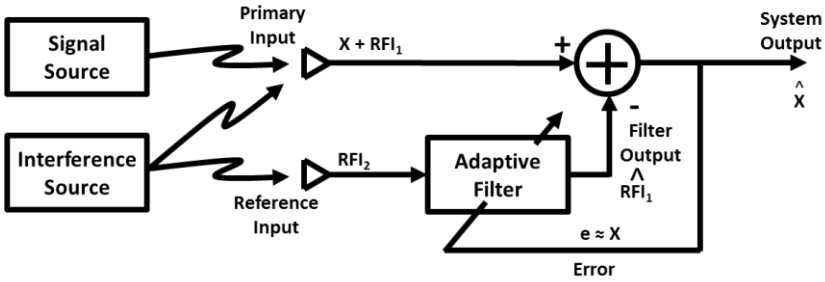

Fig. 1.6 Adaptive noise cancelling concept (adapted from [36]).

This procedure can be applied both in the time domain (adaptive filtering) and in the frequency domain (FFT → adaptive filtering in each frequency bin → FFT^{-1}). This kind of RFI cancellation is especially useful when the RFI and the signal of interest occupy the same frequency domain.

1.3.8 Spatial Filtering Using Multi-Element Systems

Spatial filtering methods use the difference in the Direction-of-Arrival (DOA) of the signal of interest and the RFI. The RFI emission from spatially localized sources could be suppressed using multi-element radio interferometers based on an adaptive array philosophy, forcing the zeroes of a synthesized antenna pattern to coincide with the DOAs of undesirable signals (adaptive nulling). However, usually RFI sources will

not be localized in only one point in the space; hence this method will work with a maximum number of RFI sources.

Another way of RFI cancellation is the RFI estimation by means of the combination of the complex spectra of the different antennas. Then, this RFI estimation is removed from the received signal. This method is very similar to the method presented in the paragraph 1.3.7, but assuming a larger number of reference channels.

This technique can be used in interferometers, beamforming arrays, and anti-jamming systems like Novatel/QinetiQ GAJT-700ML system [42]. The GAJT-700ML mitigates the jamming thanks to an antenna array that creates up to six independent nulls in the direction of the jammers. With the jammer nullified, the receiver is clear to acquire, and track the GPS signals.

This technique has been used firstly in radioastronomy [43], and later in radiometry a DOA RFI detection algorithm has been proposed in [44].

1.3.9 Crowd-Sourcing

The wide spreading of smartphones with GNSS capabilities and connected to the internet make them a great tool for detecting interferences, more specifically the ones affecting GNSS. Even though the individual measurements are of poor accuracy, the crowd consensus yields good accuracy. The concept is proposed in [45], and its feasibility is analysed in [3], the explanation here is taken from those two references.

There are numerous advantages to RFI situational awareness in a GNSS receiver design. One unique advantage is that it provides the noise floor information required to perform an adaptive initial search and acquisition process. The design continues to operate even when the RFI level is so high that the GNSS receiver is unable of acquiring and tracking satellites, an RFI situation that cannot be determined by most of today's GNSS receivers, even most military receivers. This robustness in RFI situational awareness measurement permits the GNSS receiver to inform the user that it will most likely be unable to acquire the signals and why.

The jamming measurement is obtained by the measurement of the GNSS receiver RF front-end gain using measurements obtained from the automatic gain control (AGC). The preferred embodiment of the jamming meter is the digital gain control of the

AGC. This gain control is derived from the analogue-to-digital converter (ADC) process that normally occurs at the intermediate frequency (IF) of the GNSS receiver. In the absence of RFI, the AGC gain is set by the thermal noise power level (*N*). The digital value of *N* becomes the jamming reference level; not the GPS satellite signal power (*S*), which is well below *N* at the IF. When RFI occurs, the digital gain control acts to attenuate the gain of the AGC amplifier in order to keep the RMS amplitude of the AGC amplifier output at a constant level. That AGC operating point is normally selected to provide the least amount of quantization noise in the ADC that follows the AGC. In the presence of RFI, the new digital value is now a measure of the jamming power (*J*) plus *N*. This can be converted to a useful measure of the RFI level called the jamming-to-noise power ratio (*J/N*). Therefore, the AGC digital gain control reading can be a *J/N* meter as a natural by-product of the AGC gain control. The *J/N* meter technique works because the AGC control voltage does not change from the measurement of *N* unless an RFI is present at the IF. The gain of a modern AGC amplifier is linear in decibels (dB), so reading the AGC digital gain control value provides a precise linear measurement in dB of the RFI power level, thus providing RFI situational awareness. An estimate of *J/S* can be made from this measurement assuming a uniform level of *S* for all satellites plus certain GNSS receiver front-end parameters. The estimation of *J/S* from the measurement of *J/N* cannot account for differences in *S* for each satellite, but if the initial search fails, and the *J/N* meter says that RFI is not the problem, and then the receiver can reasonably conclude that the GNSS signals must all be critically attenuated. When and if the receiver is tracking a subset of the GNSS constellation, it can accurately measure the carrier-to-noise power ratio in a 1 Hz noise bandwidth, $C/N_0 = S/N_0$, for each satellite being tracked. It can then estimate *J/S* more accurately for each satellite based on S/N_0 and certain GNSS receiver design parameters.

With this system, a solar event may trigger large numbers of phones, but the flat *J/N* versus location response can be used to rule out a localized jamming event. A real jamming event will tend to have a geographic centre with many high *J/N* values over a fairly restricted area.

1.4 HARDWARE DEVELOPMENTS AND RESULTS

The real-time hardware developments are the novelty of this work because they implement the most promising theoretical models that have been tested only with post processing. There are many advantages of real-time RFI mitigation, for example it can be directly connected between the front-end and the back-end processing blocks, and to be transparent to both. Another advantage is the elimination of contaminated data for post-processing because in many cases that data rate is extremely high for a small measurement time, consuming the resource in a moment and disabling the system for a continuous acquisition. Two systems have been developed: a wavelet-based RFI Mitigation that models the interference and removes it from the received signal explained in Chapter 4, and the anti-jamming system as collaboration with a Master Thesis [46], and explained in Chapters 5.

In Chapter 4, very interesting results have been obtained using the Haar wavelet transform, which can perform detection and mitigation on interferences of more than 30 dB INR, and on very small as -30dB INR, when the provided sampling frequency is high enough.

The results of the anti-jamming system show its capability against commercial jammers, allowing the GNSS receiver to continue acquiring the signal.

1.5 CONCLUSIONS

RFI has become a serious problem to sensitive measuring devices. Their sources are increasing because most of them are originated by human-made electrical devices.

To determine the interferences behaviour, multiple studies have been performed in this work to determine their characteristics, such as duration, bandwidth, incoming direction, estimated power, signal type, etc.

Multiple methods for detecting and mitigating RFI have been proposed, but the optimum way is a combination depending on the interference type.

As a novelty, during this work two types of real-time processing methods have been developed and implemented: wavelet denoise for RFI modelling and subtracting, and the anti-jamming system that removes the jammer's signal in real-time.

Chapter 2

RFI SOURCES CHARACTERIZATION

Personal Privacy Devices (PPDs) are used to avoid being tracked, listened, and watched over different communication channels. Although their use is outlawed in many countries, these systems are widely available at low cost, and seem to increase in number. The way these devices operate is by introducing interferences in the channel. Because the high transmitted power and bad filtering, these devices also affect other bands.

Spark gaps are usually an unintentional RFI source, produced for example by vehicles, DC motors, and many other electric systems. A spark gap generator has also been designed, implemented, and characterized in order to better understand this type of RFI and improve their mitigation.

2.1 COMMON JAMMERS (PPDS) CHARACTERIZATION

A multiple signal generator that emulates some of those devices has been designed and assembled (Fig. 2.1) in order to characterize their nature, and design better counter-measures. The output signals are generated with similar characteristics to the ones used commercially, so the differences are unnoticeable in amplitude, bandwidth, sweep, etc. Due to confidentiality issues, and to prevent potential readers of this public document from reproducing this device for illegal applications, implementation details cannot be provided.

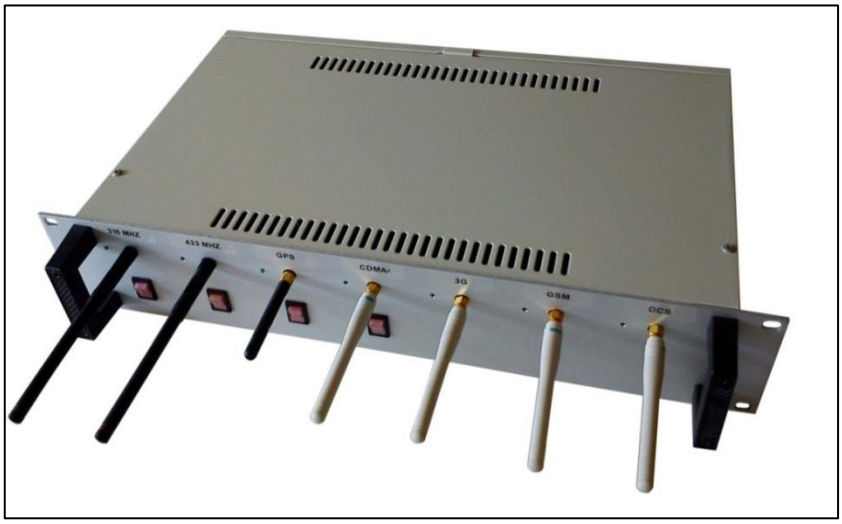

Fig. 2.1 Laboratory multi-band RFI generator for jamming studies. Bands (from left to right): 315 MHz, 433 MHz, GPS L1 (1575, 42 MHz), CDMA (824-896MHz and 1850-1990 MHz), 3G (2100 – 2150 MHz), GSM (806 – 915MHz) and DCS (1710 – 1880 MHz)

A commercial multi-band GPS jammer has also been characterized (Fig. 2.2). The characterization process in the time-domain has been performed by down-converting the emitted signal to baseband, and then sampling it at 50 MS/s with a SMU200 Rohde & Schwarz spectrum analyser in IQ capture mode. For time-domain and frequency-domain simultaneously, the spectrum analyser has been used in spectrogram mode.

Fig. 2.2 TG-121G Commercial available GPS jammer (See Appendix A.5 for details)

In order to avoid interferences outside the testing room, a 60 dB attenuator has been added to the output of this jammer using two 30 dB attenuators in cascade as shown in Fig. 2.3. The characterization is performed using the Rohde and Schwarz ZVL13 analyser in ADC and spectrogram modes. To compare the jamming signal to the legal emissions, two measurements are mixed into one spectrogram for every jammer: 1) a measurement of the legal emissions, and 2) a measurement of the jamming signal in an isolated chamber. The spectrogram is presented with an uncalibrated power scale because both measurements are taken from an antenna.

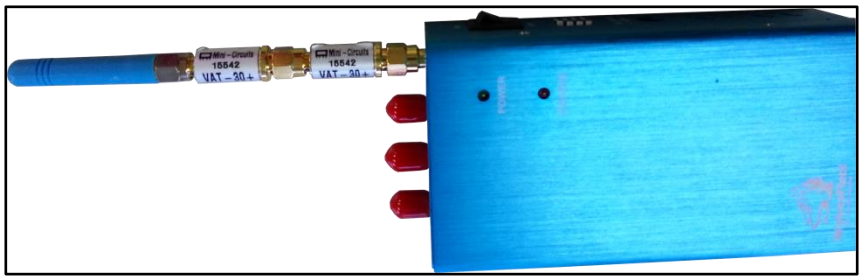

Fig. 2.3 Rohde and Schwarz ZVL13 spectrum analyser receiving the signal from a power splitter with a GPS antenna in one port and a 60 dB attenuator added to the jammer output on the other port.

2.1.1 Telemetry Jammers

Telemetry is used to transmit data and it is widely used for remote control. Examples of jammers at 315 MHz and at 433 MHz are characterized in time, frequency, and both are shown in Figs. 2.4 and 2.5.

In Fig. 2.4a the interfering signal is a sinusoidal signal modulated in amplitude using pulses of random duration and location. The bandwidth occupied is around 10 MHz and the power increase above thermal noise is around 40 dB as seen in Fig. 2.4b.

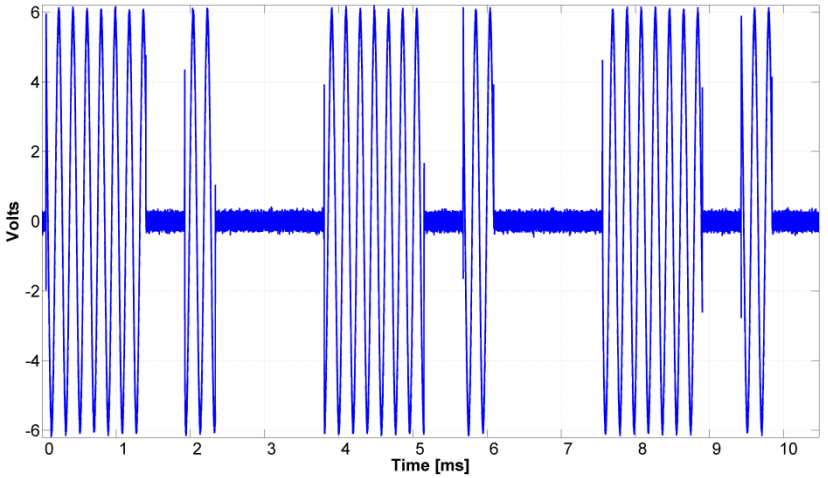

a.

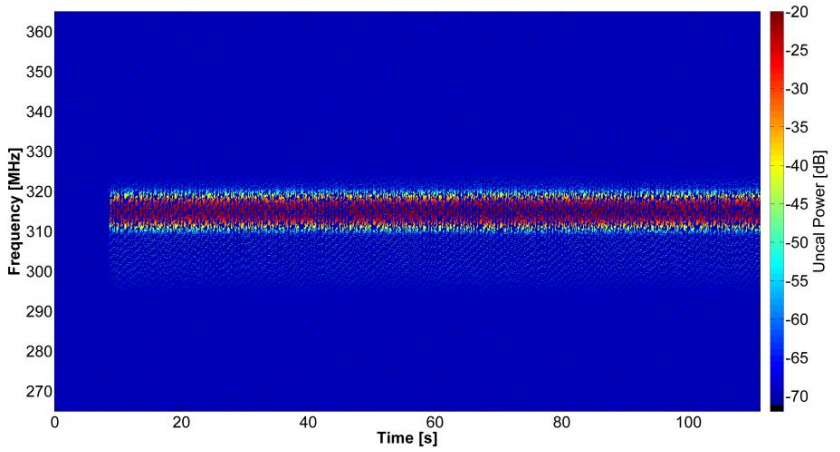

b.

Fig. 2.4 Characterization of a 315 MHz jammer: a) Time-domain signal waveform. b) Spectrogram with uncalibrated power in dB, and Resolution Bandwidth of 3 kHz. Note: jammer is turned on around t = 5s.

In Fig. 2.4 it can be noticed that until 5 s the spectrum is clean, and when the jammer is turned on the interference appears.

Time-domain mitigation will remove almost all the signal, while frequency domain-mitigation will remove around 20 MHz of the bandwidth, almost the same as the spectrogram technique because the jammer is turned on almost all the capture time.

The most effective method here is filtering, and using wavelets to estimate the interfering signal and remove it.

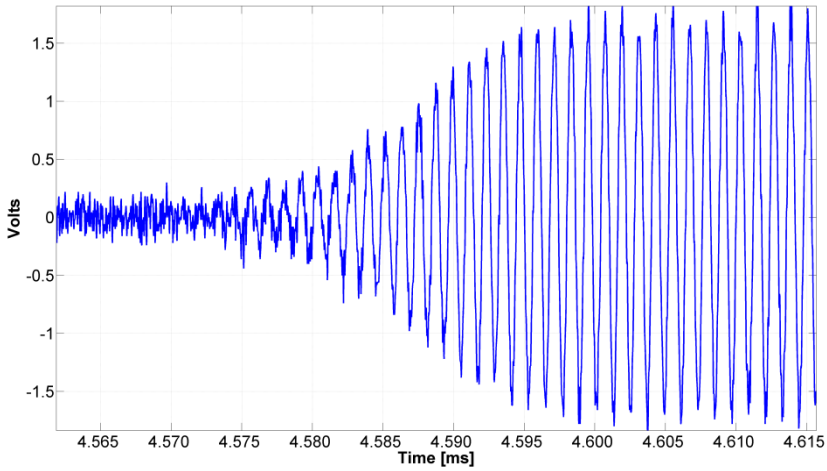

a.

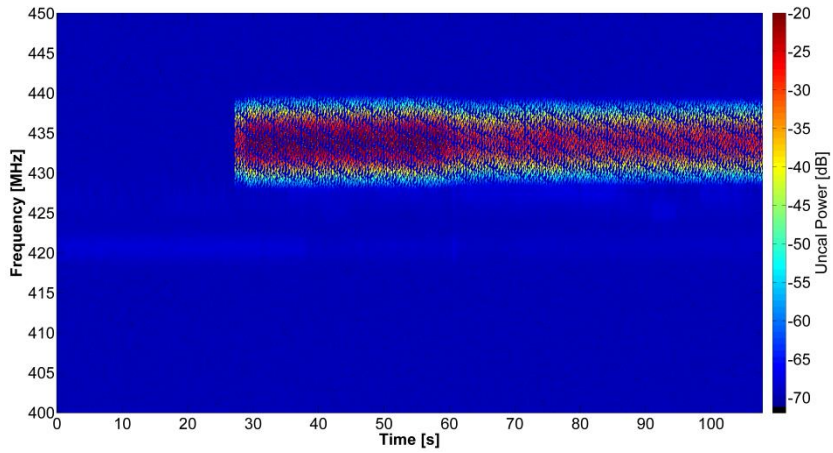

b.

Fig 2.5 Characterization of a 433 MHz jammer: a) Time-domain signal waveform. b) Spectrogram with uncalibrated power in dB, and Resolution Bandwidth of 3 kHz. Note: jammer is turned on at t ≈ 25 s.

2.1.2 GPS Jammers

RFI has been and will continue to be a significant worry for GNSS users, including administrations. Because the signals from GNSS satellites are very weak, by the time that user receives and processes them, they are especially vulnerable to RFI. Signals

that overlap GNSS frequencies are likely to come from transmitters much closer than the satellites and can easily mask the GNSS signals, making them unusable. Many studies have been performed on GNSS jamming [47-50]. In Figs. 2.6 and 2.7 a typical GPS jammer has been characterized. The type of jamming signal is a noisy chirp (FM sweep) as can be seen in Fig. 2.6a. In Fig. 2.6b it can be noticed the power increase over noise level of up to 40 dB, when the jammer is on and off. At this moment, the most efficient method for mitigating GNSS chirp RFI is filtering, as explained in Chapter 5.

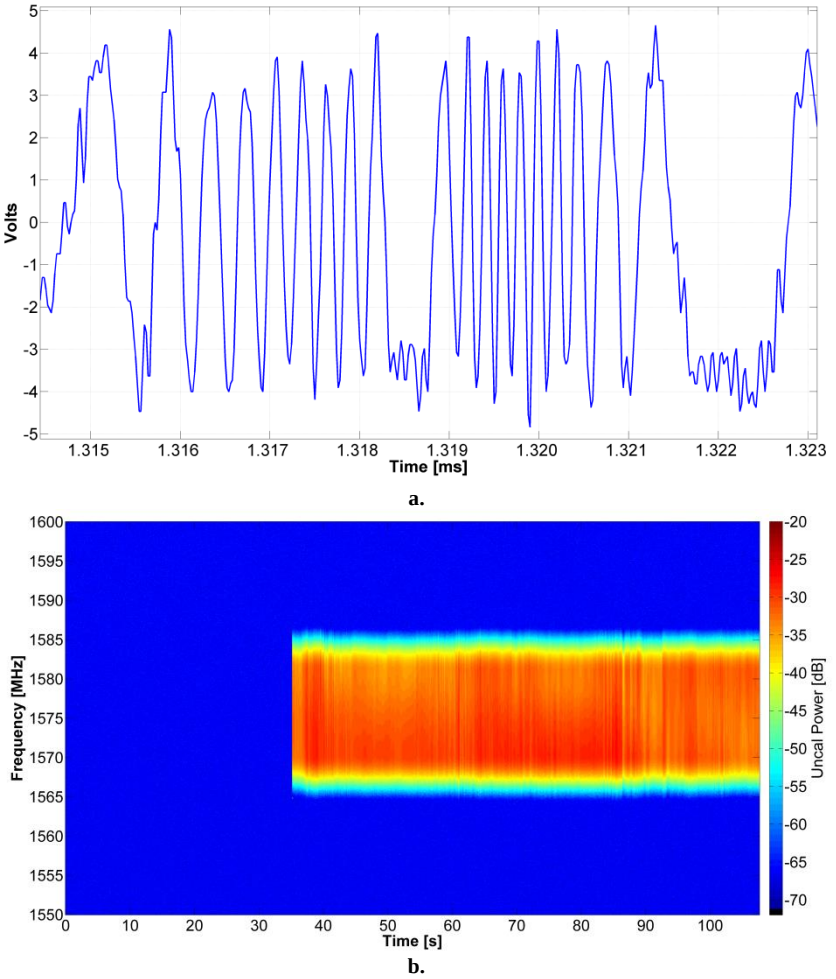

Fig. 2.6 GPS Jammer at L1 1575.42 MHz band: a) GPS L1 jammer signal in time, b) uncalibrated power spectrogram in dB, and Resolution Bandwidth of 3 kHz. Jammer is turned on at t ≈ 35 s.

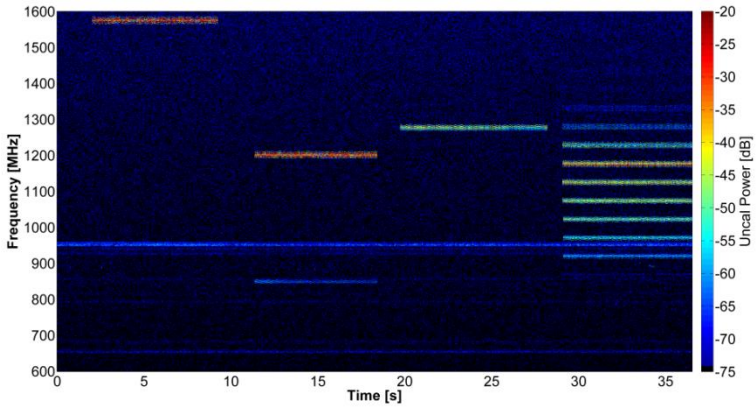

Fig. 2.7 Uncalibrated power spectrogram for GPS Jammer at L1 (1575.42 MHz), L2 (1227.60 MHz), and L5 (1176.45 MHz) bands. Jammers are turned on as follows: L1 from t = 2 s to 9 s; L5 from t = 11 s to 18 s; L2 from t = 20 s to 28 s, and from t = 29 s to 37 s all of them simultaneously.

2.1.3 Mobile Phone Jammers

Mobile phone jammers prevent communications between the base station and the cell phones. The primary reason for its proliferation is to prevent the disruption of the silence, e.g. in cinemas, examination rooms, also law enforcement agencies use them to interrupt enemy's communications, or the police to prevent explosives from being activated remotely. Although their use and possession is illegal in many countries, this has not stopped their proliferation. Their study and characterization should help to mitigate their effects.

Mobile phones operate in different bands and modulations, but in this work some common jammers are presented.

2.1.3.1 Code Division Multiple Access (CDMA)

CDMA is a spread spectrum technique that allows several transmitters to send information simultaneously over a single communication channel. This technique has strong immunity against noise, so the most common jamming method is a chirp sinusoidal signal (Fig. 2.8a) of an average power increase of 40 dB covering around 60 MHz of bandwidth (Fig. 2.8b). The jammer is turned on from t = 8 s to 14 s, as it can be noticed in Fig. 2.8b. In cases like this, where the interference is just a small fraction of time of the measurement, spectrogram techniques perform very well.

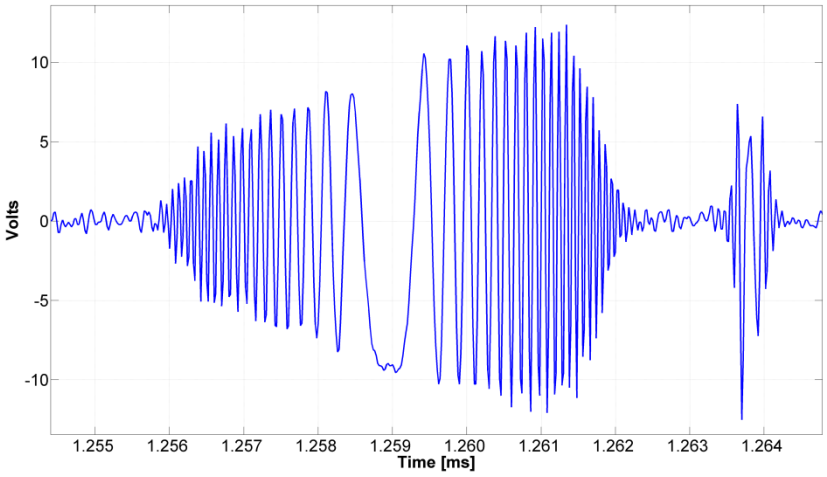

a.

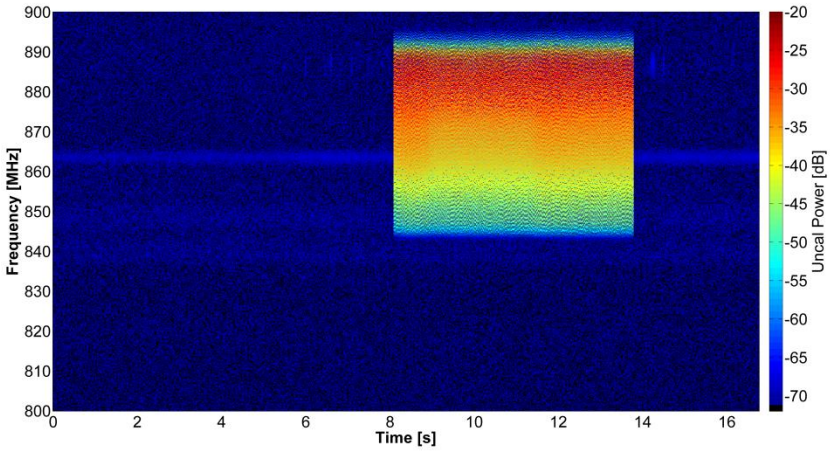

b.

Fig. 2.8 Characterization of a CDMA jammer at a central frequency = 869 MHz. Jammer turned on from 8s to 14s. a) Signal's amplitude. b) Spectrogram in dB and Resolution Bandwidth of 3 kHz.

2.1.3.2 Group Special Mobile (GSM) Communications

This system has become a global standard for mobile communications. It replaced analogue cellular networks, and it was later expanded to include data communications. Typically, a chirp sinusoidal interference is also used to disrupt the communications, as shown in Fig. 2.9a. The jammer is turned on from t = 8 s until the end of the measurements, as illustrated in Fig. 2.9b. The occupied bandwidth is approximately 40 MHz as it can be noticed in Fig. 2.9b. The jammer signal overlaps with the

communications signal which is always present, even from t = 0 s to t = 8 s, before the jammer is turned on; this can be clearly seen in Fig. 2.9b.

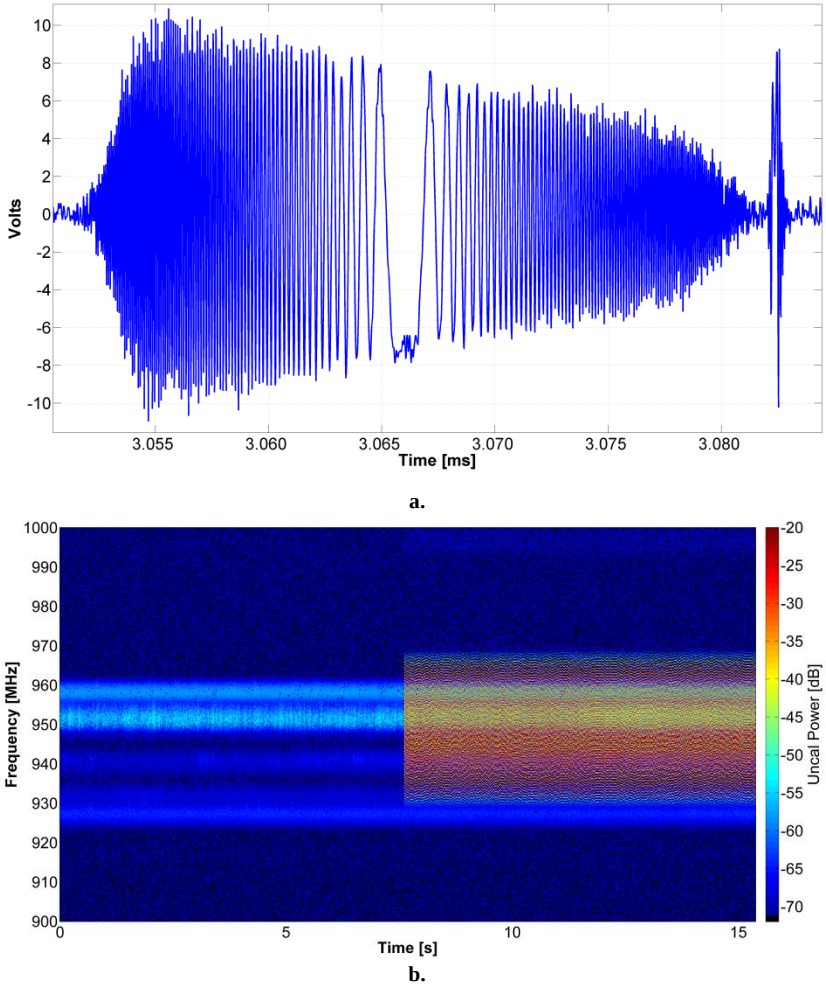

Fig. 2.9 GSM-850 jammer characterization at a central frequency of 950 MHz. a) IQ signal plot. b) Spectrogram presenting time and frequency in dB and Resolution Bandwidth of 3 kHz.

2.1.3.3 Third Generation of Mobile Telecommunications Technology (3G)

This is a set of standards used for mobile devices and mobile telecommunication services and networks that comply with the International Mobile Telecommunications-2000 (IMT-2000) specifications by the International Telecommunication Union [51]. 3G finds application in wireless voice telephony, mobile internet access, fixed wireless internet access, video calls, and mobile TV.

As most other jammers, a sinusoidal chirp is typically used as the interfering signal (Fig. 2.10a). The jammer is turned on from t = 12 s to 46 s, as it is shown in Fig. 2.10b. In this case the occupied bandwidth is around 50 MHz, as it can be seen in Fig. 2.10b. The high power interference overlaps with the communication signal's channel as evidenced in Fig. 2.10b, although the jammer's bandwidth is at one of the edges of the communication signal's bandwidth.

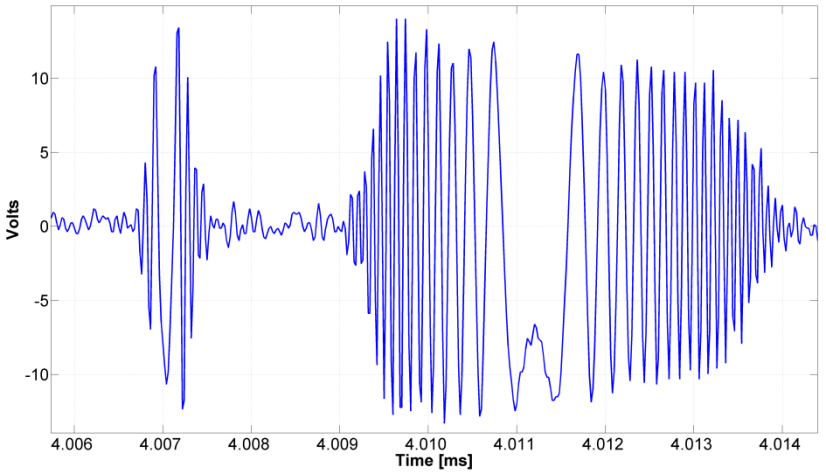

a.

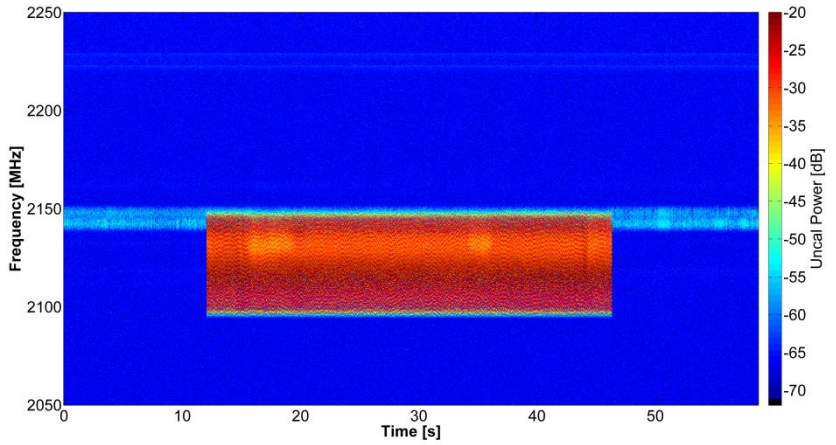

b.

Fig. 2.10 Characterization of a 3G jammer at a central frequency = 2123 MHz. a) Signal's amplitude. b) Spectrogram in dB and Resolution Bandwidth of 3 kHz. Note that the jammer is not centred in the band.

2.1.3.4 Digital Cellular Service (DCS)

DCS is an alternative name for GSM-1800. GSM-1800 uses the band from 1710 to 1785 MHz to send information from the mobile terminal to the base transceiver station (uplink) and the band from 1805 to 1880 MHz in the other direction (downlink). Again a chirp sinusoidal interference is often used to disrupt the communications as illustrated in Fig. 2.11a. The jammer is turned on from t = 8 s until the end of the measurements, as shown in Fig. 2.11b. The occupied bandwidth is approximately 170 MHz, as seen in Fig. 2.11, which overlaps with the communications signal. This jammer also introduces a smaller interference in the 2100 MHz communications band, as it can be noticed in Fig. 2.11b.

2.1.4 Other Jammers

There are other types of jammers less common and not characterized in this work. They are Gaussian, Continuous Wave, Gold and Spoof. Gaussian jammers introduce Gaussian interference, increasing the noise level where measurements are corrupted. Continuous Wave is a single sinusoidal signal at the targeted system frequency. Gold jammer is a very sophisticated one that generates fake PRN codes that makes the receiver unable to determine authentic data. Spoof jammer is a kind of "intelligent jammer", because its purpose is to make the receiver to be wrong, by transmitting realistic, fake data, at a higher power.

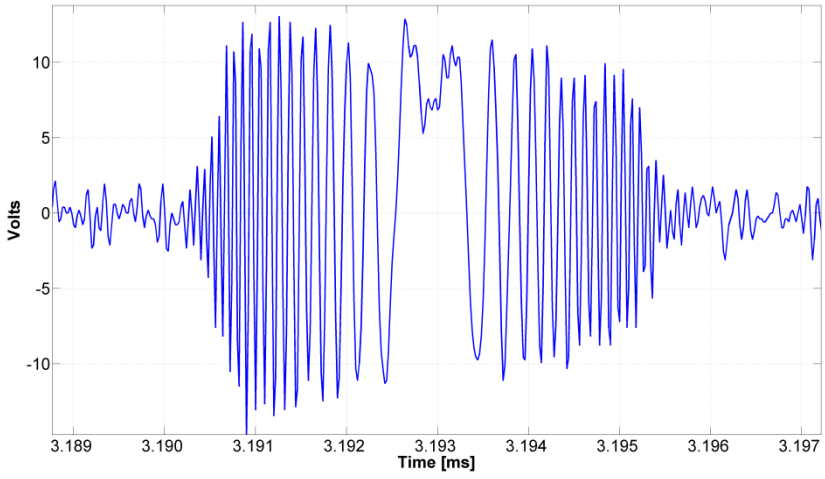

a.

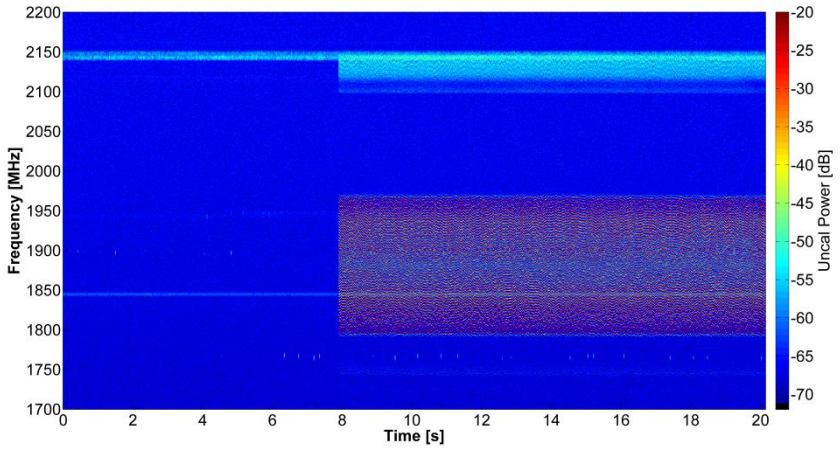

b.

Fig. 2.11 Characterization of a GSM-1900 jammer at a central frequency = 1900 MHz. a) Time-domain signal. b) Spectrogram in dB and Resolution Bandwidth (R_b) of 3 kHz.

2.2 OTHER UNINTENTIONAL SOURCES OF RFI: CHARACTERIZATION OF SPARKS' SPECTRA

Sparks are a very common source of RFI [52 - 57]. A system with a spark gap has also been designed and implemented. Vehicles, DC motors, etc. have components that produce sparks. The system is constructed with an oscillator that drives a large ratio transformer in order to convert 12 volts to many thousands of volts so that a spark is produced. In order to make a larger spark and avoid ozone contamination, a bulb with the filament broken is used to benefit from its vacuum and terminals separation. The frequency can also be controlled by a computer serial port, in order to have oscillations at different frequencies. The complete system setup is shown in Fig. 2.12. Note in the spectrum analyser on the left hand side the peak, showing the interferences generated by the spark.

The interferences generated vary from the driving frequency. At lower frequencies the interferences last longer, but are less frequent, while at higher frequencies the interferences appears more often, but last less. The system has been designed in order to receive commands from a PC setting the desired frequency in Hz. The higher frequency that creates a spark is around 1200 MHz, above that a smaller gap is needed to make the spark appear. In Fig. 2.13 is shown the spark gap at different frequencies.

Figure 2.14a shows the results from the first experiment. From 25 s to 75 s the spark gap system is turned on at a frequency of 400 Hz. The system can produce power peaks up to 40 dB above the noise level from a distance of 40 cm. of the measuring antenna. Figure 2.14b is a zoom of Fig. 2.14a, showing in more detail the interference type that is actually the superposition of multiple chirp signals.

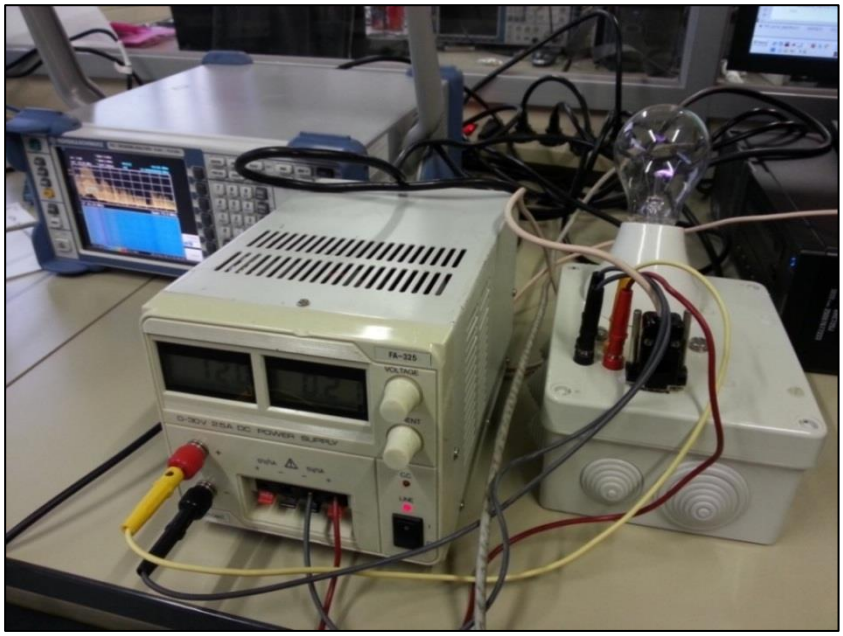

Fig. 2.12 Spark gap system. From left to right: spectrum analyser, power supply, and spark gap at vacuum.

Fig. 2.13 Spark gap figures: From left to right 100 Hz, 400 Hz, 900 Hz and 1200 Hz.

In Fig. 2.15 the results from another experiment are presented. Every 20 seconds the frequency is increased by 100 Hz. Starting at 100 Hz and finishing at 1200 Hz from t = 240 s until t = 320 s. Although results are chaotic, at lower frequencies

interferences last longer because there is a slower spark gap change, but sweeps slower. Interferences are generated when the spark current arrives at the second filament.

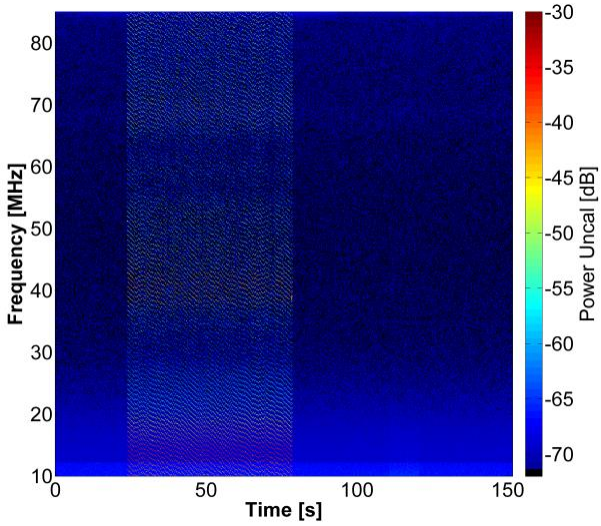

a.

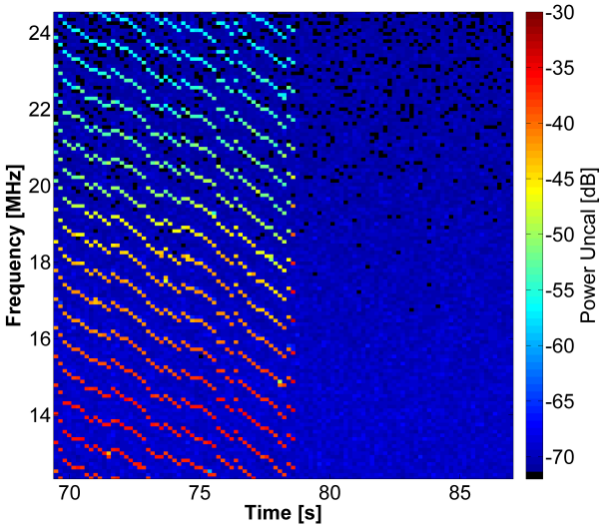

b.

Fig. 2.14 Spectrogram of the spark gap system turned on from t = 25 s to 77 s at 400 Hz. a) Full experiment setup from t = 0 s to 150 s, from 10 to 85 MHz frequency span. b) Figure 2.14a zoom.

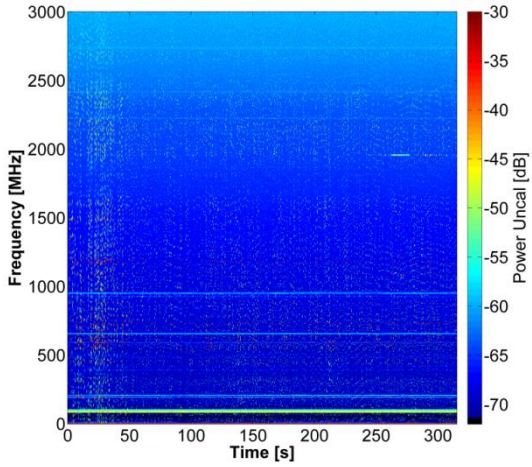

Fig. 2.15 Spectrogram of the spark gap system. Every 20 seconds the frequency is incremented by 100 Hz, starting at 100 Hz and finishing at 1200 Hz from t = 240 s until 320 s.

In Fig. 2.16, zooms of Fig. 2.15 are used to show the interferences affecting different channels. Sometimes, when a motorcycle passes nearby, interferences can be noticed in the television bands (54 MHz to 72 MHz, 76 MHz to 88 MHz, 174 MHz to 216 MHz, 512 MHz to 608 MHz and 614 MHz to 698 MHz), or listened to in the FM radio (88 MHz to 108 MHz). This environment is similar to the results shown in Figs. 2.16a, 2.16b and 2.16f, where those bands are contaminated by spark gap generated RFI. The similarity becomes because the spark gap is produced by a coil used in combustion motors to provide the high voltage needed by the igniting spark plug. Motorcycles motor introduces little attenuation to the generated RFI, allowing it to reach close television or FM radio systems.

In Fig. 2.16c it can be seen that the 2.4 GHz wireless networks and satellite communication at 2.2 GHz are also interfered. Mobile phone services are also affected by those interferences as it can be noticed in Fig. 2.16d

Examples of RFI in Microwave Radiometry and GNSS bands are shown in Figs. 2.16e and 2.16f. As it was explained before, lower spark frequencies produces wider spectrum interferences as in Fig. 2.16e, while in Fig. 2.16f they are narrower due to the smaller duration of the spark.

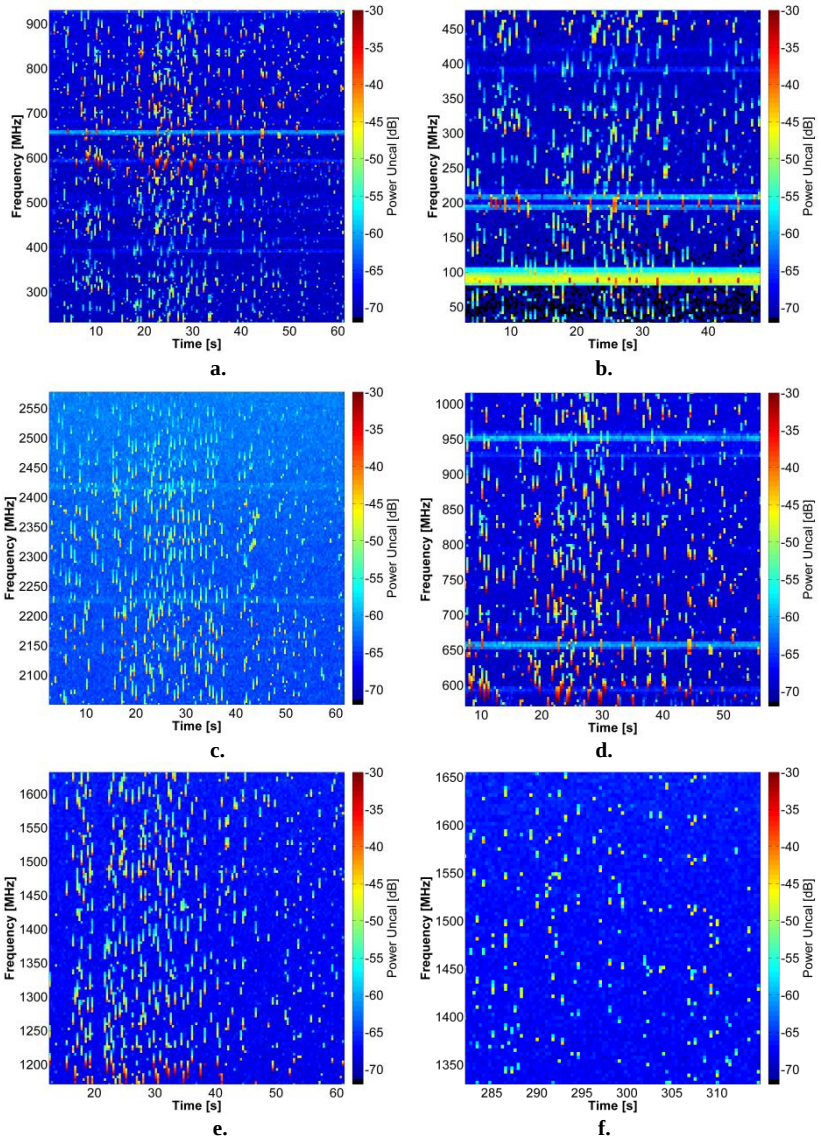

Fig. 2.16 Spectrograms of the spark gap system, zooms of Fig. 2.15 at different times and frequencies. a) Interfering lower bands Telemetry and Television Channels. b) Interfering FM Radio, Aeronautical Radio navigation, Satellite, Television Channels and Telemetry transmission. c) Interfering satellite and wireless networks. d) Interfering Mobile Phone services. e) Interfering the Microwave Radiometry and the GNSS bands. f) Interfering the Microwave Radiometry and GNSS bands with narrower signals than Fig. 2.16e.

2.3 CONCLUSIONS

Jammer's signals are used to inhibit telemetry systems, GNSS, and mobile phone services, among others.

From the analysis of the data acquired, the most common signal jammers seems to be a chirp signal to interfere a bandwidth from f_1 to f_2, changing the bandwidth (B = f_2 - f_1) and Central Frequency $(f_0 = (f_1 + f_2)/2)$ depend on the targeted system. Other types include Gaussian, Continuous Wave, Gold and Spoof.

Sparks are also a source of RFI, and they appear where a voltage is large enough to break the gap. The most common places they appear are the spark plugs in motor vehicles, DC motors, high voltage installations, etc.

Spark RFI produces white noise and contaminates the spectrum. Sparks at lower frequencies produce wider interferences and last longer because the spark stays more time than at higher frequencies.

Chapter 3

LOCATING RFI IN SPACE, TIME AND FREQUENCY

RFI sources can be detected in space, time and frequency. Locating RFI in those three domains gives information that can improve the RFI mitigation techniques. Locating in space helps to detect the direction of the RFI and countermeasures could be implemented to avoid measurements in that direction or to enforce the source to shut down. Locating in time domain, can give information about its periodicity or randomness. Possible countermeasures could be discarding or just avoid measuring during the time when the RFI is present. Locating in frequency gives information about its bandwidth and frequency, so discarding measurements in those subbands, or simply avoid measuring the contaminated ones, can mitigate the interferences.

3.1 RFI SIGNATURES IN TIME AND SPACE

In this section, the results of a temporal and spatial RFI survey at L-band are presented. For this purpose the L-band Automatic Radiometer (LAURA) instrument was used. The original LAURA instrument was a fully polarimetric Dicke radiometer implemented in 2000 for the field experiments carried out in support of the Soil Moisture and Ocean Salinity (SMOS) mission [63, 64]. In 2010 LAURA was decommissioned and replaced by LAURA 2.0. Since it was found that the polarimetric channels did not provided much information at L-band[*], the LAURA 2.0 instrument had a simpler design: a dual polarization antenna connected to an extremely stable Total Power Radiometer. LAURA is thermally controlled with a Proportional Integral Derivative temperature control at 45ºC ±0.1ºC and mounted inside a plastic box covered with a metallic film acting as a Faraday cage, and several layers of polystyrene to protect the instrument against external humidity and temperature changes. In this experiment the instrument was mounted on a mast (the right mast in Fig. 3.1). Azimuth and elevation scan movements were performed in an automatic manner, controlled by an ad-hoc software.

The main experiment aims at estimating atmospheric effects in polarimetric radio occultations for the PAZ mission [65], the software controlled the position, pointing in real time to the visible GPS satellites, and followed the one indicated by a script.

The second instrument of the experiment (the left mast in Fig. 3.1) is a novel antenna array, designed for very low cross-polar ratio, connected to a commercial GPS receiver and to the GOLD-RTR [66]. The antenna design is based on seven symmetric square microstrip patches arranged in the vertices and centre of a regular hexagon, which are properly fed and combined to obtain the two desired orthogonal linear polarizations. The experiment has been designed for polarimetric studies in the presence of hydrometeors in the lower atmosphere, within the framework of the preparatory activities of the GNSS Radio-Occultation secondary payload [65] within the PAZ mission. The antenna array operates at the GPS L1 band (1575.42 GHz central frequency) covering a 10 MHz full-bandwidth. Its main parameters are 14 dB

[*] As opposed to higher frequencies where the polarimetric channels provide useful wind direction signatures over the ocean, at L-band the third stokes parameter was found to be almost negligible (T3 << 1K), and T4 completely negligible (T4 ≈ 0K). Therefore, in LAURA 2.0, these two channels were eliminated.

directivity, and cross-polar <-30 dB in the main beam, since the transmitting GPS satellite is tracked by mechanically scanning the antenna; and to provide two orthogonal linear polarizations from which all the desired combinations: Right Hand Circular Polarization (RHCP), Left Hand Circular Polarization (LHCP), etc. were derived.

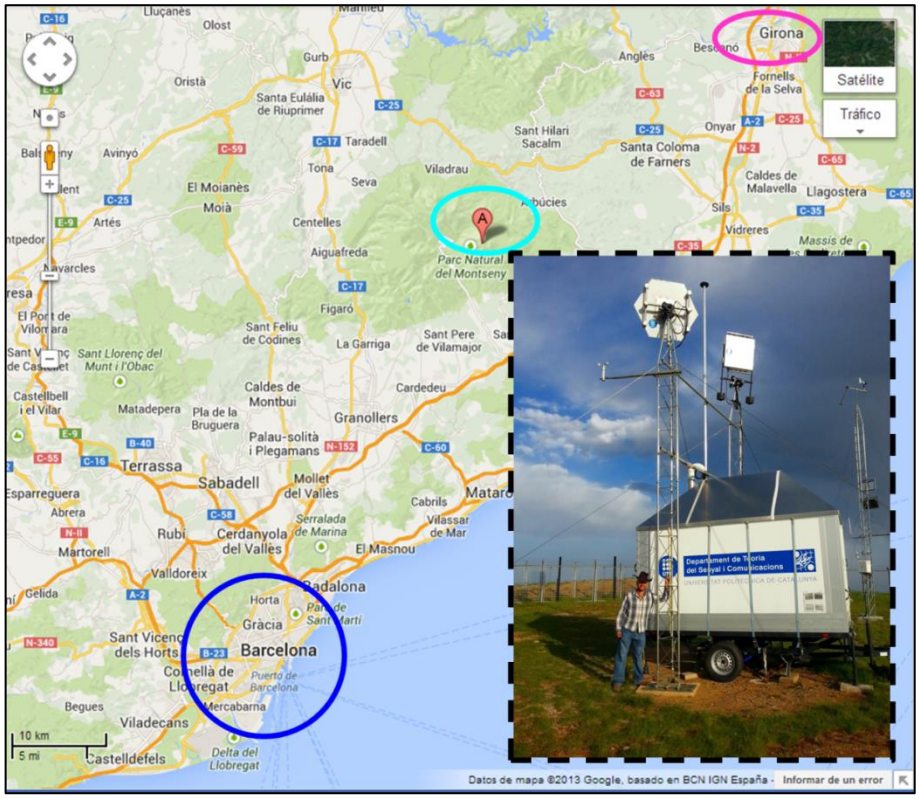

Fig. 3.1 LAURA Instrument (top right) and dual-polarization Antenna (top left) mounted at Turò de l'Home mountain peak at N41º 46' 24" E2º 26' 17" GPS coordinates (in cyan ellipse) and 1667 meters above sea level. Barcelona city is in the blue circle and Girona city is in the magenta ellipse.

The experimental data was collected from February 23rd until March 21st, 2012 and it provided thousands of samples along the satellites paths, and because of those trajectories change a little every cycle, a large area was covered (captured 370 files of around 4000 samples each one). Despite this, there are still blank places without measurement, and many times the pointing direction is zero degrees azimuth and elevation where the system doesn't require a satellite to follow. As it can be noticed in Figs. 3.2 and 3.3, the largest power came from the azimuth 220º, pointing to the city of

Barcelona, as it can be seen on the map in Fig. 3.1, where the experiment location is shown in cyan, and Barcelona city in blue. An increase in the power can also be noticed between 40º to 60º, that azimuth direction corresponds to the city of Girona inside the magenta ellipse. The interferences appear near 25º elevation because a building blocks the antenna at lower elevations in that azimuth direction.

Additionally, over 25º elevation, the average power level decreases, because most interferences are man-made and come from ground.

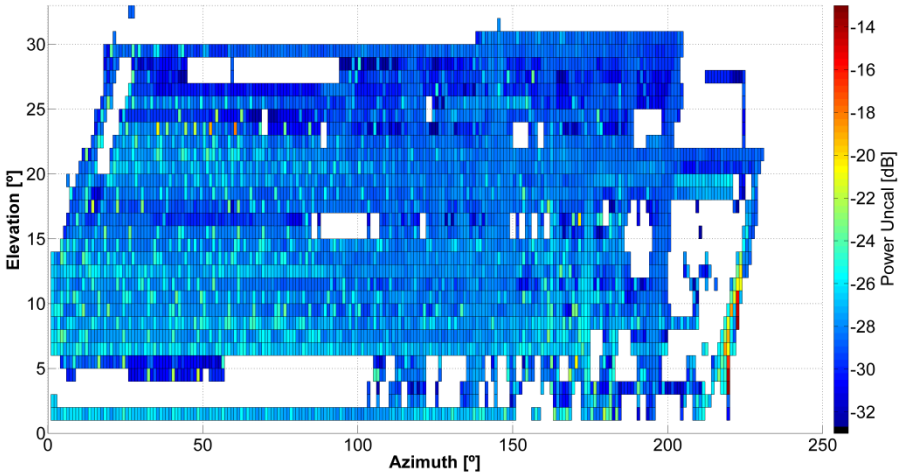

Fig. 3.2 Average uncalibrated power of the LAURA 2.0 instrument survey. X axis: azimuth angle. Y axis: elevation angle.

Figure 3.3 also shows the instantaneous power over time for a small data series and over it the azimuth angle where the antenna was pointing. As mentioned before, the highest power comes from the city of Barcelona when the antenna points around 200º. The kurtosis value is 42.41, very far away from 3, confirming the existence of strong RFI. In the next section, the periodicity and possible RFI sources are presented.

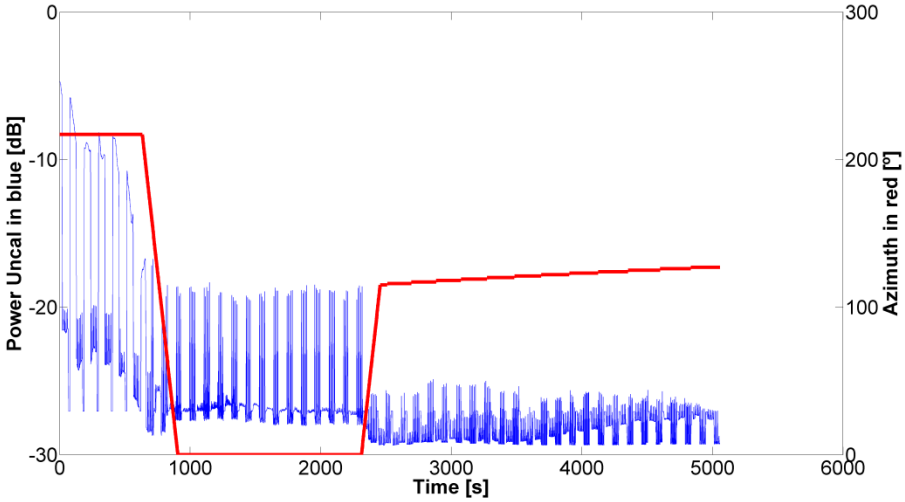

Fig. 3.3 Instantaneous power over time taken on March 2th of 2012 at 0:49:16 until 2:13:33 UTC time (a total of 5057 seconds). In red is the antenna's azimuth pointing angle.

3.2 TIME AND FREQUENCY-DOMAIN RFI SIGNATURES

The main objective of this study is to have a better understanding of the presence and types of RFI sources present in an urban environment, in this case the city of Barcelona. The first part of this study concerns the band from 1.400 to 1.427 MHz, used for soil moisture and sea surface salinity monitoring. In the second part, the X-band from 10.60 to 10.80 GHz is studied. A 5 minutes long measurement has been acquired every 20 minutes, during 30 days for each band, in 964 sub-bands, with a sweep time of 5 ms.

3.2.1 Methodology

The first part of this study consists of acquiring long series of data from the Department of Signal Theory and Communications building at the Universitat Politècnica de Catalunya-Campus Nord located in the city of Barcelona (Fig. 3.4), using an L-band total power radiometer front-end with a spectrum analyser as a back-end. For the second part, an X-band (10.60-10.80 GHz) total power radiometer front-end has been used. During 30 days for each band, every 20 minutes, a 5 minutes measurement sequence has been acquired in 964 sub-bands, with a sweep time of 5 ms. The antenna was pointing to azimuth 100º.

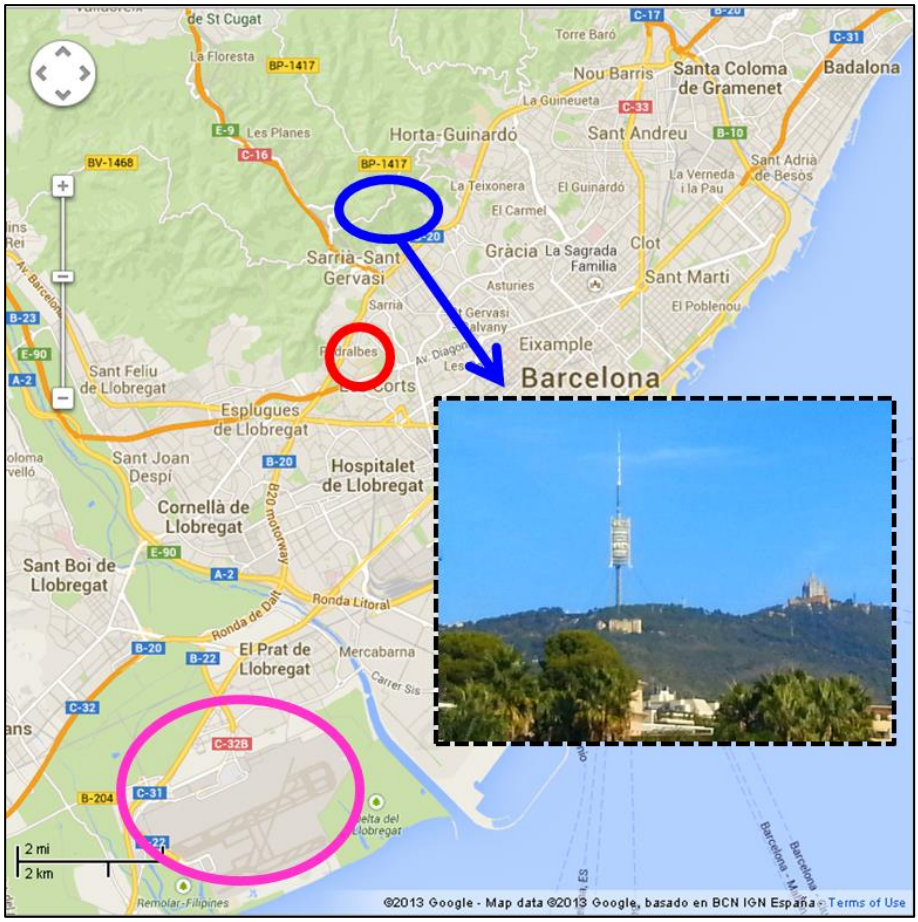

Fig. 3.4 Map for georeferencing the measurements. Red: experiment location at Department of Signal Theory and Communications building – Universitat Politècnica de Catalunya (GPS position N 41º23'19" E 2º06'41"). Blue: Collserola Communications Tower (inserted photo). Magenta: Barcelona Airport. The antenna is pointing to 100º in azimuth that is the city centre.

The second part of the study analyses the temporal evolution of the RFI present in the radiometric measurements, using the following RFI detection algorithms: spectrograms (simultaneously time and frequency) analysis [10, 11, 58], time-domain analysis [9, 59, 60], frequency-domain analysis [9, 60], statistical analysis over time [60, 61], and statistical analysis over frequency [60].

3.2.2. Results

Uncalibrated power spectrograms over the whole series of days have been calculated and presented in Fig. 3.5a at L-band, and Fig. 3.5b at X-band. Figure 3.5a shows a continuous spectrogram from 1.400 to 1.427 GHz over 30 days during May-June 2012 in the city of Barcelona, Spain [62]. This figure illustrates:

1) The variability of the RFI over time and frequency, and
2) The level of RFI contamination usually found is at least ~10 dB over the spectral noise density background in large portions of the spectrum, and during long periods of time.

Note that only at the end of May, and if some occasions from approximately June 8th to 12th, the spectrum is mostly RFI "free".

In Fig. 3.5b, a continuous spectrogram from 10.6 to 10.8 GHz over 30 days during June-July 2012 in the city of Barcelona, Spain [62] is presented. The level of contamination usually found is less than ~5 dB over the spectral noise density background, and mostly concentrated close to 10.60 GHz.

Based on the algorithms described in [9-12, 16-18, 58], the percentage of RFI present over time is estimated by analysing time and frequency domains, and normality tests listed at the end of Section 3.2.1. Results are shown in Figs. 3.6a and 3.6b. For every measurement, the estimation is computed as the fraction of the time occupied by a detected RFI. As it can be noticed, most of the "protected" L-band is contaminated (in the best cases just temporally). It is remarkable that the most corrupted areas are near 1400 MHz, which can be attributed to near-by emissions, and in the centre of the band, around 1419 MHz. At X-Band, the RFI contamination is much smaller, as it is seen in Fig. 3.6b. The maximum probability of RFI that appears is less than 1% (P_{fa} = 0.1%).

In Fig. 3.7 the total percentage of the time occupied by RFI during the 30 days of the survey is shown. Here, it is confirmed that the "protected" L-band areas with the largest RFI are near the 1400 MHz, and 1419 MHz. Note in Fig. 3.7b the largest percentage is close to 10.6 GHz. This means that around 10% of the time, this band has RFI, while in Fig. 3.6b shows the probability at a specific moment.

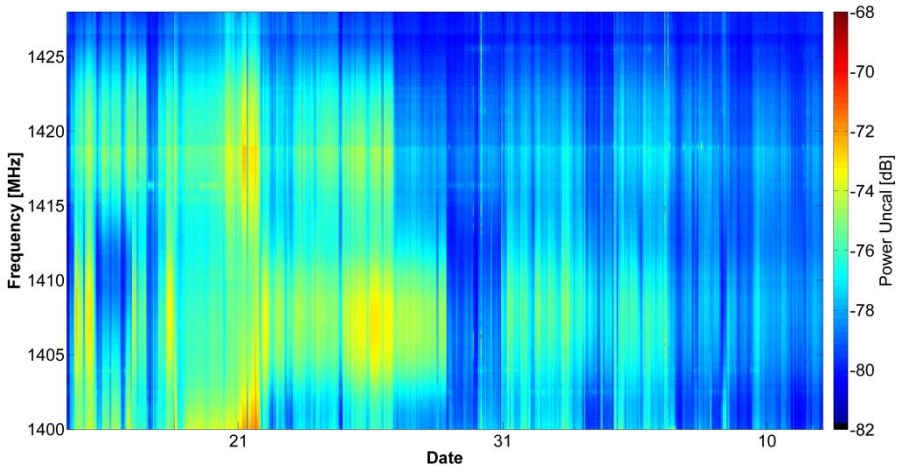

a.

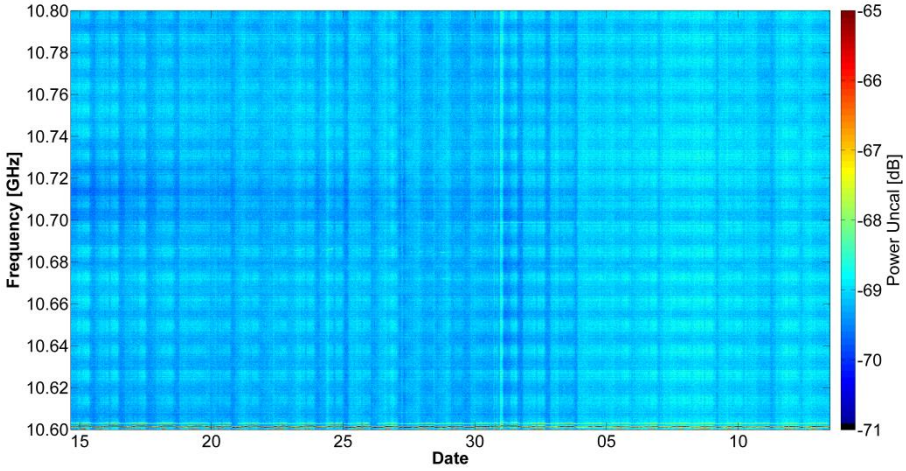

b.

Fig. 3.5 Average Uncalibrated Power Spectrogram over all experiment at: a) L-Band. Horizontal axis: days of May and June 2012. b) X-Band. Horizontal axis: days of June and July 2012

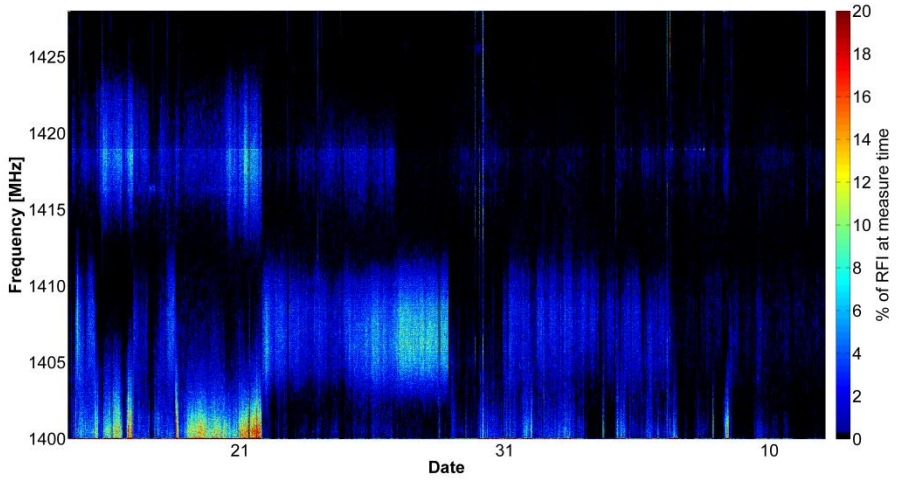

May ***June***

a.

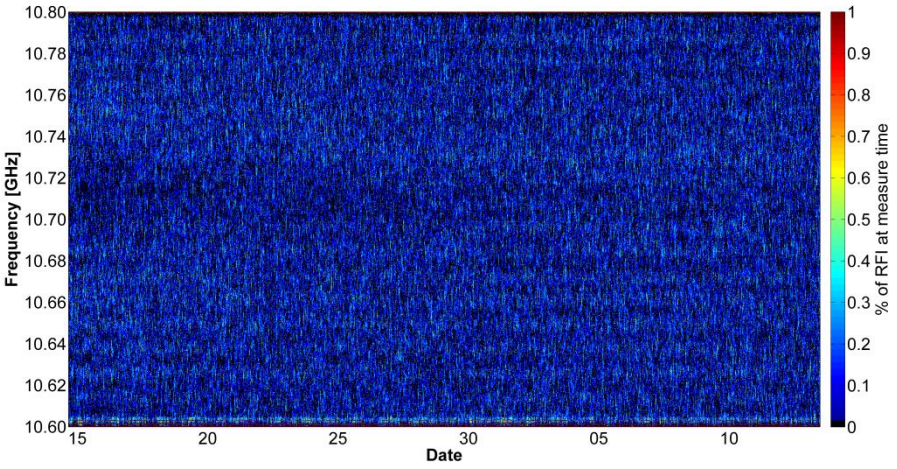

June ***July***

b.

Fig. 3.6 Percentage of RFI vs. measurement time during all the experiment at: a) L-band. b) X-band

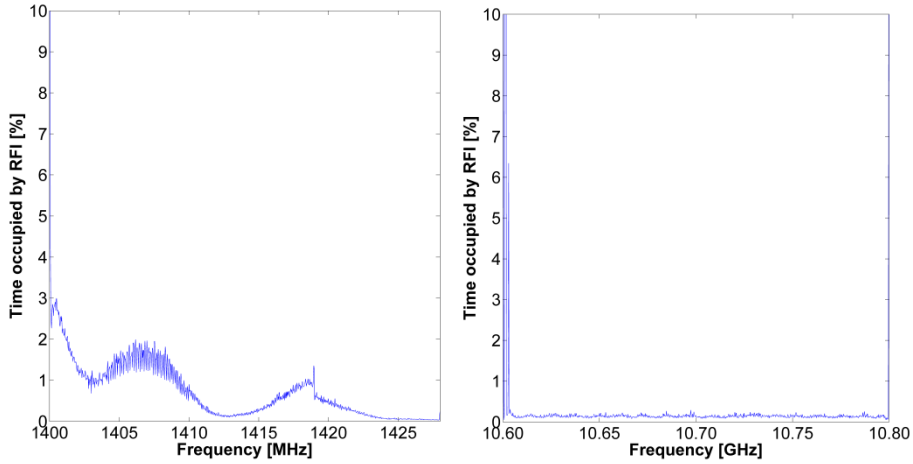

a. *b.*

Fig. 3.7 Average percentage of time occupied by RFI as function of frequency: a) in the 1400-1427 MHz "protected" band, and b) in the 10.68 - 10.8 GHz band.

Anyway this is only valid in the long term, as it can be seen in Fig. 3.8, zooming on a 9 s interval spectrogram of the "cleanest" data (~1413 and ~1425 MHz); many short spread-spectrum RFI are also present in the 9 s interval.

Figure 3.8 shows a sub-band from 1.410 to 1.415 MHz, starting on May 15th, 2012 from 16:56:55 h to 16:57:04 h (9 s). This zoom shows that most of the RFI is actually pulsed (short duration) and broadband. Chirp signals are difficult to detect depending on the chirp rate, and spread-spectrum modulation signals whose spectral density is below that of the thermal noise may be present, but are undetected in the spectrogram.

Using a time-domain analysis [9, 63] the entire band would be removed during the affected time (see Fig. 3.9, most interferences are concentrated from ~12 s to ~23 s). Eventually, because of the noticeable increase of the instantaneous total power over the mean, high power interferences can be easily discarded in the time domain using a threshold.

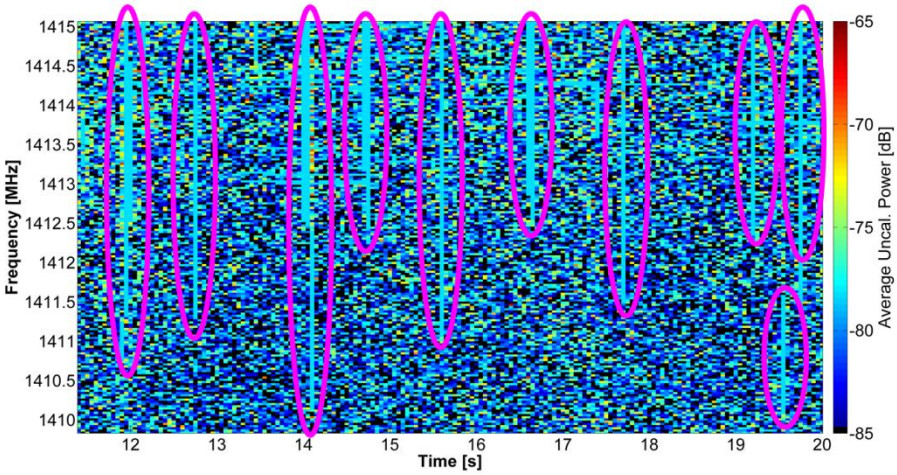

Fig. 3.8 Temporal wide spread RFI spectrum during an 9 seconds interval extracted from a measure at date 2012/05/15 16:56:55h.

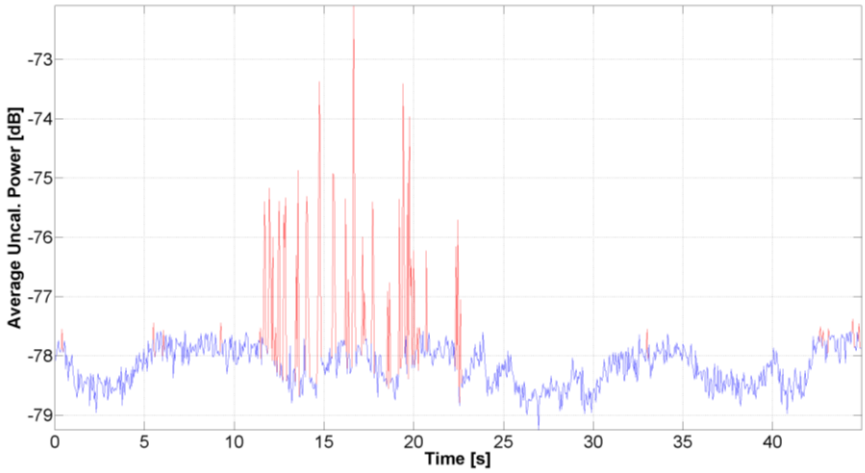

Fig. 3.9 Instantaneous power during a 45 seconds measurement acquired on 2012/05/15 at 16:56:55 h. Red Plot: including RFI over time (K = 20.89). Blue Plot: with RFI contaminated intervals removed (K = 2.12).

However, this way all the band is totally removed. For frequency domain analysis [9, 63] the only difference is that it is applied to entire subbands for all the measurement time as it can be seen in Fig. 3.10. Alternatively, using the spectrogram analysis [11] only the RFI is discarded, as it is shown in Fig. 3.11.

Because time- or frequency-domain techniques alone are based on eliminating RFI using thresholds, a great disadvantage is that they reduce the probability of detection and increase the probability of false alarm (removal of clean data). There is no method

to completely guarantee the effectiveness of the selected threshold. If the RFI is below it, it will not be detected, and lowering the threshold will eliminate clean signal too. Statistical analysis over time [17, 18], and statistical analysis over frequency [17] could help to validate those RFI mitigation methods, but alone they have the disadvantage that discard all the data. The method used in this study is the Kurtosis (K).

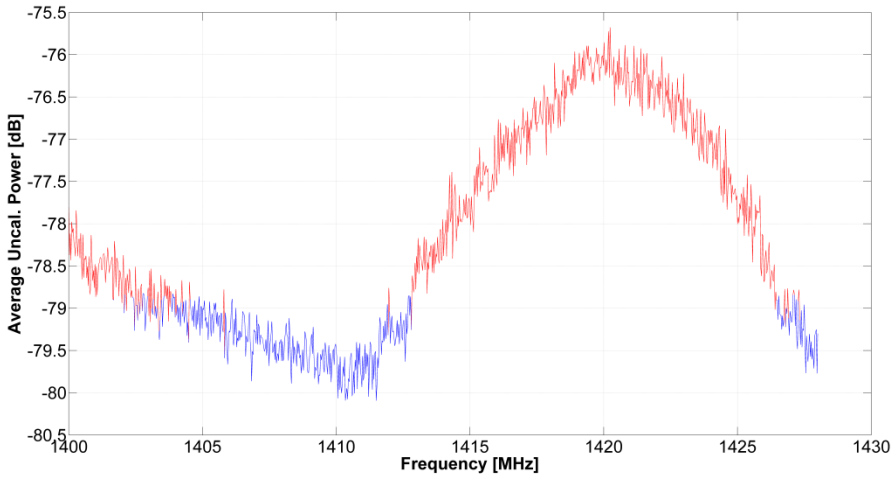

Fig. 3.10 Power spectrum after receivers' frequency response equalization using a 50 Ω load. Measurement acquired on 2012/05/15 at 16:56:55. Red: Power spectrum (K = 1.74). Blue: Power spectrum with RFI contaminated frequencies removed (K = 2.34).

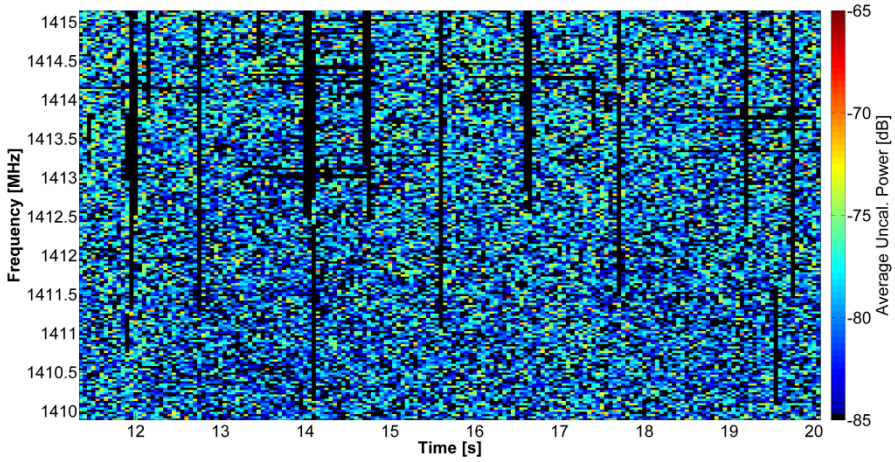

Fig. 3.11 Same spectrogram as Fig. 3.8 with RFI removed using spectrogram analysis.

As an example, for the measurement acquired on 2012/05/15 at 16:56:55 h (Figs. 3.9 and 3.10), the Kurtosis values in the time and frequency domains are K_t = 20.89 and K_f = 1.74, respectively before applying the RFI detection and mitigation algorithms. Both of them are far from 3, which indicate the presence of RFI, although with different sensitivities. After time or frequency blanking (Figs. 3.9 and 3.10) K_t = 2.07 and K_f = 2.34, which are still different from $K_{t,f}$ = 3, but much closer to it, indicating the presence of residual RFI not properly detected and cancelled by the previous algorithms. The same happens to the kurtosis applied to the spectrogram analysis, where K_{spec} = 183.78 before mitigating RFI and K_{spec} = 27.08 after the algorithm application.

3.3. TIME, FREQUENCY AND SPACE RFI SIGNATURES

Time, frequency and space RFI signatures takes unites the advantages of sections 3.1 and 3.2 for detecting interferences. RFI can come from any direction, so knowing the location of arrival can be used to mitigate its effects accordingly. A semi- sphere can be scanned with this system, but since most of the RFI is human made, and it comes from ground level, the scans are simplified to azimuth scans only.

3.3.1. Experiment Set-Up

The system block diagram is shown in Fig. 3.12. It consists of three antennas at L-, C- and X- bands mounted in a mast with azimuth and elevation motors moved by a motor controller (see Appendix A.2). The scan time at each direction is around two minutes. In the Filters & Amplifiers block there is one set for every antenna.

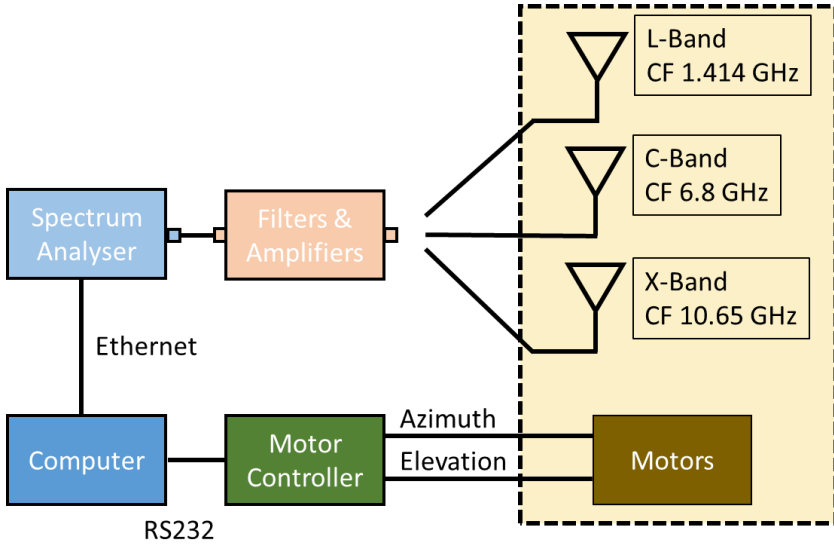

Fig. 3.12 Multiband and Multidirectional Time and Frequency RFI Detector Block Diagram

From the three antennas, only one is connected at a time as shown in Fig. 3.12. Later, the three antennas (Fig. 3.13a) have been replaced by a GPS L1 band antenna (Fig. 3.13b) with central frequency of 1575.42 MHz.

a. **b.**

Fig. 3.13 a) On top from left to right L-band, C-band and X-band antennas. Spectrum Analyser in bottom left. b) GPS L1 Band Antenna.

The system has been mounted on the roof top of building D3 at UPC Campus Nord premises in Barcelona City (Coordinates N41º23'19" E2º06'40"), as shown on Fig. 3.4

3.3.2. Experiment Results

The results are shown in time and frequency domain on a polar plot to locate more easily the interference direction in azimuth.

3.3.2.1. L-Band

In Figure 3.14, interferences can be easily detected from many places. Between 0º and 15º (Collserola Communications Tower direction) RFI appears at different times. From 45º to 135º corresponding to the city area an increment in noise level compared to the mountain zone (255º to 345º) is evident implying a higher RFI at the populated

area than the unoccupied zone. The airport radar direction between 195º and 225º also shows a RFI increase.

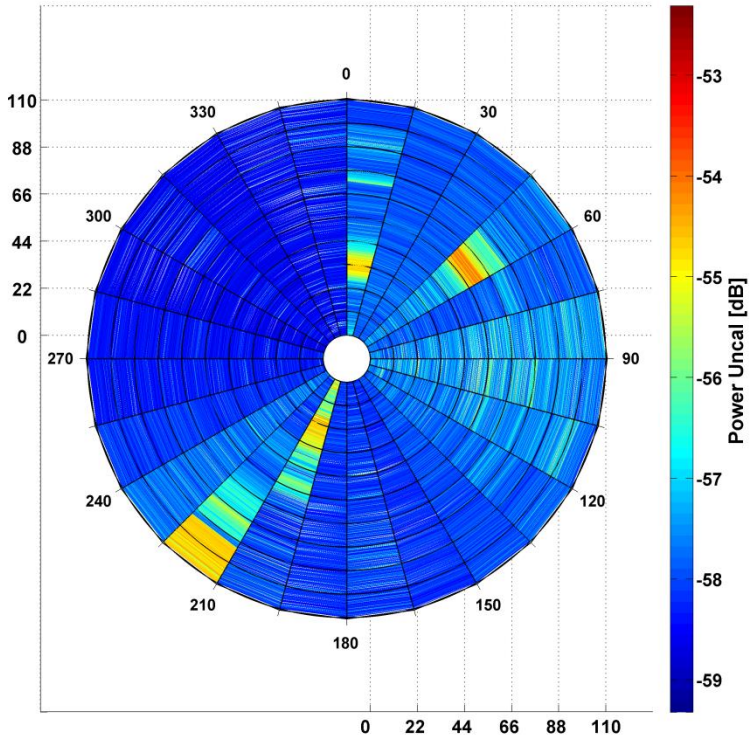

Fig. 3.14 L-band Survey. Radial distance is time in seconds at different azimuth angles in degrees. Kurtosis is $K_t = 3.84$

Figure 3.15a shows the interferences in the frequency domain. The radial distance represents the frequency from 900 to 1900 MHz. Some interference (more than 10 dB power increment over noise level) can be noticed from Collserola Communication Tower direction. Although mobile phone networks are not strictly considered RFI because they are at their corresponding bands close to the 900 MHz and to the 1900 MHz, they can be easily identified on this map, stronger in the city direction than to the mountain. A zoom of Fig. 3.15a is presented in Figure 3.15b, where Radio Navigation Service (RNS) signals [67] have been detected at 1115 MHz in the airport direction (195º to 225º).

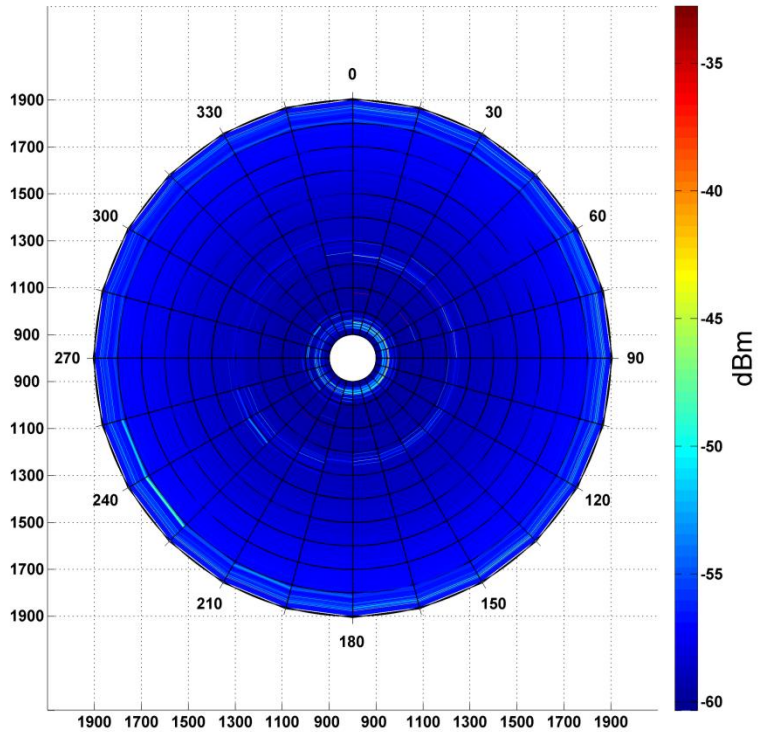

a.

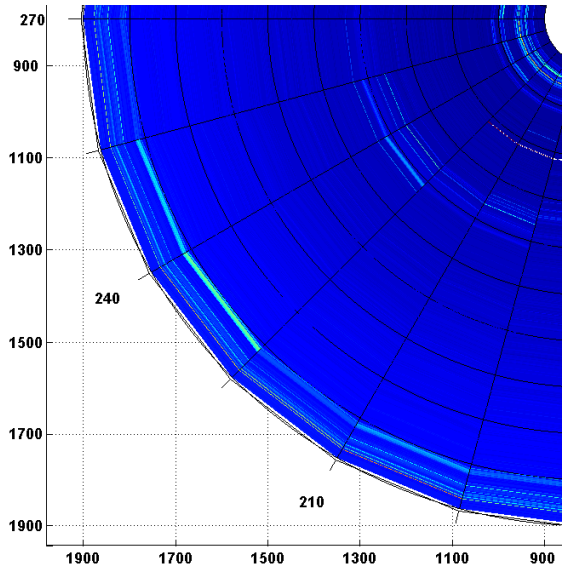

b.

Fig. 3.15 a) L-band Survey. Radius is frequency in MHz. b) Zoom of Fig. 3.15a. Kurtosis is $K_f = 32.01$

3.3.2.2. C-Band

The C-band survey presents very interesting results: in the time domain RFI is unnoticeable because it looks like Gaussian noise (Fig. 3.16a), but the kurtosis in the time (K_t = 2.84) and frequency-domain (K_f = 1.34) surveys (Fig. 3.16b) proves it is not. Frequency map shows an increase in power between 6300 and 6700 MHz that probably comes from satellite communications uplink [67].

3.3.2.3. X-Band

The X-band survey in the time- and frequency-domains is shown in Figs. 3.17a and 3.17b respectively, indicating the need of combined tests to detect RFI because in many cases are undetectable by these methods alone. The variation in both graphs is 1 dB_{pp} and it looks like Gaussian noise, but testing with the kurtosis K_t = 2.82 and K_f = 3.36 shows a small RFI present in both maps.

To detect the direction of the RFI, a table with individual kurtosis values for every direction is calculated, and it is shown in Fig. 3.18 for this example. Notice that most values are close to 3, with the error calculated as $\hat{\sigma}_K \approx \sqrt{24/N}$ as considered in [68]. For time domain, $\hat{\sigma}_K \approx \sqrt{24/900} \approx 0.16$. For frequency domain, $\hat{\sigma}_K \approx \sqrt{24/801} \approx 0.17$. The most probable source of those RFI detected is the communications tower because the directions where the kurtosis exceeds the tolerance are close to 0º. Another direction with detected RFI is to the city centre, between 150º and 200º.

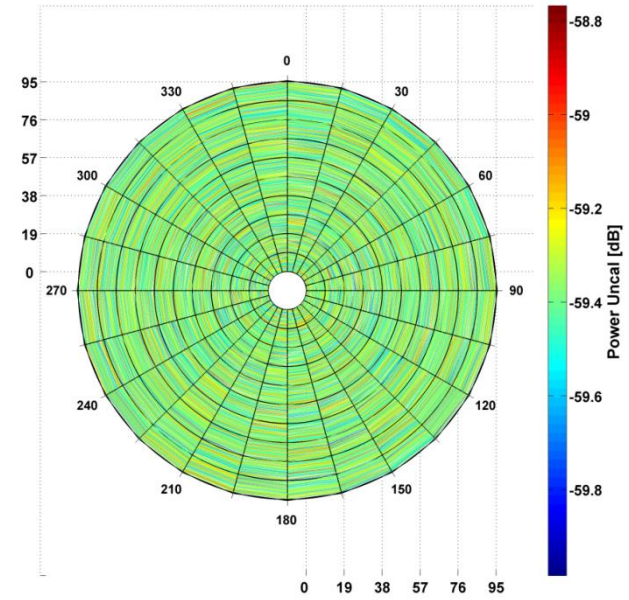

a.

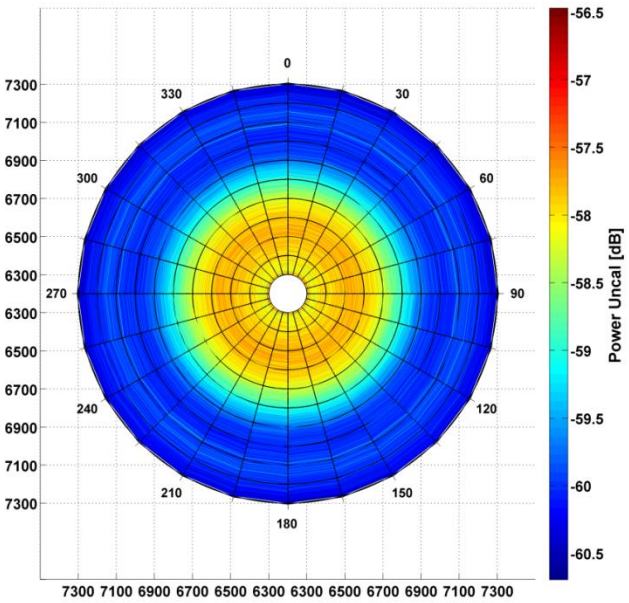

b.

Fig. 3.16 C-band survey at different azimuth angles in degrees. a) radius is time from 0 to 95 s. b) Radius is frequency in MHz.

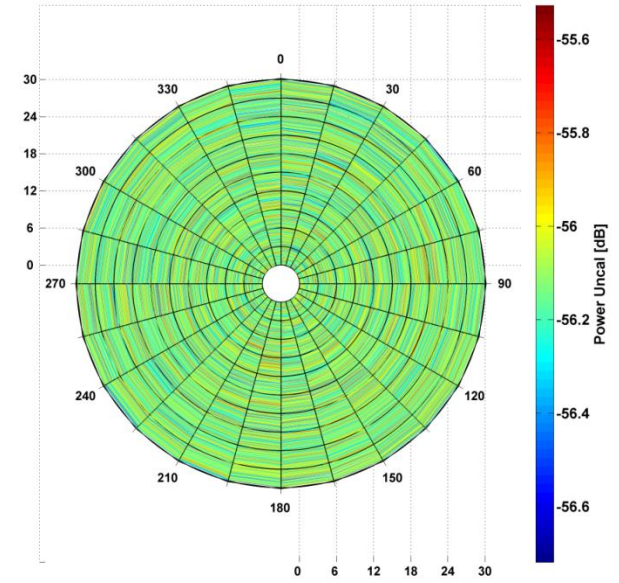

a.

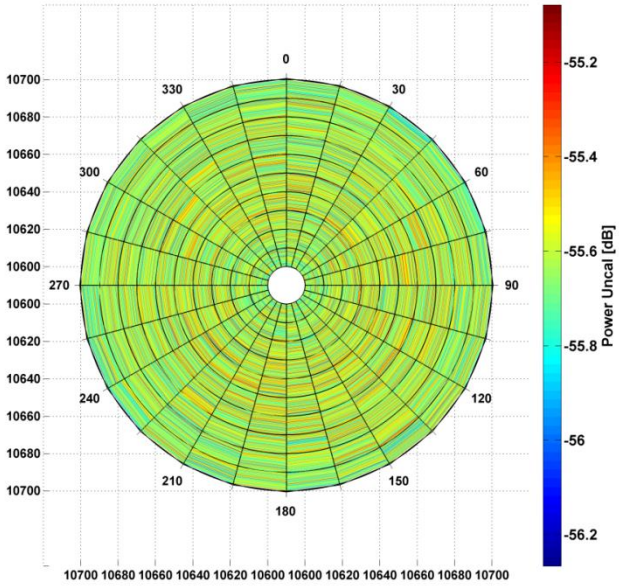

b.

Fig. 3.17 X-band survey at different azimuth angles in degrees. a) Radius is time in s. b) Radius is frequency in MHz.

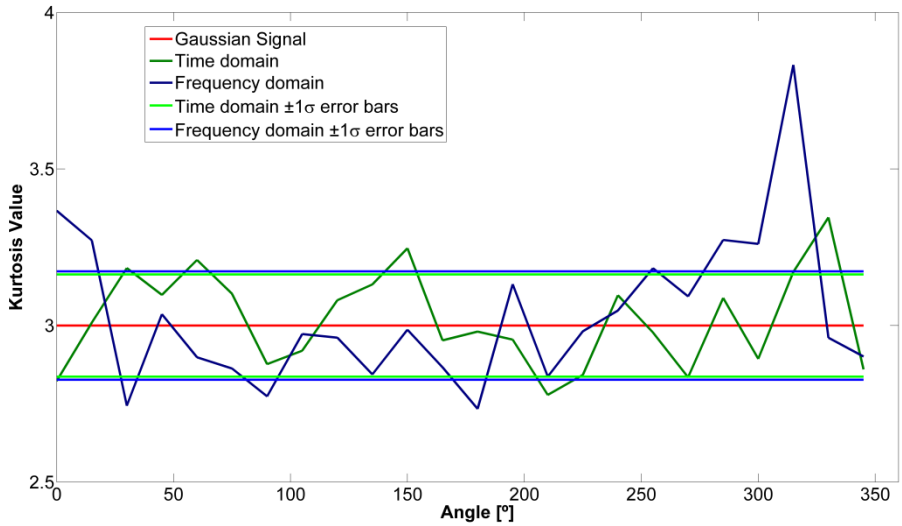

Fig. 3.18 Kurtosis values for different directions in time and frequency domains.

3.3.2.4. GNSS L1-Band

Nowadays, GNSS have become of great importance because their widespread use in aerial and terrestrial navigation, synchronization of transactions, and their original use in military applications. Interferences in aircraft systems could endanger many lives, while in bank transactions can cause large economic losses. Detecting their direction of arrival is of great importance for law enforcement purposes. In Fig. 3.19 an increase in the average power can be noticed in the direction of the Collserola Communications Tower, Barcelona's most populated area, and the RFI source at 280 degrees that is generated by some computer systems. Also, in the direction of the airport (around 200º) some RFI signals appear.

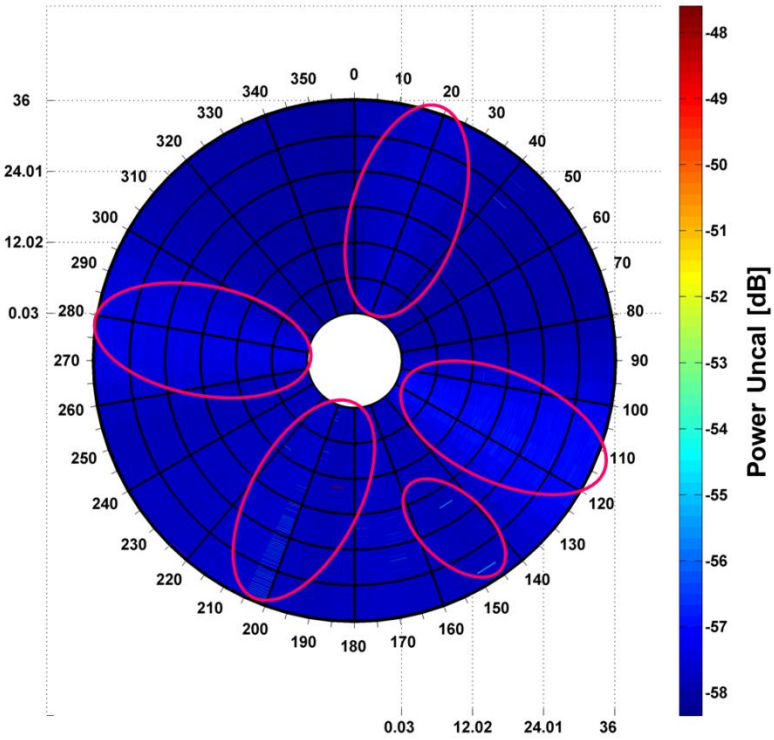

Fig. 3.19 GNSS L1 band survey at different azimuth angles in degrees, where the radius is time in seconds. Magenta ovals indicate the detected RFI directions.

In the frequency domain (Fig. 3.20), interferences are a lot clearer because they are emitted in specific sub-bands. Note that the RFI around 280º and around 1600 MHz because the GLONASS L1 band is located there. Because the interference is localized in space, further investigation was carried out and led to the conclusion that some computer systems where producing it, so when it was turned off that specific RFI disappears [69].

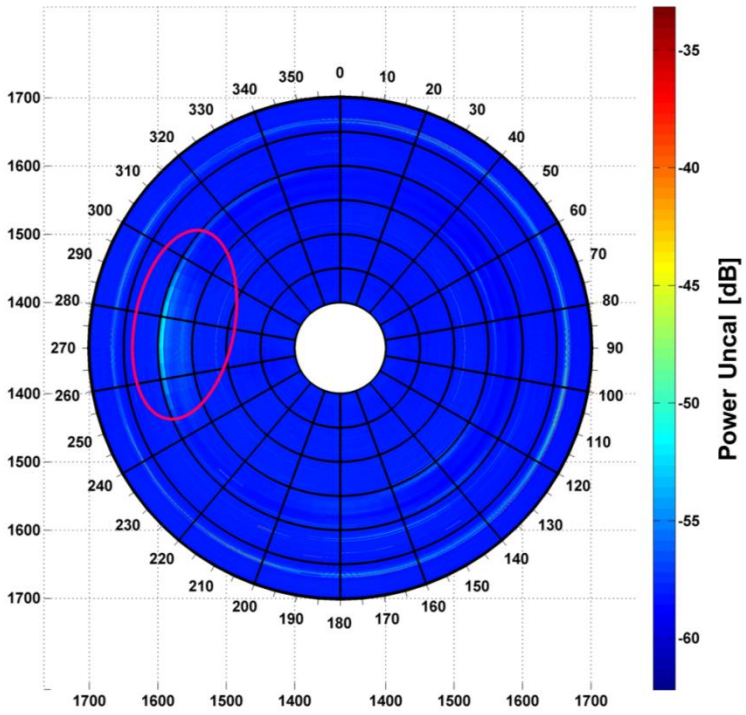

Fig. 3.20 GNSS L1-band survey at different azimuth angles. Radius is frequency from 1400 to 1700 MHz.

3.4. TIME AND FREQUENCY RFI SIGNATURES FOR RADIOMETRY BANDS

In this section a time and space RFI survey is carried out in all the radiometry protected bands used by the MERITXELL radiometer, explained in Appendix A.4. The bands covered are: L-band (1.40 GHz - 1.427 GHz), S-band (2.69 GHz - 2.70 GHz), C-band (7.14 GHz - 7.23 GHz), X-band (10.6 GHz - 10.7 GHz), K-band (18.6 GHz - 18.8 GHz and 23.6 GHz - 24.0 GHz), Ka-band (36 GHz - 37 GHz), and W-band (86 GHz - 92 GHz). Horizontal and vertical polarizations are included in the survey. For every survey, frequency equalization has been performed. Each time bin lasts around 100 ms and it has one sample for each frequency subband.

As it will be noticed in all the surveys, the most contaminated bands are the lower ones because most of the RFI sources operate in those frequencies or have harmonics that generate them.

As a preview for the spectrum used by most of the electronic systems, Fig. 3.21a shows the first 10 GHz, while Fig. 3.21b shows with finer detail the first 2 GHz of the spectrum. In both figures, the presence of the mobile phone signals around 800 to 960 MHz, and from 1800 to 1960 MHz is noticeable. Also, around 500 to 700 MHz the TV broadcasting channels are present. In Fig. 3.21a the power increase at ~2100 MHz of the 3G signal is also noticeable.

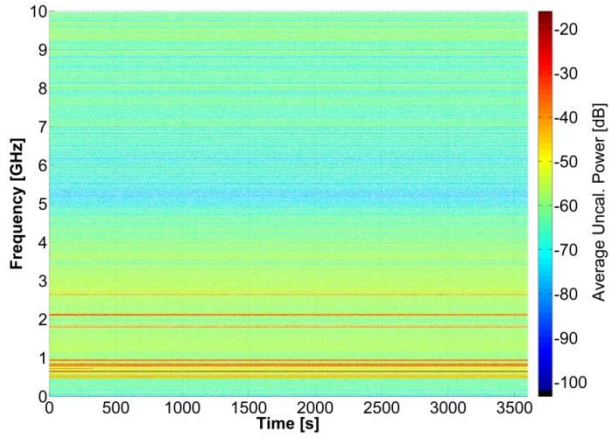

a.

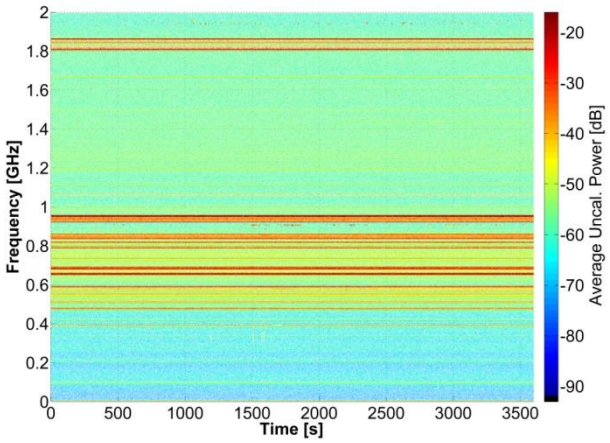

b.

Fig. 3.21 a) General survey from 0 to 10 GHz spectrum, and b) zoom from 0 to 2 GHz.

3.4.1 L-band (1.400 GHz - 1.427 GHz)

This band is the most prone to RFI contamination because it is very close to the operation frequency of most consumer electronic devices. In populated areas, thousands of electronic devices are operating at the same time, and many of them introduce a large amount of RFI because of poor filtering or bad EMI enclosures. In Fig. 3.22a different types of interferences appears: permanent in time, like the one that appears in the 1.404 to 1.405 GHz subband; short with high bandwidth, like the one that appears at t = 11 s, and zoomed in Fig. 3.22b (around 20 MHz); and pulsed, like the ones appearing close to 1408 GHz with bandwidth of around 300 kHz as better noticed also in Fig. 3.22b. In Fig. 3.23a and 3.23b pulsed RFI with short time duration (around 100 ms), and small bandwidth (around 100 kHz) is also presented. The fluctuation is because each bin came from one sample.

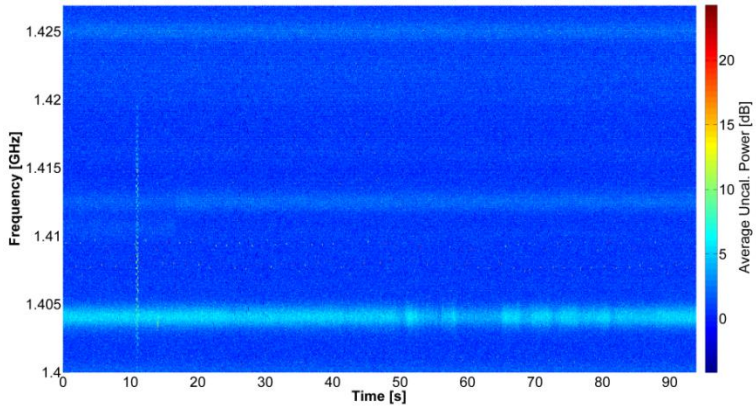

a.

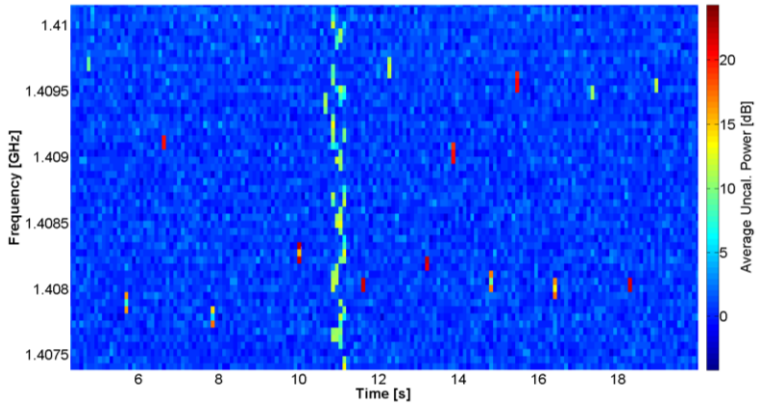

b.

Fig. 3.22 a) L-band survey from 1.400 to 1.427 GHz. at horizontal polarization, and b) zoom of Fig. 3.22a.

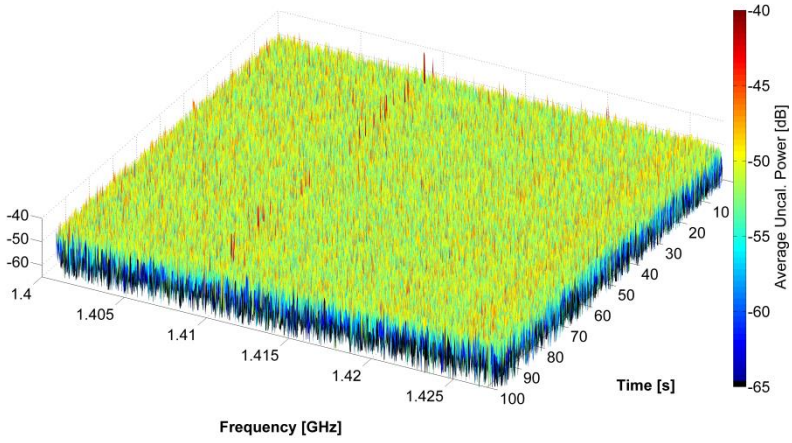

a.

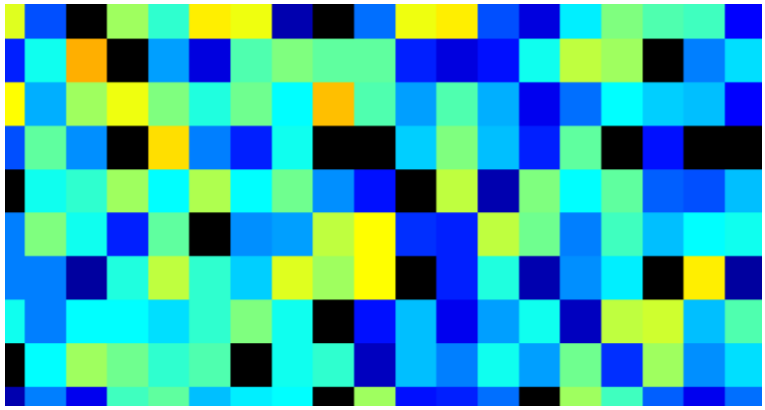

b.

Fig. 3.23 a) L-band survey from 1.400 GHz to 1.427 GHz. at horizontal polarization, and b) zoom of Fig. 3.23a.

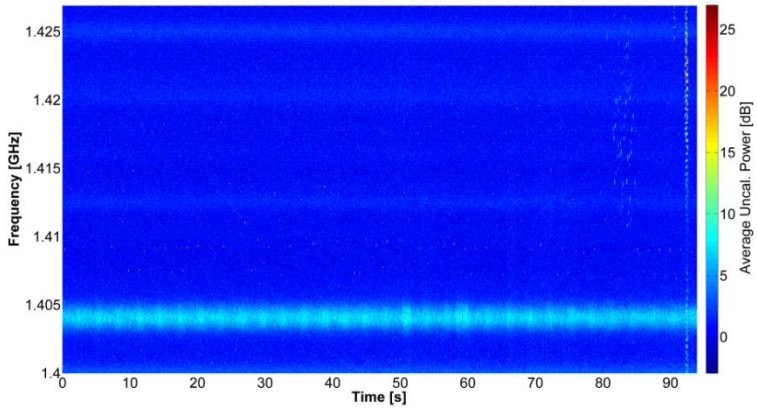

a.

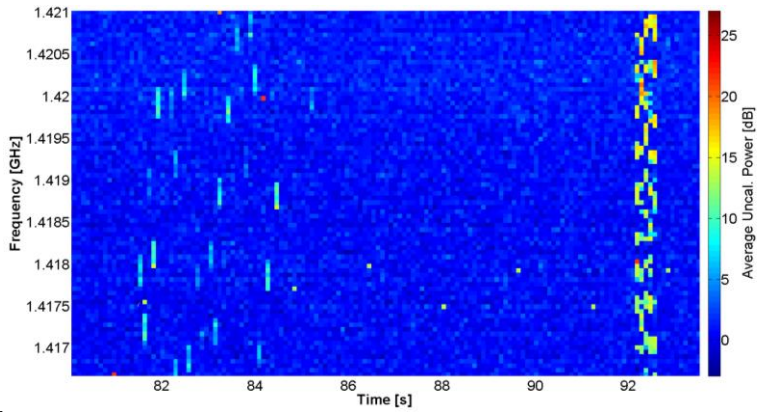

a.

b.

Fig. 3.24 a) L-band survey from 1.400 to 1.427 GHz. at vertical polarization, and b) zoom of Fig. 3.24a.

Vertical polarization survey exhibits similar interferences to the horizontal polarization one. Figure 3.24a shows the permanent in time (1.404 to 1.405 GHz subband); short duration with high bandwidth (around 92 s and zoomed in Fig. 3.22b); and pulsed (close to 1408 GHz). Figures 3.25a and 3.25b show pulsed RFI with short time duration (around 100 ms), and small bandwidth (around 100 kHz), the same type that appears at horizontal polarization.

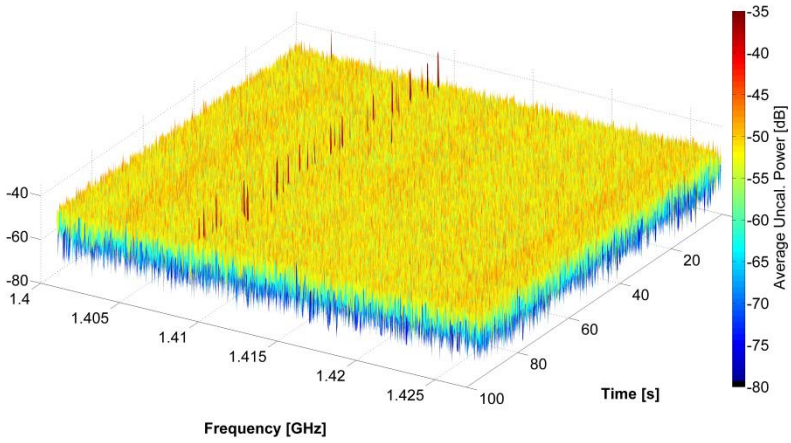

a.

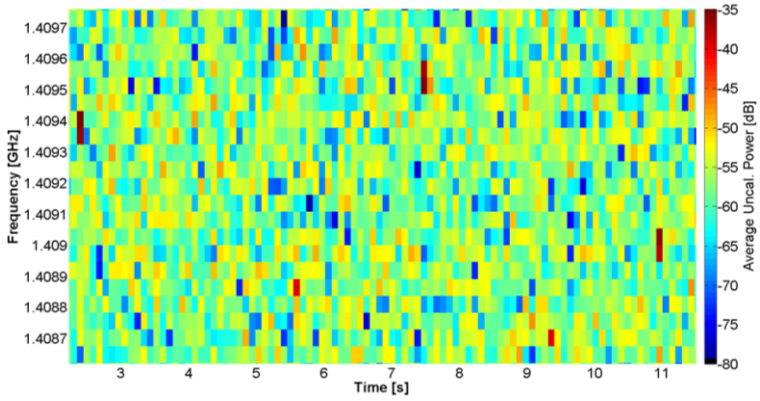

b.

Fig. 3.25 a) L-band survey from 1.400 to 1.427 GHz. at vertical polarization, and b) zoom of Fig. 3.25a. to show the relevant RFI's (in red) time duration ($t \approx 100$ ms) and bandwidth ($B \approx 100$ kHz).

3.4.2 S-band (2.69 GHz - 2.70 GHz)

S-band is another highly RFI-contaminated band, as it can be seen in Figs. 3.26 and 3.27. Having only 10 MHz of bandwidth, sporadic 100 kHz interferences at different times can contaminate most of the bandwidth. Wider interferences are less common, but affect almost the whole bandwidth as seen in 19 s, 33 s and 58 s of Fig. 3.26a and 25 s, 42 s, and 83 s of Fig. 3.27a.

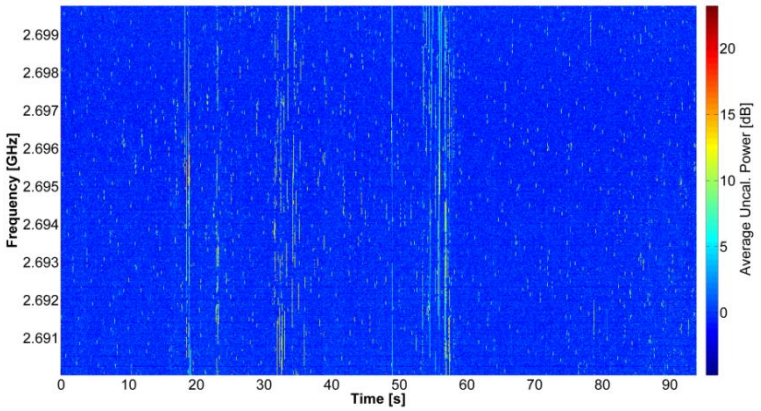

a.

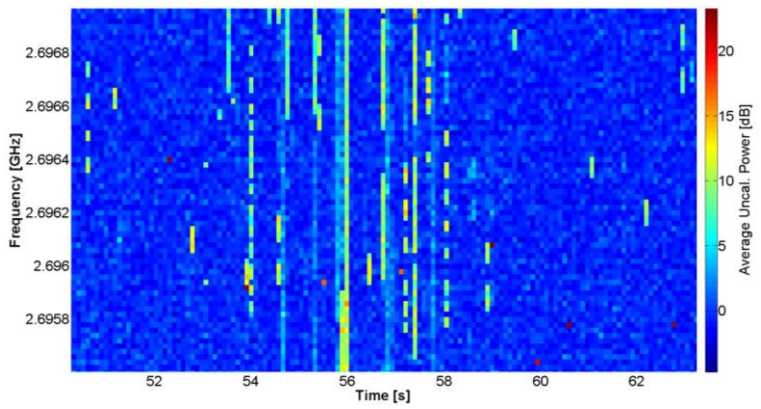

b.

Fig. 3.26 a) S-band survey from 2.69 to 2.7 GHz. at horizontal polarization, and b) zoom of Fig. 3.26a showing the relevant RFI's (in red and yellow) duration (t ≈ 100 ms), and bandwidth up to 10 MHz.

As it happens in other bands, vertical polarization exhibits similar interferences to horizontal polarization. This can be verified by comparing Fig. 3.26 with Fig. 3.27.

Here interferences that last t ≤ 100 ms, and with a bandwidth varying from around 10 kHz can be seen.

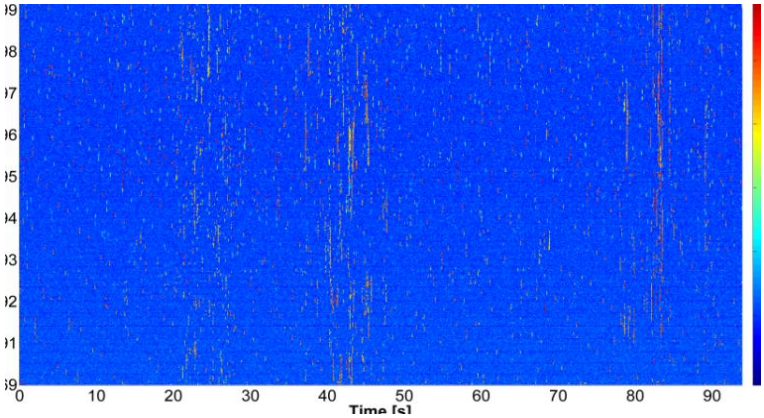

a.

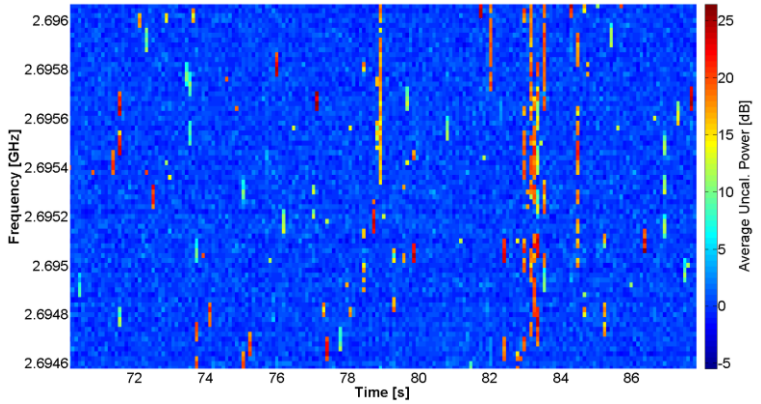

b.

Fig. 3.27 a) S-band survey from 2.69 to 2.7 GHz. at vertical polarization, and b) zoom of Fig. 3.27a.

3.4.3 C-band (7.14 GHz - 7.23 GHz)

At C-band sporadic 100 to 500 kHz interferences at horizontal and vertical polarizations are the only ones located during this survey, as shown in Figs. 3.28 and 3.29.

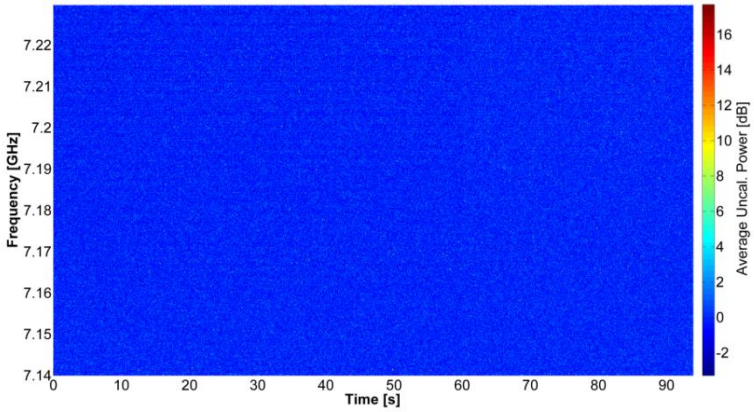

a.

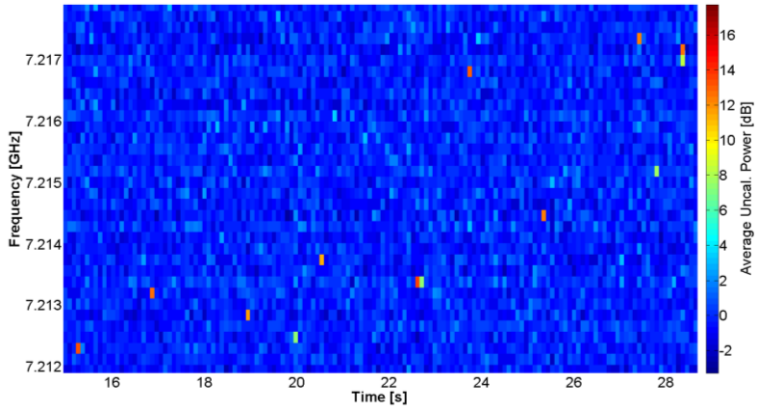

b.

Fig. 3.28 a) C-band survey from 7.14 to 7.23 GHz. at horizontal polarization, and b) zoom of Fig. 3.28a.

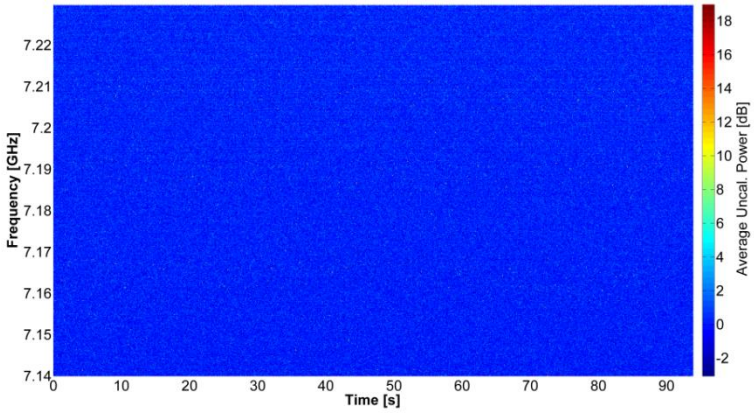

a.

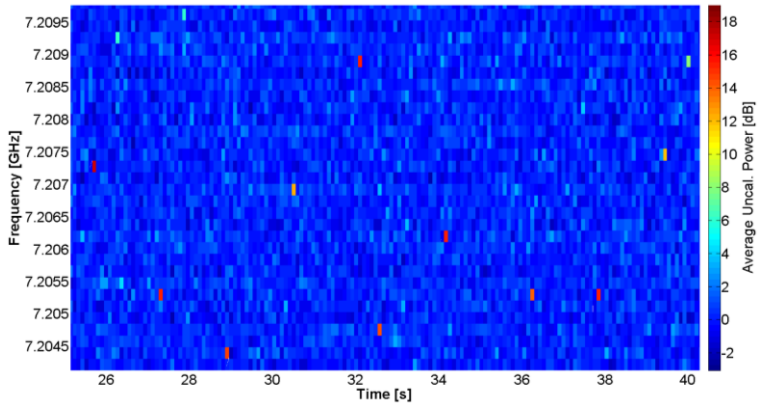

b.

Fig. 3.29 a) C-band survey from 7.14 to 7.23 GHz. at vertical polarization, and b) zoom of Fig. 3.29a.

3.4.4 X-band (10.68 GHz - 10.7 GHz)

The protected X-band starts to be cleaner than at L, S and C bands. Over the 20 MHz bandwidth, sporadic 100 to 500 kHz interferences are less probable, and occupy a smaller percentage of the spectrum as shown in Figs. 3.30, 3.31 and 3.32.

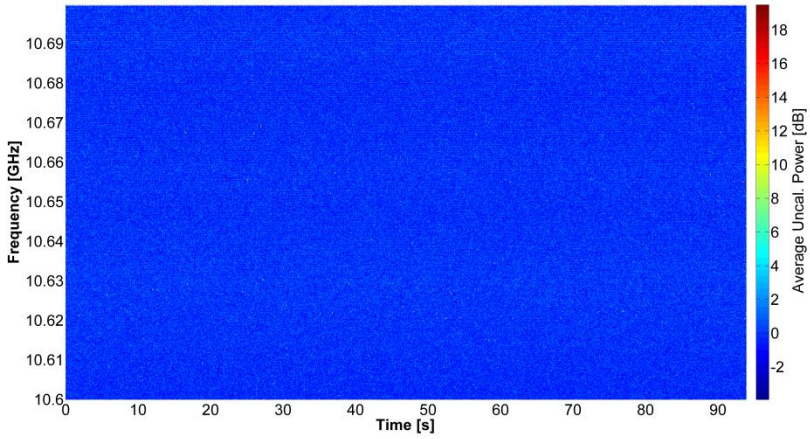

a.

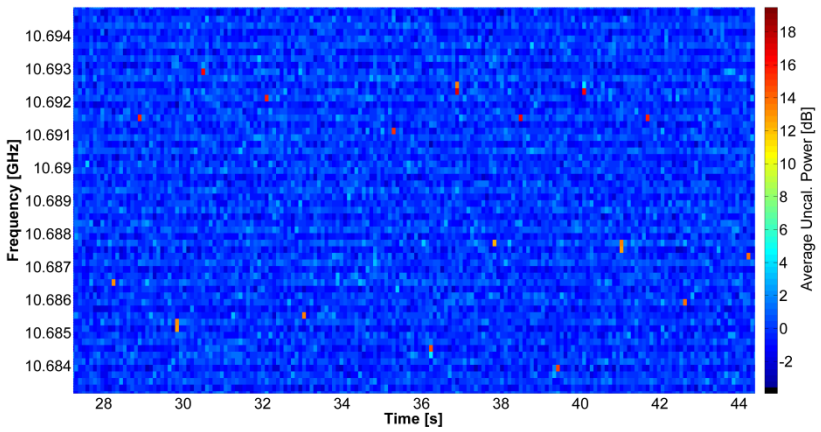

b.

Fig. 3.30 a) X-band survey from 10.6 to 10.7 GHz. at horizontal polarization, and b) zoom of Fig. 3.30a.

In Fig. 3.31 the typical 100 to 500 kHz RFI is presented very close to the 10.66 GHz. This is not part of the protected band (10.68 to 10.7 GHz), but it is also located on a band assigned for Earth exploration and space research. As in the other cases, those peaks could vary from 5 to 20 dB above the noise level.

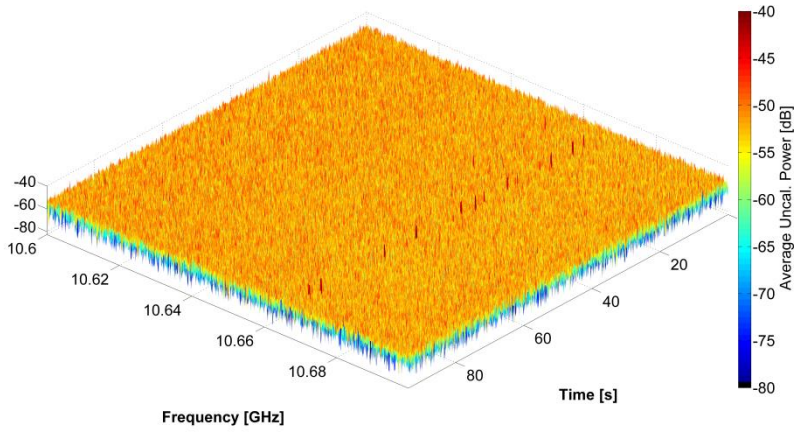

a.

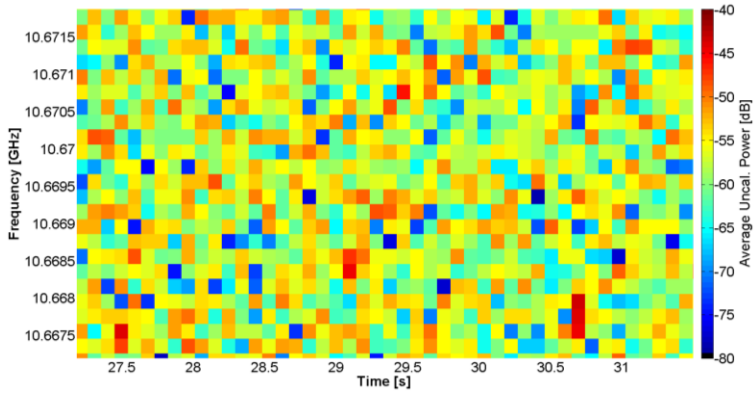

b.

Fig. 3.31 a) X-band survey from 10.6 to 10.7 GHz. at horizontal polarization, and b) zoom of Fig. 3.31a.

Vertical polarization shows similar interferences than the horizontal one, as illustrated in Fig. 3.32, between 10.68 and 10.69 GHz. Pulsed interferences of around 100 kHz bandwidth, and around 100 ms duration appears around every 900 ms in the 10.682 and 10.689 GHz subbands.

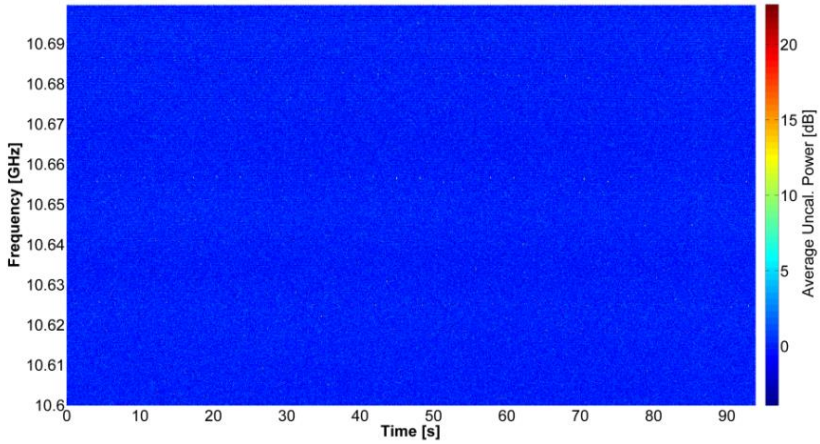

a.

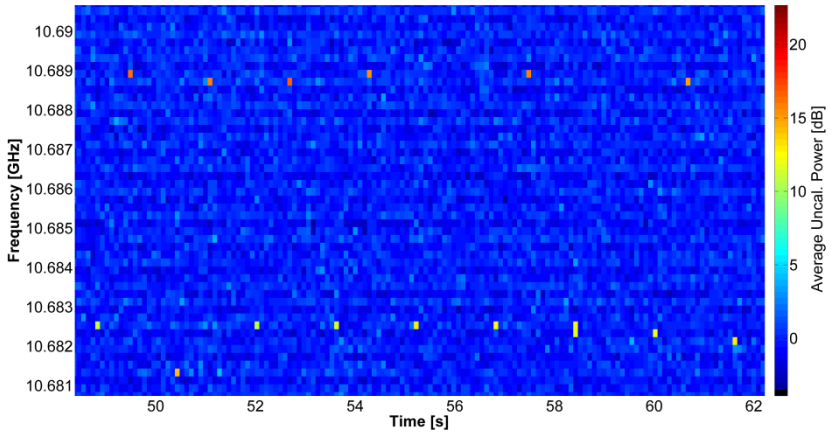

b.

Fig. 3.32 a) X-band survey from 10.6 to 10.7 GHz. at vertical polarization, and b) zoom of Fig. 3.32a.

Vertical polarization also has high peak (around 15 dB above the noise level), small bandwidth (around 500 kHz), and short duration (around 100 ms) periodic interference, as shown in Fig. 3.33

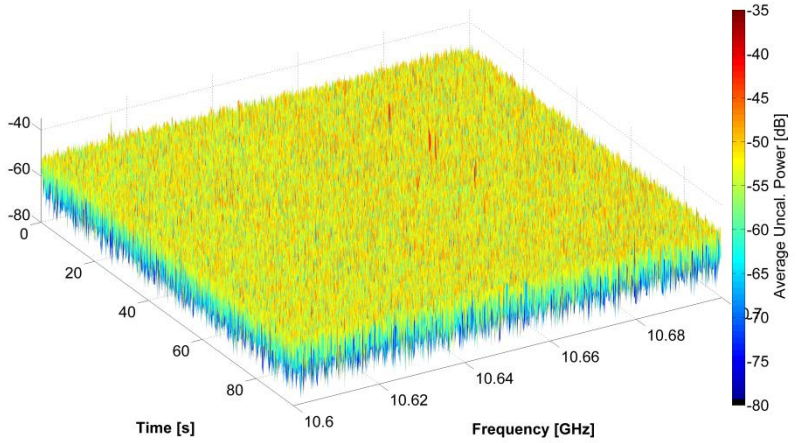

a.

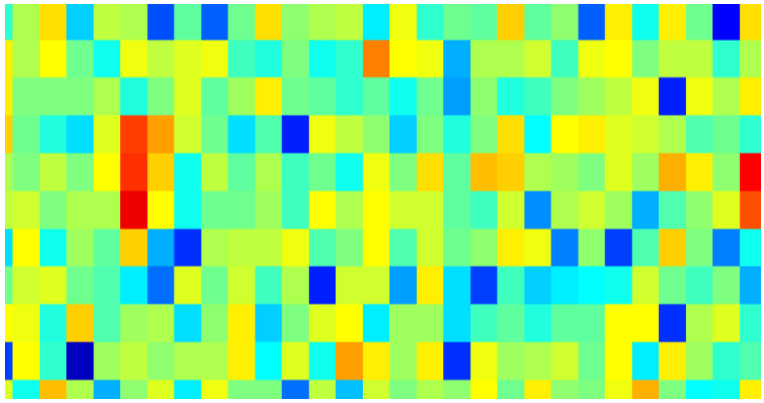

b.

Fig. 3.33 a) X-band survey from 10.6 to 10.7 GHz. at vertical polarization, and b) zoom of Fig. 3.33a.

3.4.5 K-band (18.6 GHz - 18.8 GHz) and (23.6 GHz - 24.0 GHz)

The K-band has assigned two sections of the spectrum: the first 200 MHz from 18.6 to 18.8 GHz, and the next 400 MHz from 23.6 to 24.0 GHz. The same pulsed RFI that appeared in the previous bands also appears in this band at both polarizations, as it can be seen in Fig. 3.34. However, every single narrowband interference of this type (around 100 to 500 kHz) just occupies a 0.083% of the spectrum at most ($100 \cdot 500$ kHz / 600 MHz $\approx 0{,}083$).

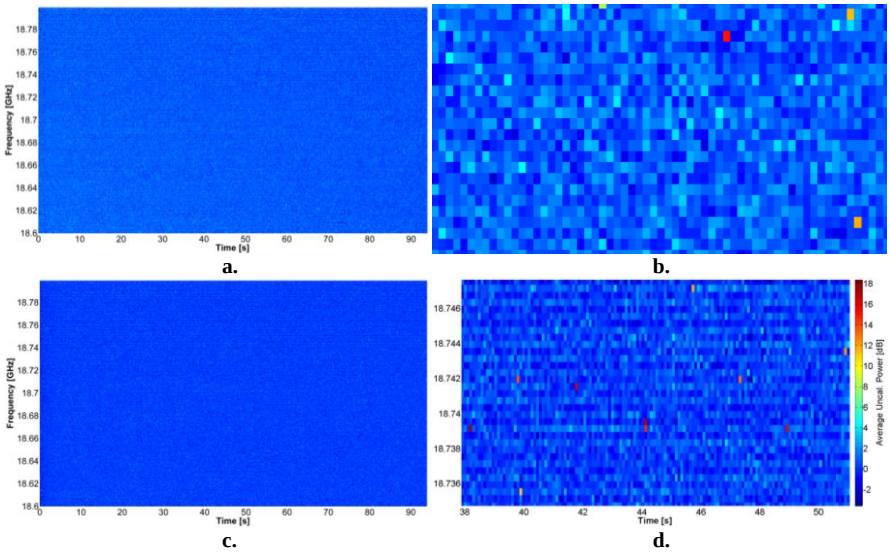

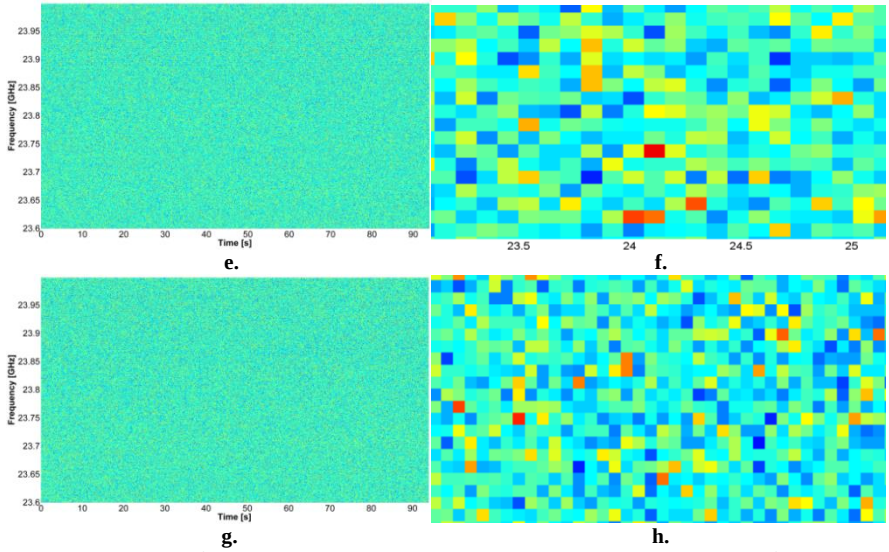

Fig. 3.34 K-band survey from 18.6 GHz to 18.8 GHz: a) Horizontal polarization. b) Zoom of Fig. 3.34a. c) Vertical polarization. d) Zoom of Fig. 3.34c. K-band survey from 23.6 GHz to 24.0 GHz. e) Horizontal polarization. f) Zoom of Fig. 3.34e. g) Vertical polarization. h) Zoom of Fig. 3.34g.

3.4.6 Ka-band (36 GHz - 37 GHz)

At Ka-band around 1 hour of measurements (38300 spectrum samples with 0.94 s between each one and 501 points in frequency) has been acquired. They are shown in Fig. 3.35, and looking the spectrograms only, the Ka-band seems to be RFI-free at horizontal polarization. However, in vertical polarization (Fig. 3.35b), the different power level in the subbands even after equalizing with a measurement using a matched load could be due to the stability of the amplifier, as can be seen in Table A.15. Using statistical analysis, as seen in Table 3.1, RFI can be detected in the survey because the kurtosis is outside the tolerance range, calculated as $K_{Range} = 3 \pm \sqrt{24/N}$. These parameters can be observed in more detail in Fig. 3.36.

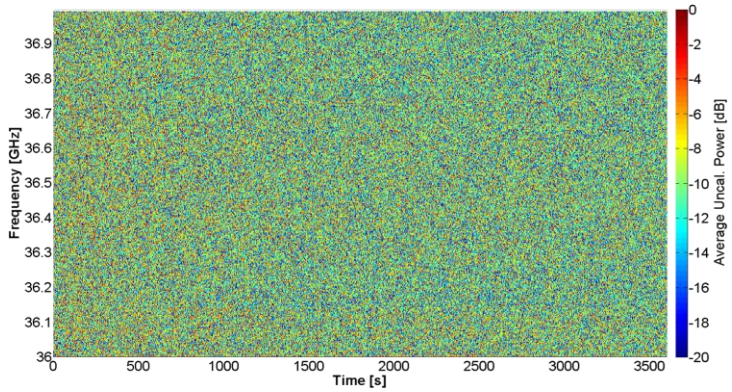

a.

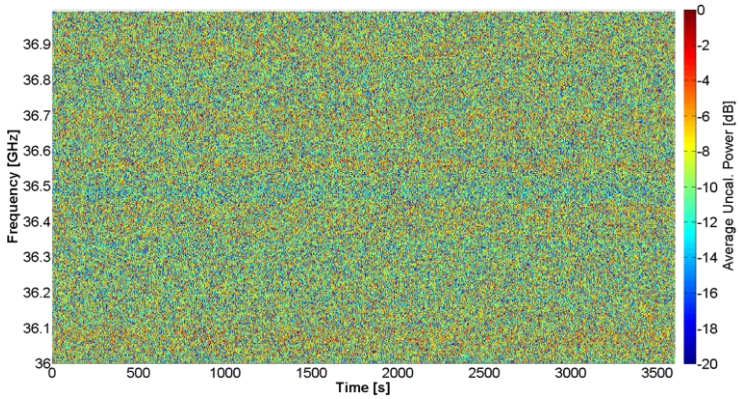

b.

Fig. 3.35 Ka-band survey. a) Horizontal polarization. b) Vertical polarization.

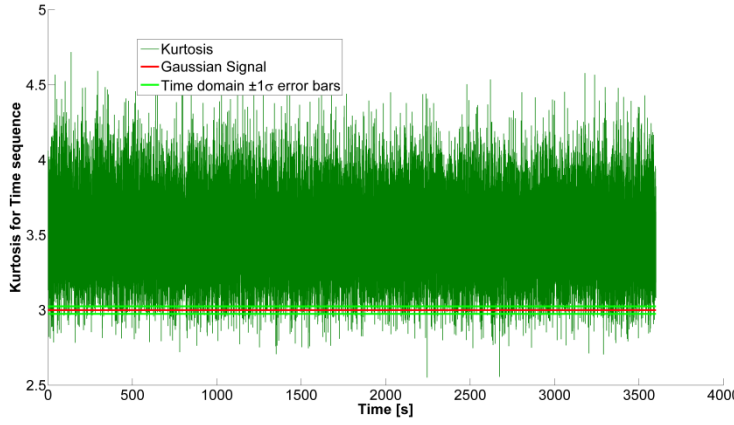

a.

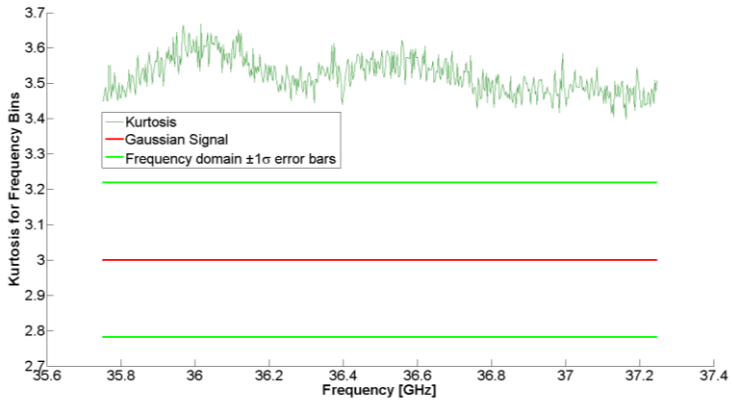

b.

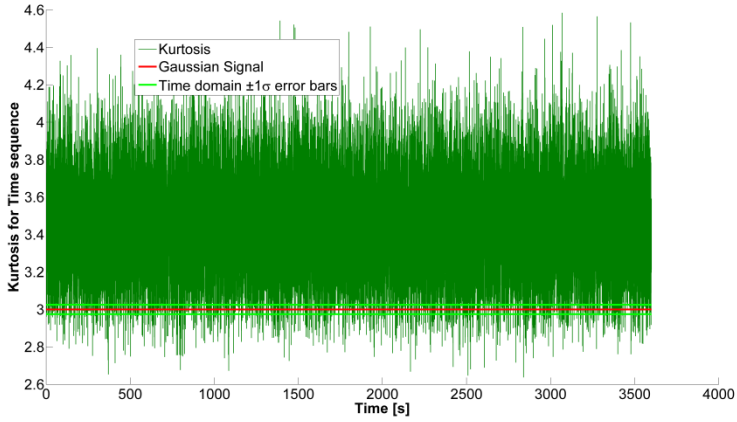

c.

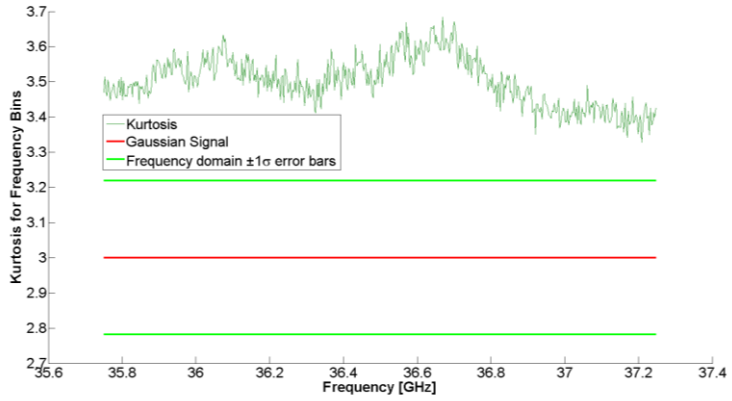

d.

Fig. 3.36 Ka-band Kurtosis. a) Horizontal polarization and Time domain. b) Horizontal polarization and Frequency domain. c) Vertical polarization and Time domain. d) Vertical polarization and Frequency domain.

Table 3.1 Kurtosis and Standard deviation for Ka-band survey

	Horizontal Polarization			Vertical Polarization		
	K	**K_{Range}**	**σ**	**K**	**K_{Range}**	**σ**
Time Sequence	3.49	3 ± 0.26	5.34	3.43	3 ± 0.25	5.40
Frequency Bins	3.52	3 ± 0.05	5.31	3.50	3 ± 0.07	5.31

3.4.7 W-band (86 GHz - 92 GHz)

As at Ka-band, 1 hour of data has been captured. Using statistical analysis (Table 3.2), RFI can be detected in the survey because the kurtosis is outside the tolerance range, calculated as $K_{Range} = 3 \pm \sqrt{24/N}$. These parameters can be observed in more detail in Fig. 3.38. An interesting fact is that at horizontal polarization, the Kurtosis in frequency-domain is in the RFI-free range (K = 3.03), while in time-domain it is outside the range (K = 2.65).

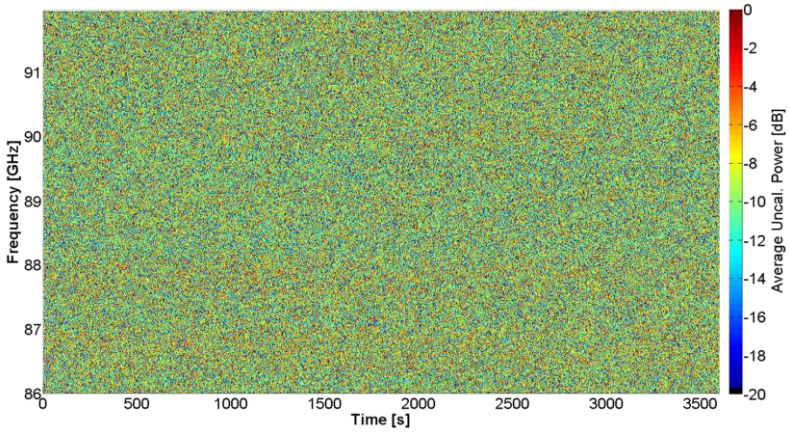

a.

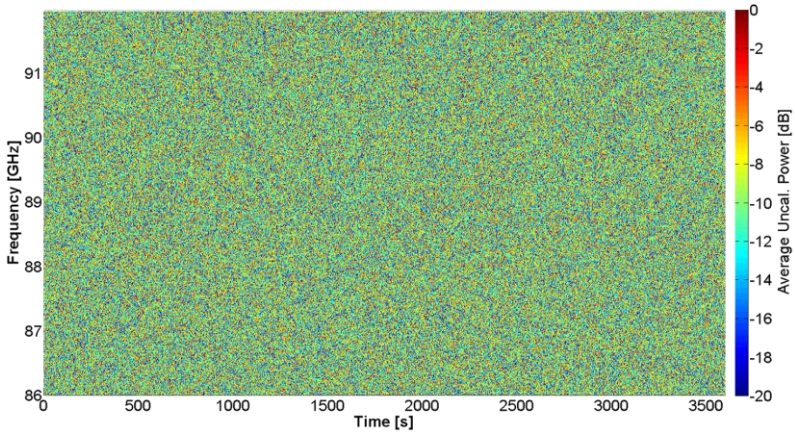

b.

Fig. 3.37 W-band survey. a) Horizontal polarization. b) Vertical polarization.

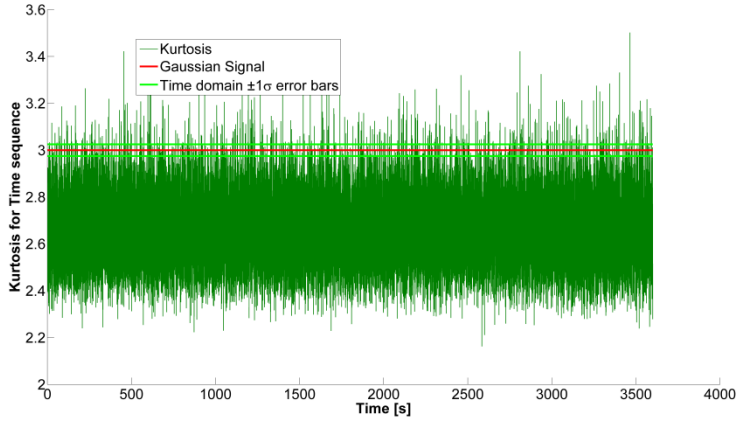

a.

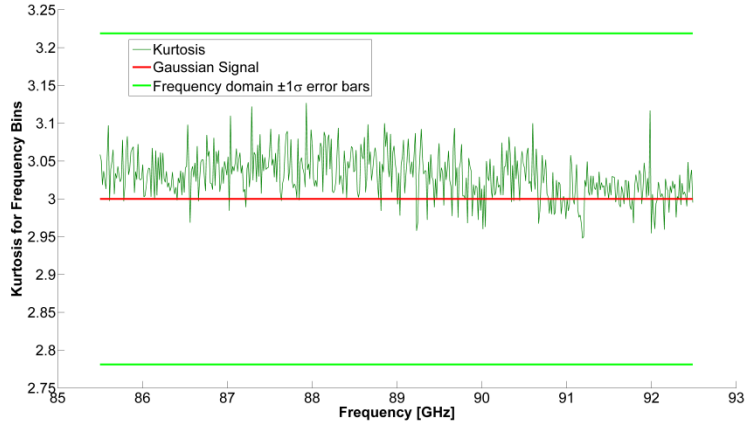

b.

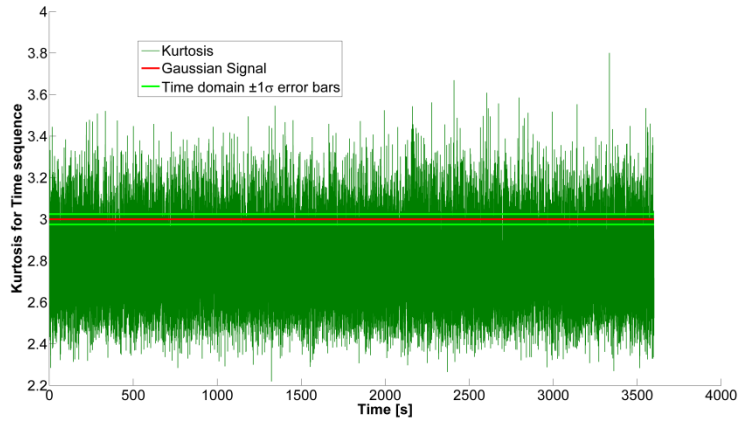

c.

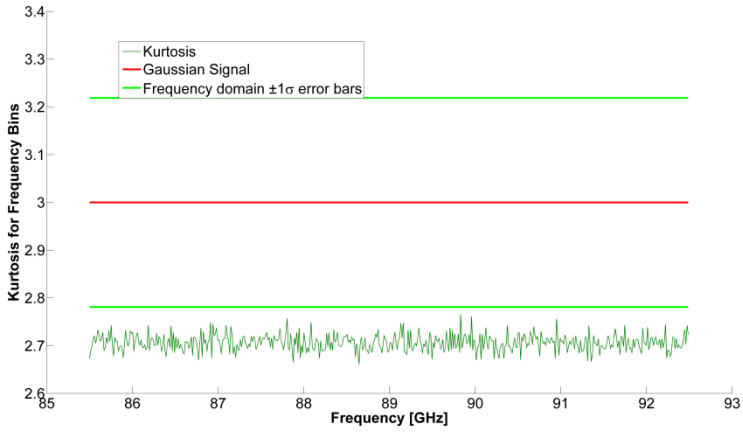

d.

Fig. 3.38 W-band Kurtosis. a) Horizontal polarization and Time domain. b) Horizontal polarization and Frequency domain. c) Vertical polarization and Time domain. d) Vertical polarization and Frequency domain.

Table 3.2 Kurtosis and Standard deviation for W-band survey

	Horizontal Polarization			**Vertical Polarization**		
	K	**K_{Range}**	**σ**	**K**	**K_{Range}**	**σ**
Time Sequence	2.65	3 ± 0.14	7.04	2.78	3 ± 0.18	5.09
Frequency Bins	3.03	3 ± 0.03	5.03	2.71	3 ± 0.02	4.61

3.5. CONCLUSIONS

This chapter has evidenced the presence of RFI in most of the radiometry protected bands.

Time and space RFI signatures help locating the direction of the RFI. If a second system is installed in another point, triangulation can be performed to detect the RFI location, and take the necessary actions to mitigate it.

A long survey in time and frequency-domain helps to establish patterns of the interferences, like contaminated subbands and time appearance of the RFI.

The L- and X-bands two-month surveys explained in Section 3.2 show that in Barcelona city L-band is the most contaminated one, more than 2% of the time, but some days can be up to 20%. On the other hand, the X-band is less than 0.1% of the time, and some eventual occasion can be up to 1%.

Time, frequency and space RFI signatures provide more information because for each direction they provide time and frequency-domain RFI maps. In the surveys made using this technique, several interferences have been detected, and by referencing it to a map the probable RFI source, like the communications tower, airport radar, city centre, etc. can be identified.

The MERITXELL radiometer is a multifrequency instrument operating in the protected radiometry bands from 1 to 100 GHz. The results of the surveys carried out with the MERITXELL demonstrate that the lower bands are more contaminated than the higher ones due to the frequency of operation of the wide variety of electronic devices. The higher ones seem to be cleaner, not only because the higher frequency, but also because of the much wider bandwidth, so a narrow band interference occupies a much smaller fraction of the band.

At L-band, many types of interferences appeared, short time high bandwidth, or long but located in a specific subband.

Some computer systems have also been found as potential interferers at GNSS L1 band, because some use similar clock frequencies [69].

Many RFI with short duration (~100ms) and bandwidths from 100 kHz up to 10 MHz contaminate the S-band at both polarizations. The RFI occupied time could be up to

5%. The common bandwidth contamination can be less than 5%, but some RFI can be in the whole band at arbitrary times.

C-, X-, and K-bands suffer contamination with small bandwidth (~ 100 kHz) and short time (<100 ms) pulsed RFIs. The performed survey indicates a contamination less than 1%.

Ka- and W-bands look RFI-clean, but after applying statistical techniques (in this case Kurtosis) RFI have been found in all bands because the kurtosis values clearly exceed the $\pm 1\sigma$ threshold. The only exception to this is the W-band horizontal polarization in frequency domain, where kurtosis values are inside the limits. However, W-band horizontal polarization in time domain shows clearly there is RFI.

Chapter 4

WAVELET-BASED RFI MITIGATION HARDWARE

In [39] a technique to mitigate RFI in microwave radiometry is proposed and analysed in detail, anyway it can be used to estimate RFI in many other fields [70]. It is based on the estimation of the RFI signal using wavelet denoising techniques, and its subtraction from the original signal so as to obtain an estimate of the noise itself.

4.1 METHODOLOGY

The system has been implemented using the Haar wavelet because is the most effective one in terms of computation time and space occupied into the FPGA. The hardware implementation is described in [71], based on the parameters studied in [39].

4.1.1 RFI estimation by Denoising: Principles

The interfering signal $s(t)$ (RFI) can be estimated without any a priori knowledge, and then subtracted from the received signal $x(t)$, to obtain a quasi RFI-free noise signal $\hat{n}(t)$ (Fig. 4.1).

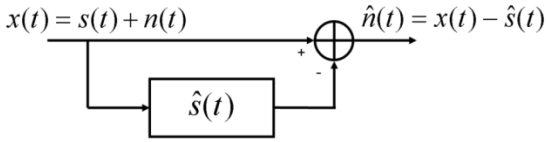

Fig. 4.1 RFI mitigation technique: an estimate of the RFI signal ŝ(t) is subtracted from the received signal x(t) to obtain a quasi RFI-free noise signal (from [39]).

A Wavelet Transform decomposes a discrete signal f into a first trend a^1 and a first fluctuation d^1: $f \rightarrow (a^1 \mid d^1)$. Because Wavelet analysis is based on multi-resolution analysis, the Wavelet transform is applied recursively first to the signal, and then to the trend obtained from this transform. The process is repeated a number L of steps (levels): $f \rightarrow (a^L \mid d^L \mid d^{L-1} \mid d^{L-2} ... \mid d^2 \mid d^1)$. After this, denoising is performed by discarding, neglecting or attenuating the coefficients that are below a predetermined level. The steps are the following:

- Computation of the wavelet transform of the data as they enter.
- Computation of the threshold coefficients.
- Computation of the inverse wavelet transform with the remaining components after thresholding.
- Subtraction of the denoised signal from the original one to estimate the noise.

To have a system operating in real time without collapsing the memory, the data must be processed before the next data block enters, as sketched in Fig. 4.2

4.1.2 Implementation Parameters Trade-off

The parameters that can be selected to optimize the performance of the generic algorithm described before are analysed in detail in [39], and are summarized below:

- **Wavelet family** or basis function used in the decomposition.
- **Thresholding method and threshold value**: The thresholding method can be either hard thresholding (sets to zero the wavelet coefficients smaller than a given threshold) or soft thresholding (sets to zero the wavelet coefficients smaller than a given threshold and shrinks the wavelet coefficients above that threshold).
- **Sequence length** or every single set of samples to apply the wavelet technique.
- **Decomposition level** or number of steps in which the process of decomposition into a signal trend and a fluctuation is repeated.

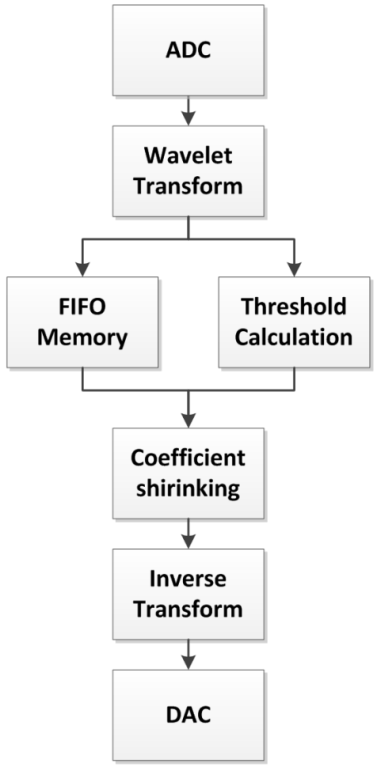

Fig. 4.2 Conceptual implementation of the pipelined method used to estimate the interfering signal ("denoised") with wavelets. The data appears at the same clock rate although with certain and fixed latency.

Other considerations:

- **Noise correlation due to oversampling**: The correlation between consecutive

noise samples was analysed in [39] and found to have a negligible impact in the interference mitigation (< 0.1 dB).

- **Quantization effects**: The analysis performed in [39] shows a negligible impact of the number of bits from 4 to 16, only barely distinguishable for Interference to Noise Ratios (INR) < -20 dB.
- **Computational requirements** are strongly dependent on the wavelet type and sequence length. Results are shown in Fig. 4.3 (adapted from [39]) for different wavelet types. There is an important trade-off between the achievable interference rejection (depending on the wavelet type and mainly sequence length), and the computational complexity which must be evaluated depending on the application.

After a careful analysis of the state of the art FPGAs, it was considered that only a sub-optimum algorithm could be implemented for a real-time application. The final selected parameters are:

- **Wavelet family**: Due to the very demanding computational requirements the Haar transform is selected, since it requires the simplest mathematical operations (sums and differences). In this case, the Haar wavelet can be implemented efficiently in real time operation hardware, and it requires fewer operations than other types of wavelet families. In addition, it was proved that it has good signal rejection rate against different kinds of RFI signals. As explained later, divisions by $\sqrt{2}$ will not be performed during the decomposition process, but they will be taken into account in the thresholding**.**
- **Thresholding method and threshold value [39, 72]**: A hard thresholding method is applied for simplicity, and to facilitate the computation of the threshold (especially in a real-time application). While the Stein's Unbiased Risk Estimate (SURE) [73] method performs better than the Universal method for choosing threshold value, the last one is used because it can be implemented in hardware for real time calculation. This last method is explained in Section 4.2.2.
- **Number of samples**: The number of samples is limited to 2^{17}, which is a set of samples sufficient large to estimate interference signals with samples per period up to 10^5 samples.

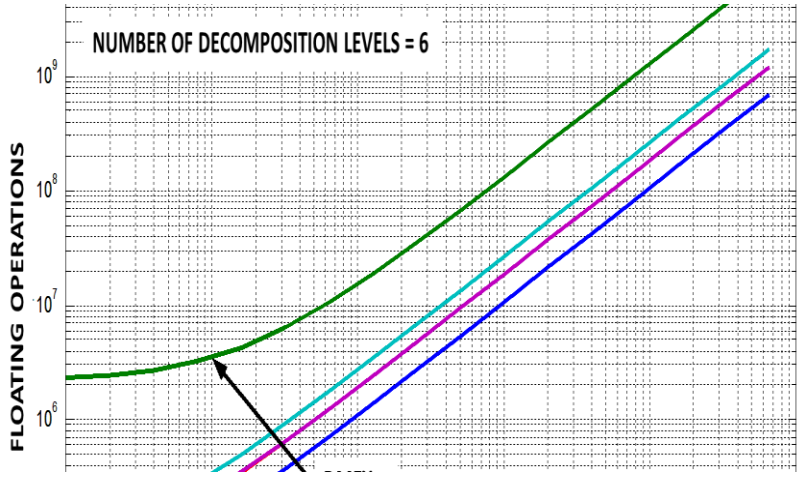

a.

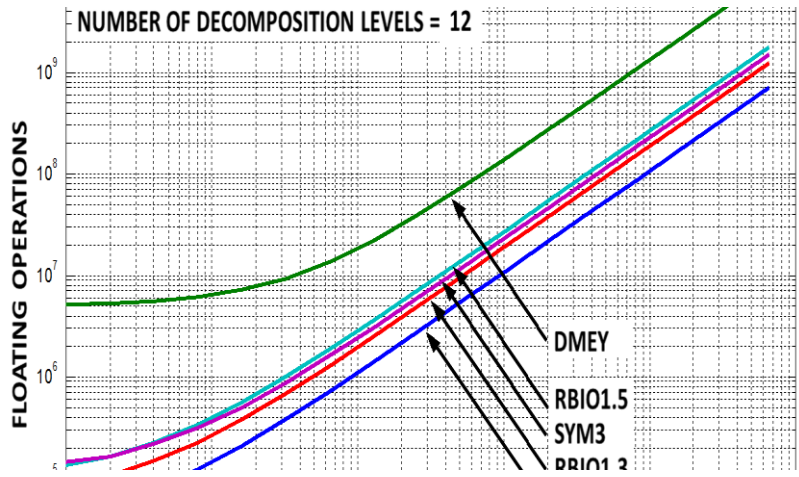

b.

Fig. 4.3 In the vertical axis the number of floating operations required by the RFI cancellation algorithm (INR = 100) vs. sequence length in the horizontal axis, for different wavelet types and decomposition levels equal to a) 6 levels, and b) 12 levels (adapted from [39]).

- **Decomposition level:** While the difference between 6 and 12 decomposition levels is small (Figs. 4.3a and 4.3b) for coefficient multi-scaling (different scaling for every decomposition level), as compared to the dependence with the wavelet family and sequence length, using coefficient single scaling the selected decomposition level is 12 to improve the performance in front of spread-spectrum signals.
- **Number of bits:** For RFI mitigation purposes 4 bits was the minimum required

for a ±3.5·σ ADC window [39]), but in [70] it was shown that for a ±4.05·σ ADC window, and 8 bits quantization, the estimated antenna temperature error was smaller than 0.01 K. For convenience, in our system the default number of bits is set to 12 for each ADC, although it can be decreased internally to minimize memory requirements.

4.2 HARDWARE IMPLEMENTATION

4.2.1 Real-Time Computation of the Haar Transform Coefficients

A real-time wavelet transform has been implemented in order to obtain the Haar transform coefficients (trend and fluctuations) at one clock cycle after the last data sample enters in the set. In our case this means latency between input and output is $2^{17\text{th}}$ samples multiplied by clock period.

One thing to take into account is that classical Haar Wavelet transform requires a factor of √2 in the denominator and it may become an important computational effort for the hardware. In this implementation, this problem has been solved by applying twice this √2 factor when the inverse transform and threshold coefficients are calculated. This leads to a scaling factor of 2 that is straightforward in binary systems.

Thus, the 1-level classical Haar transform coefficients are obtained as shown in Eqn. 4.1, for m = 1, 2, 3… $N/2$ where $N=2^{17}$.

$$a_m = \frac{f_{2m-1} + f_{2m}}{\sqrt{2}}, \tag{4.1a}$$

$$d_m = \frac{f_{2m-1} - f_{2m}}{\sqrt{2}}. \tag{4.1b}$$

The next level is obtained by applying the transform to the previous level trend coefficients only (a_m). From this, the following general formula is obtained (Eqn. 4.2), with l = level and m = 1, 2, 3… $N/2$.

$$a_m^l = \frac{a_{2m-1}^{l-1}}{\sqrt{2}} + \frac{a_{2m}^{l-1}}{\sqrt{2}}, \tag{4.2a}$$

$$d_m^l = \frac{a_{2m-1}^{l-1}}{\sqrt{2}} - \frac{a_{2m}^{l-1}}{\sqrt{2}}. \tag{4.2b}$$

As it has been noticed, since all operations are sums and differences the denominator can be extracted as shown in Eqn. 4.3:

$$k_l = \frac{1}{2^{l/2}}. \tag{4.3}$$

Therefore, Eqns. 4.2a and 4.2b become 4.4a and 4.4b, provided that the factor in Eqn. 4.3 is taken into account during the threshold coefficient calculation and the inverse transform process:

$$a_m^l = a_{2m-1}^{l-1} + a_{2m}^{l-1}, \tag{4.4a}$$

$$d_m^l = a_{2m-1}^{l-1} - a_{2m}^{l-1}. \tag{4.4b}$$

4.2.2 Computation of the Threshold Coefficients

For the sake of implementation efficiency the Universal method is used to compute the threshold. As shown in Eqn. 4.5, it assigns a threshold level equal to the noise standard deviation times a constant, where l = level, and N = number of samples. Note that coefficient correction $\left(\sqrt{2}\right)^l$ is applied because it was removed when calculating the transform in Eqns. 4.4a and 4.4b.

$$Threshold_l = \left(\sqrt{2}\right)^l \cdot \sqrt{2 \cdot \log(N)} \cdot \sigma(c_l). \tag{4.5}$$

The standard deviation is computed in real time using Eqn. 4.6 which has while data is being processed.

$$\sigma = \sqrt{\frac{1}{k}\sum_{i=1}^{k} c_i^2 - \bar{c}^2}. \tag{4.6}$$

The total latency of the threshold coefficient computation step is of the order of N clock cycles where N is the number of samples per block (as said N=2^{17}). These values are determined by the specific hardware implementation of the operations.

4.2.3 Coefficient Shrinking Process

The coefficient shrinking process consists of discarding all fluctuation coefficients which are above the previously calculated threshold value as in Eqn. 4.7.

$$a_k^l = a_k^l, \tag{4.7a}$$

$$d_k^l = \begin{cases} 0, & d_k^l >= Threshold_l, \\ d_k^l, & d_k^l < Threshold_l. \end{cases} \tag{4.7b}$$

This process is equivalent to estimate the RFI signal by keeping fluctuation coefficients above a threshold and subtracting this value from the original input signal.

4.2.4 Inverse Haar Transform

The classical inverse Haar transform takes coefficients ($a^1 \mid d^1$) back to the original signal f by means of Eqn. 4.8.

$$f = \left(\frac{a_1 + d_1}{\sqrt{2}}, \frac{a_1 - d_1}{\sqrt{2}}, ..., \frac{a_{N/2} + d_{N/2}}{\sqrt{2}}, \frac{a_{N/2} - d_{N/2}}{\sqrt{2}} \right). \tag{4.8}$$

For multilevel resolution, the highest level coefficients are replaced, obtaining Eqn. 4.9, with *n* = highest resolution level, and *i* = sample number.

$$f_i = \frac{a^n}{k^n} + \sum_{j=1}^{n} \left(\frac{1}{k^j} \right) \cdot \left(-1^{\left(\frac{i-1}{2^{j-1}} \right)} \right) \cdot \left(d^j_{\left(\frac{i+2^j-1}{2^j} \right)} \right). \tag{4.9}$$

As noticed at the beginning of this section, the inverse Haar transform must be calculated dividing by a factor of 2, each resolution level instead of $\sqrt{2}$. Hence, the calculation leads to Eqn. 4.10 for every single sample at the output of this system.

$$f_i = \frac{a}{2^L} + \sum_{j=1}^{L} \left(\frac{(-1)^{\left\lfloor \frac{i}{2^j} \right\rfloor}}{2^j} \cdot d^j_{\left\lfloor \frac{i}{2^j} \right\rfloor} \right) \qquad i = 1,2 \ldots N. \tag{4.10}$$

4.3 HARDWARE DESCRIPTION

The hardware used for the data conversion and implementation of the signal processing algorithms includes a Xilinx KC705 base board with the Kintex 7 FPGA (Fig. 4.4).

The FMC150, red board in Fig. 4.4, is a four channel Analogue to Digital Converter

(ADC) and Digital to Analogue Converter (DAC) FPGA Mezzanine Card (FMC). The card provides two 14-bit A/D channels and two 16-bit D/A channels which can be clocked by an internal clock source, optionally locked to an external reference, or an externally supplied sample clock. The design is based on a dual channel 14-bit 250Msps ADC and a dual channel 16-bit 800Msps DAC. The FMC150 allows a flexible control of sampling frequency, analogue input gain, and offset correction through serial communication. Its block diagram is shown in Fig. 4.5.

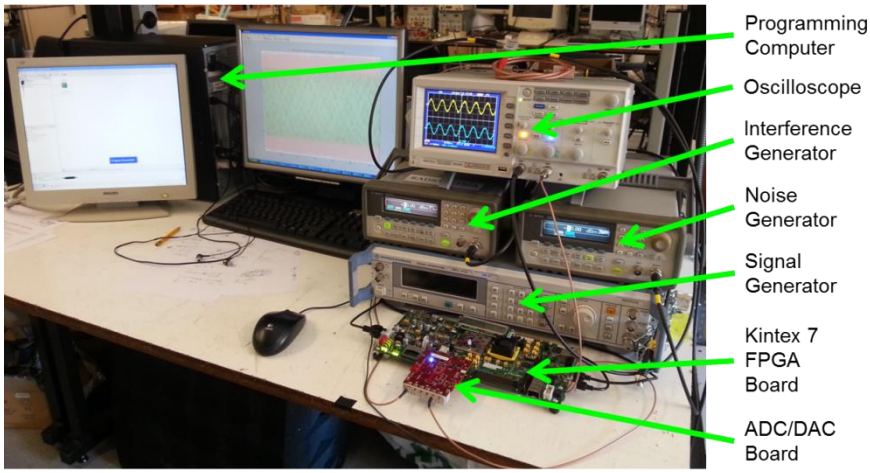

Fig. 4.4 Xilinx KC705 base board with the Kintex 7 FPGA used in this work. In the bottom right comes the FPGA board with the ADC can be seen. Behind the FPGA, there is a signal generator to convert the signal to baseband and returning it to the original frequency after removing the interference. Over the signal generator, a noise generator and interference generator. On the top right corner, an oscilloscope showing the original interference in yellow, and the estimated are on cyan.

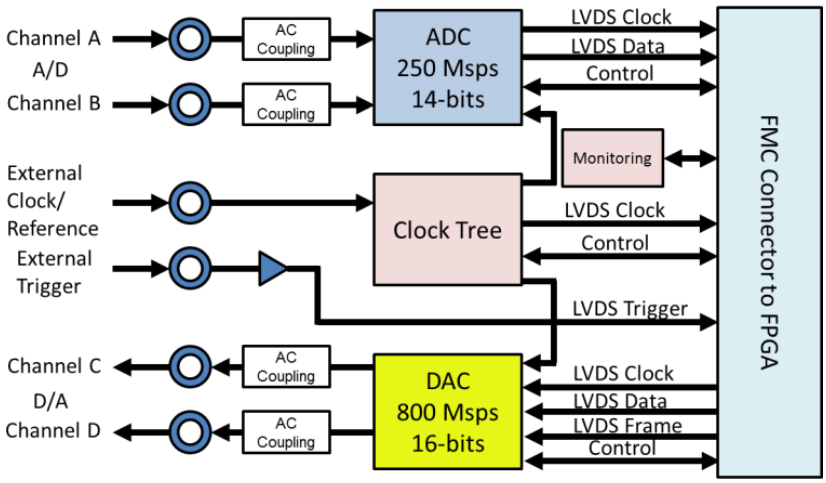

Fig. 4.5 FMC150 ADC/DAC Block Diagram.

The resources used in the Xilinx Kintex 7 FPGA for this system are shown on Table 4.1. Notice there is much free space for implementing more algorithms alongside wavelet denoising. The data output rate is one sample per clock cycle and the estimated latency between the sample and its interference removed version is 534 μs.

Table 4.1 xc7k325t-2ffg900 FPGA utilization (adapted from [74])

Device Utilization Summary (estimated values)			
Logic Utilization	**Used**	**Available**	**Utilization**
Number of Slice Registers	33125	407,600	8%
Number of Slice LUTs	37597	203,800	8%
Number of LUT-FF pairs used	44907	44907	100%
Number of bonded IOBs	205	500	29%
Number of Block RAM/FIFO	208	445	46%
Number of BUFG/BUFGCTRLs	9	32	37%
Number of DSP48E1s	63	840	7%

4.4 SIMULATION RESULTS

In order to have a well-defined and controlled evaluation scenario, numerically generated signals (noise plus different types of interference at different power levels) have been uploaded into the FPGA memory for later processing. The hardware implementation of the wavelet system is explained in [71, 74].

Simulations and hardware tests include sinusoidal interfering signals at power levels from -30 dB to +30 dB with respect to the noise power, for different samples per period from 1 to $4 \cdot 10^9$ (this value is unrealistically high, but is included to show the

saturation effect caused by the limitation of the number of samples used in the calculation).

In Fig. 4.6a, it is seen that for a 20 samples per period (or sequence length), sinusoidal RFI of INR = +20 dB is attenuated by almost a factor of 20, while for INR = 0 dB, the attenuation is just a factor of 2. In order to increase the interference attenuation, the number of samples per period must be increased, e.g. for 100 samples per period, sinusoidal RFI of INR = +20 dB is attenuated by a factor of ~19 dB, while for INR = +0 dB, the attenuation is a factor of 6 dB, and for 1000 samples per period, sinusoidal RFI of INR = +20 dB is attenuated by a factor of 27 dB, while for INR = +0 dB, the attenuation is a factor of 17 dB. To compare it with other types of signals, Pseudo-Random Noise (PRN) RFI mitigation is shown in Fig. 4.6b, and it saturates faster than sinusoidal RFI. Median filtering method for RFI mitigation is shown in Fig. 4.6c and is noticeable that saturates much faster than the wavelet denoising method.

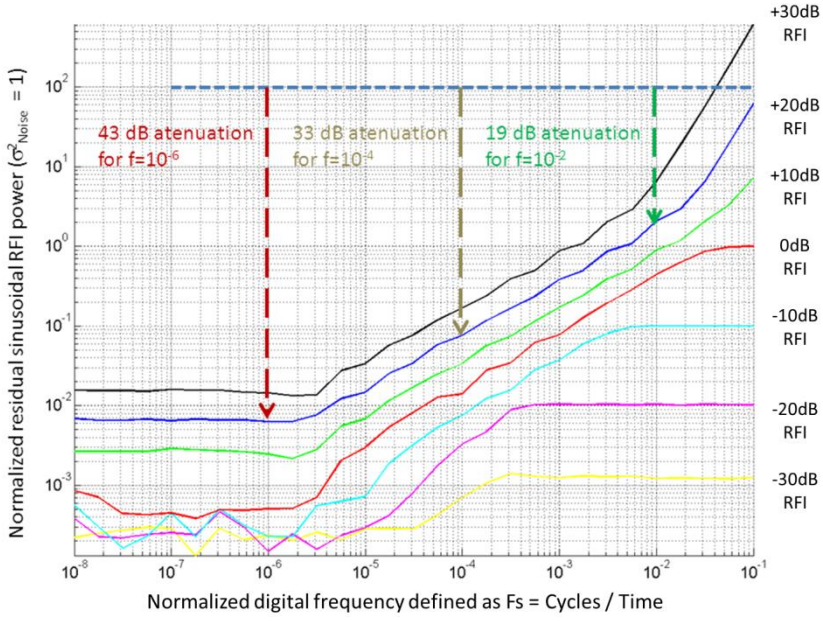

a.

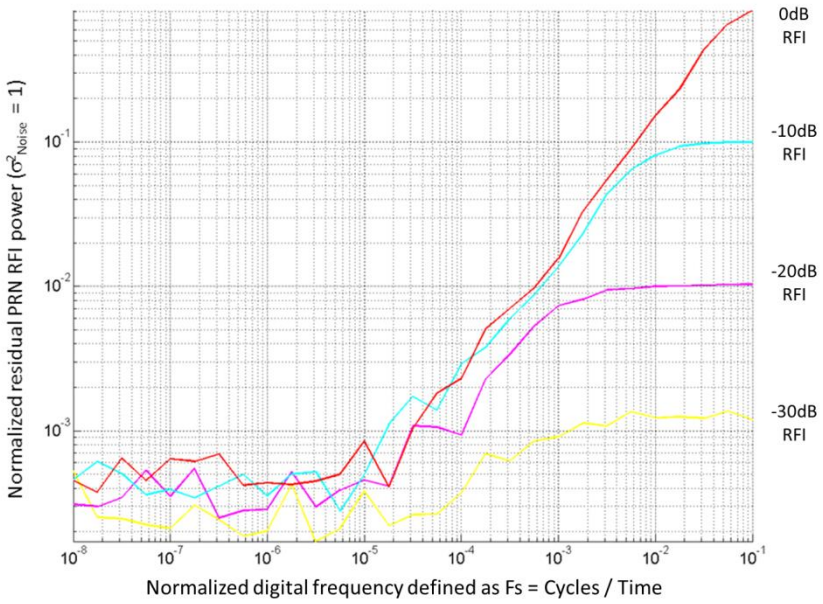

b.

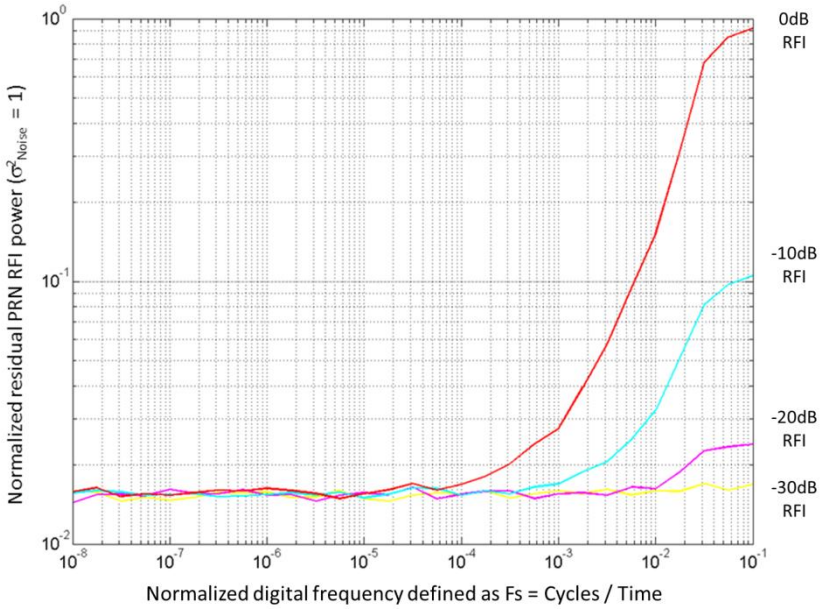

c.

Fig. 4.6 Normalized residual RFI power (σ^2_{Noise} = 1) vs. normalized digital frequency defined as Fs = Cycles / Time for different INR: +30 dB (black); +20 dB (blue), +10 dB (green); 0 dB (red); -10 dB (cyan); -20 dB (magenta), and -30 dB (yellow) for different interferences and methods (from [71]):
a) Sinusoidal, b) PRN interferences using Haar Wavelet Denoise, and c) PRN interference using Median filtering technique.

Figures 4.7a to 4.7*l* illustrate the performance and results of the RFI estimation process with different INRs for a set of 2^{21} samples, with 36,000 per period (18,000 times the Nyquist sampling frequency). Figure 4.7m shows the results when the number of samples is 4096 with just 36 samples per period (18 times Nyquist sampling frequency), the minimum required for an effective threshold estimation. Note that the performance of the technique improves for higher INRs. In the Figs. 4.7 and 4.8, it can be noticed that the wavelet modelling of the signal is much better for larger interferences, while for weaker interference powers, the modelling get worse. Mitigating sinusoidal RFI is shown in Fig. 4.7, and PRN RFI on Fig. 4.8.

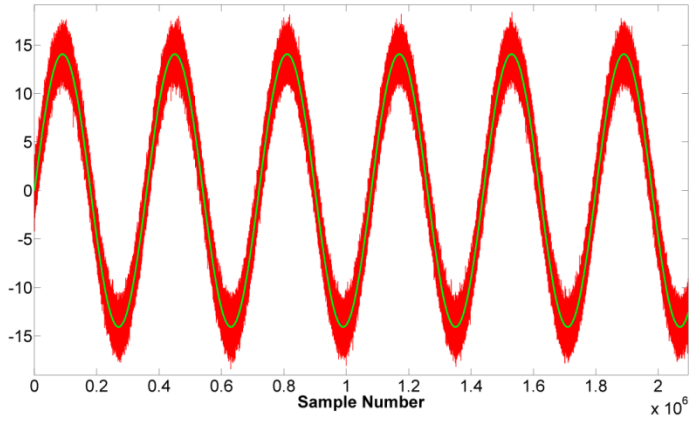

a.

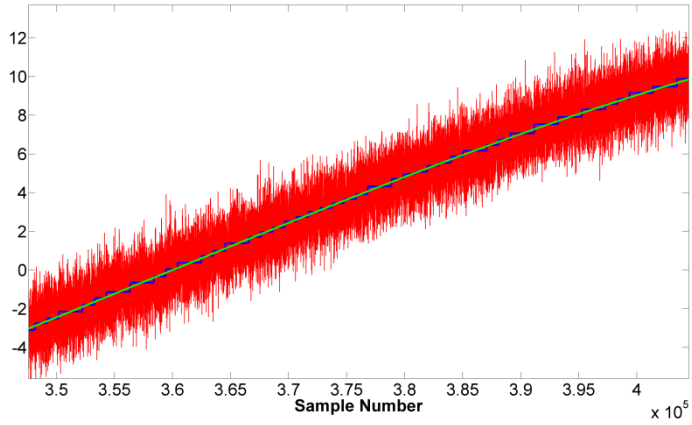

b.

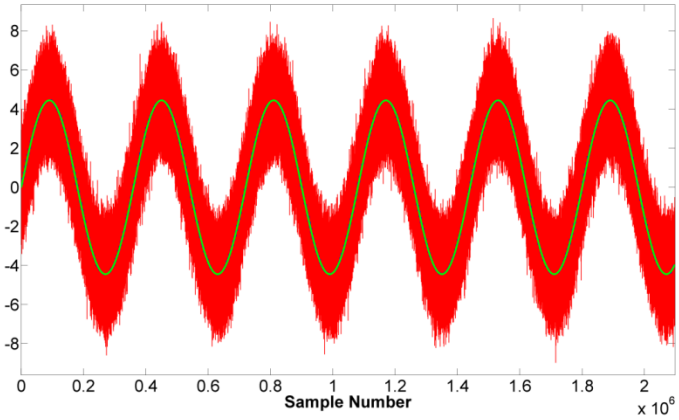
8
6
4
2
0
-2
-4
-6
-8
0
0.2
0.4
0.6
0.8
1
1.2
1.4
1.6
1.8
2
Sample Number
x 10^6

c.

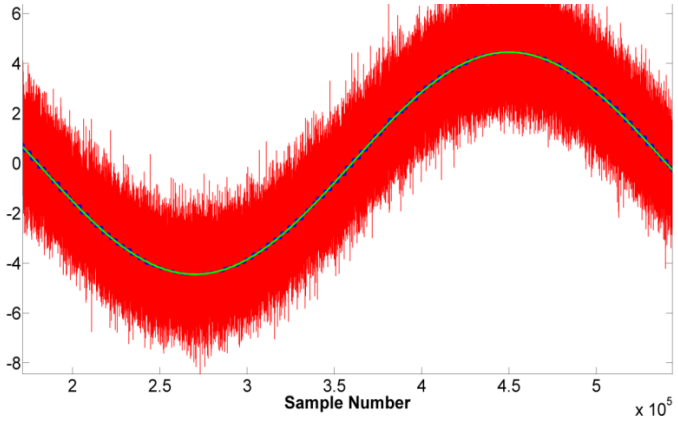
6
4
2
0
-2
-4
-6
-8
2
2.5
3
3.5
4
4.5
5
Sample Number
x 10^5

d.

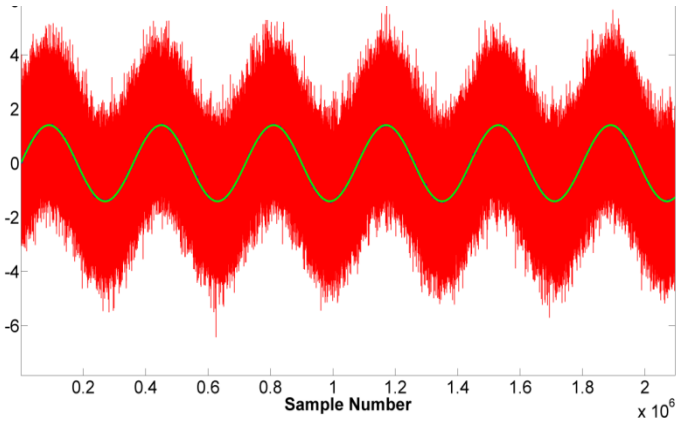
4
2
0
-2
-4
-6
0.2
0.4
0.6
0.8
1
1.2
1.4
1.6
1.8
2
Sample Number
x 10^6

e.

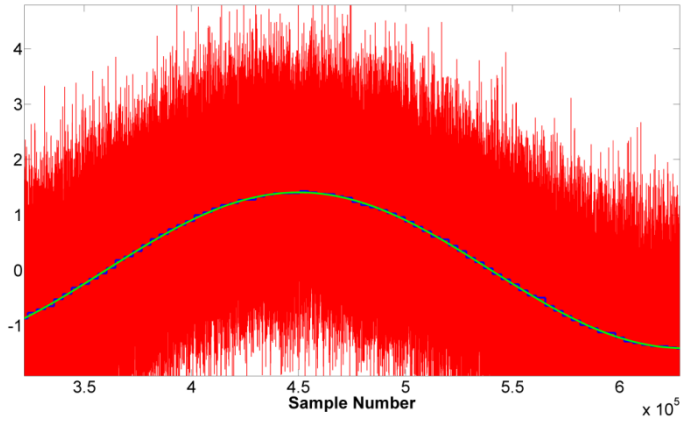
4
3
2
1
0
-1
3.5
4
4.5
5
5.5
6
Sample Number
x 10^5

f.

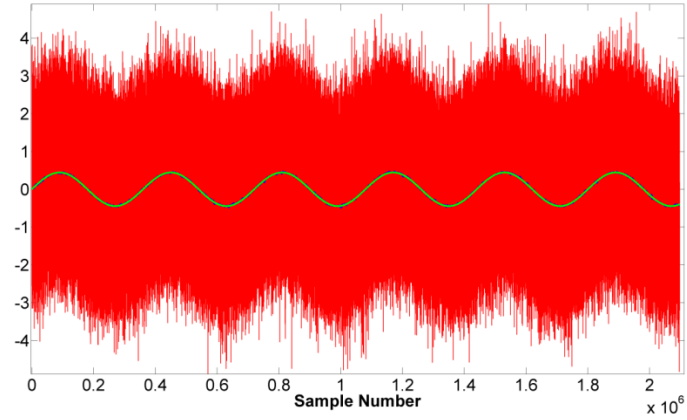
4
3
2
1
0
-1
-2
-3
-4
0
0.2
0.4
0.6
0.8
1
1.2
1.4
1.6
1.8
2
Sample Number
x 10^6

g.

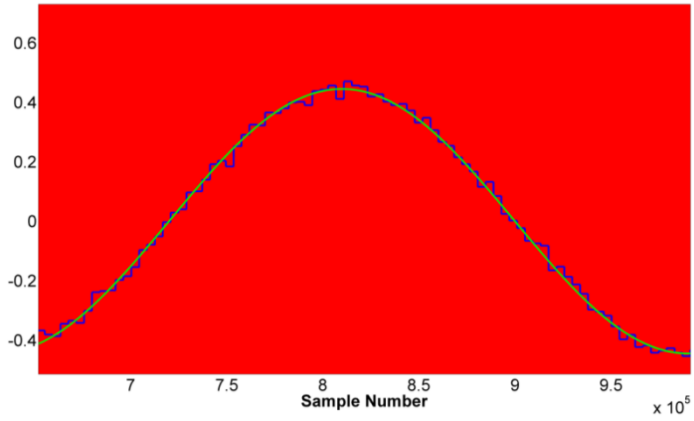
0.6
0.4
0.2
0
-0.2
-0.4
7
7.5
8
8.5
9
9.5
Sample Number
x 10^5

h.

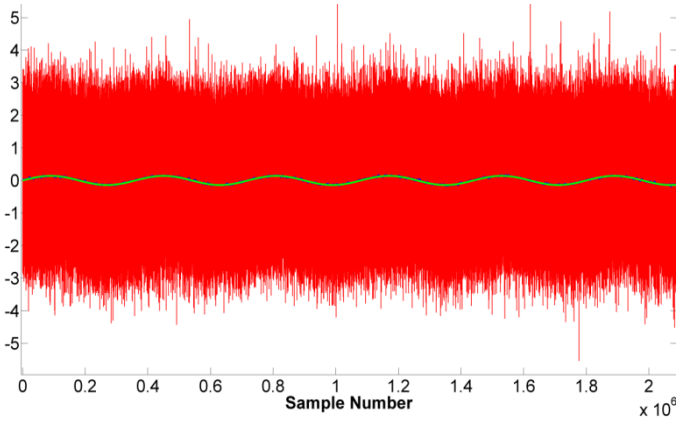
5
4
3
2
1
0
-1
-2
-3
-4
-5
0
0.2
0.4
0.6
0.8
1
1.2
1.4
1.6
1.8
2
Sample Number
x 10^6

i.

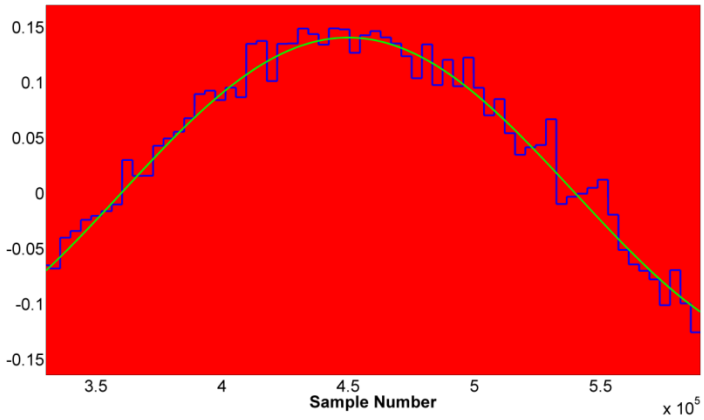
0.15
0.1
0.05
0
-0.05
-0.1
-0.15
3.5
4
4.5
5
5.5
Sample Number
x 10^5

j.

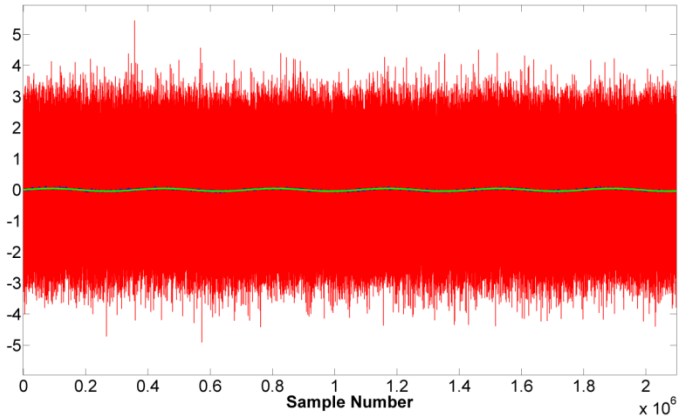
5
4
3
2
1
0
-1
-2
-3
-4
-5
0
0.2
0.4
0.6
0.8
1
1.2
1.4
1.6
1.8
2
Sample Number
x 10^6

k.

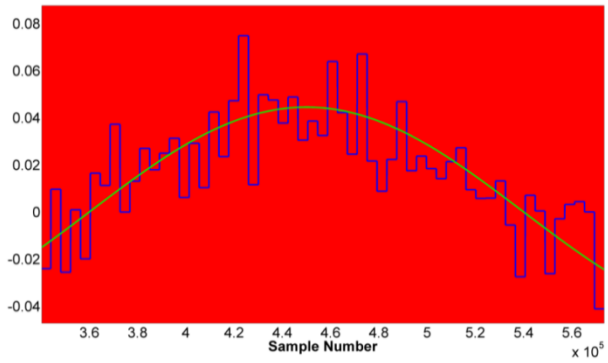

l.

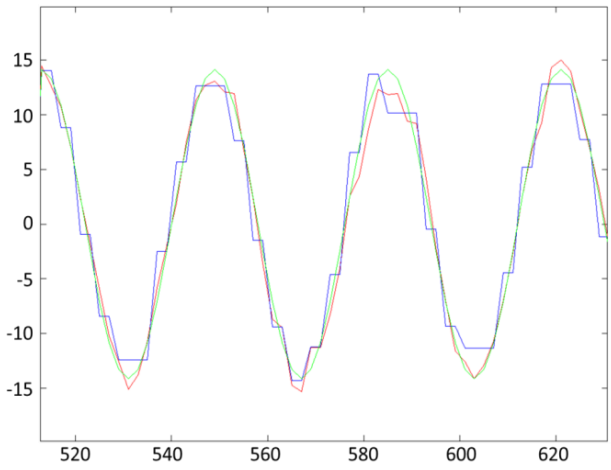

m.

Fig. 4.7 Sample estimation of a sinusoidal RFI with different Interference-to-Noise Ratios. X axis is sample number and Y axis amplitude (arbitrary units $\sigma^2_{noise} = 1, \sigma^2_{RFI} = INR \cdot \sigma^2_{noise}$). The colors are as follows: composite signal is red, modeled interference is blue and original interference is green: a) INR = +20 dB with 36 Kilo Samples (KS) per period, b) Zoom of Fig. 4.7a, c) INR = +10 dB with 36 KS per period, d) Zoom of Fig. 4.7c, e) INR = 0 dB with 36 KS per period, f) Zoom of Fig. 4.7e, g) INR = -10 dB with 36 KS per period, h) Zoom of Fig. 4.7g, i) INR = -20 dB with 36 KS per period, j) Zoom of Fig. 4.7j, k) INR = -30 dB with 36 KS per period, l) Zoom of Fig. 4.7k and m) INR = +20 dB but with only 36 samples per period.

RFI mitigation is calculated for signals presented in Figs. 4.7 and 4.8. For Figs. 4.7 and 4.8 where 36,000 samples per period are used, the attenuation for INR = 20 dB, 0 dB and -30 dB interferences is 35 dB, 20 dB and 7 dB respectively. For Fig. 4.7m, where 36 samples per period are used, the attenuation for INR = 20 dB interferences is 12 dB.

Note that the estimation of weak RFI (e.g. sinusoidal RFI with INR = -30 dB) requires sets of length = 2^{21}, with at least 36,000 samples per signal period for an effective threshold estimation [71].

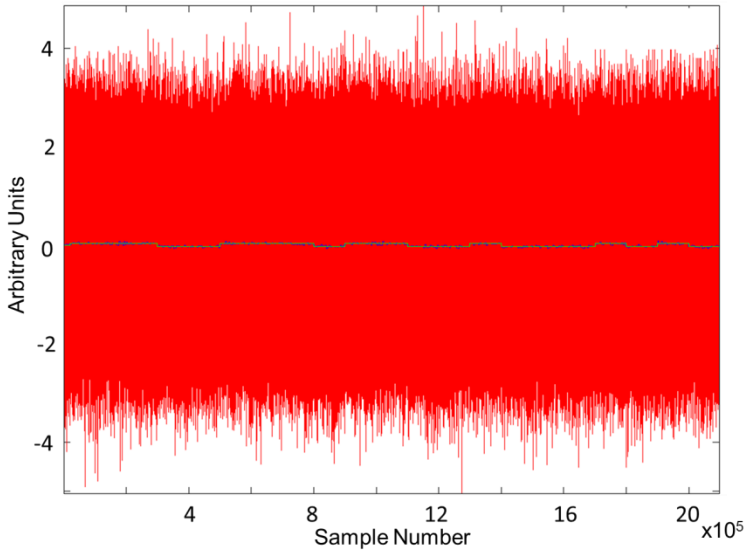

a.

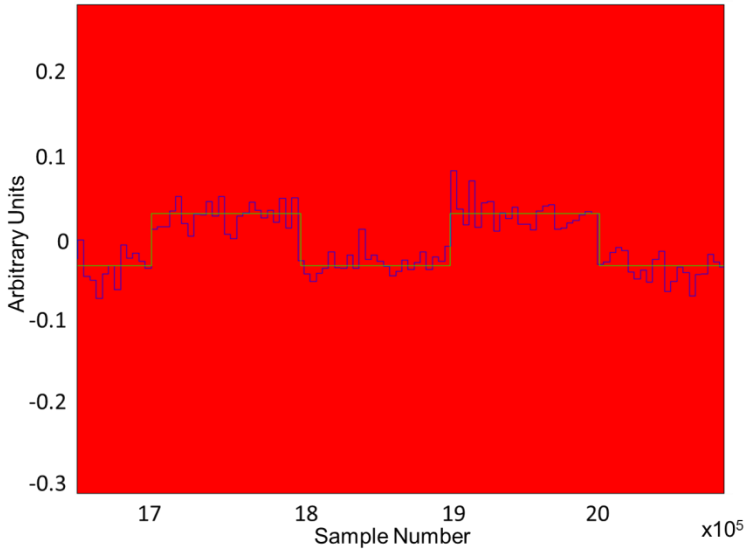

b.

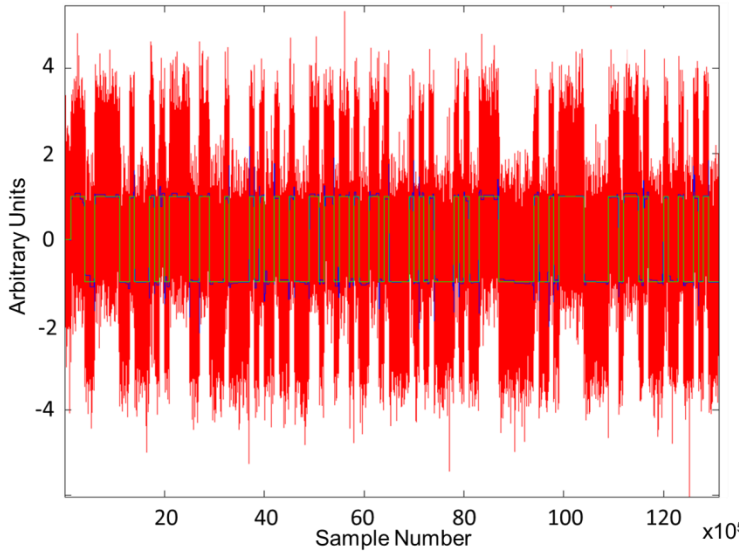

c.

Fig. 4.8 Sample estimation of a PRN RFI with different Interference-to-Noise Ratios with 36,000 per period. X axis is sample number and Y axis amplitude (arbitrary units $\sigma^2_{noise} = 1, \sigma^2_{RFI} = INR \cdot \sigma^2_{noise}$). The colors are as follows: composite signal is red, modelled interference is blue and original interference is green. a) INR = -30 dB b) Zoom of Fig. 4.8a c) INR = 0 dB.

4.5 WAVELET DENOISING FOR RFI REMOVAL

Sinusoidal RFI mitigation comparison between simulated signals and hardware implemented is shown in Figs. 4.9a to 4.9f. Note that the increment of the interference power makes it easier to detect and mitigate, while an increase in the signal frequency difficult the mitigation. Also is noticeable that the results with the hardware implementation are very similar to the theoretical estimations.

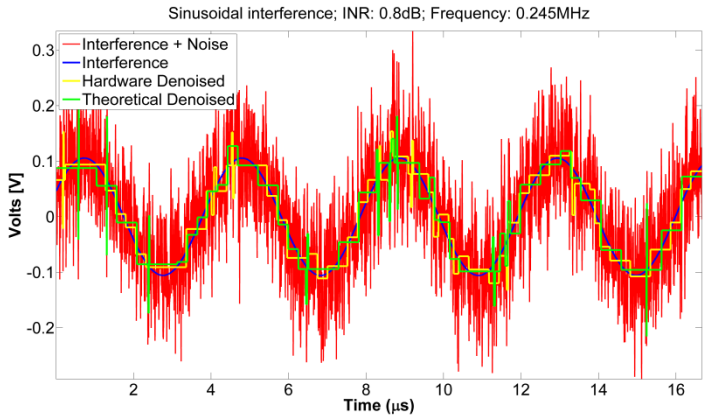
Sinusoidal interference; INR: 0.8dB; Frequency: 0.245MHz
Interference + Noise
Interference
Hardware Denoised
Theoretical Denoised
Volts [V]
Time (μs)

a.

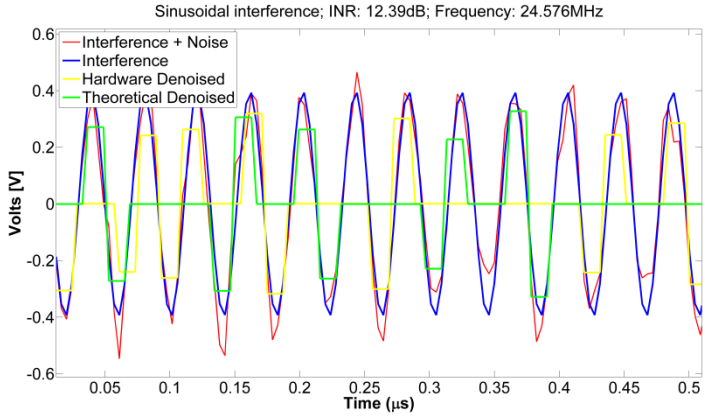
Sinusoidal interference; INR: 12.39dB; Frequency: 24.576MHz
Interference + Noise
Interference
Hardware Denoised
Theoretical Denoised
Volts [V]
Time (μs)

b.

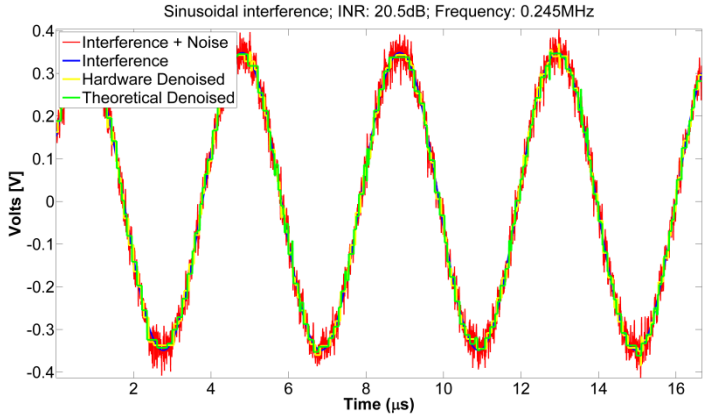
Sinusoidal interference; INR: 20.5dB; Frequency: 0.245MHz
Interference + Noise
Interference
Hardware Denoised
Theoretical Denoised
Volts [V]
Time (μs)

c.

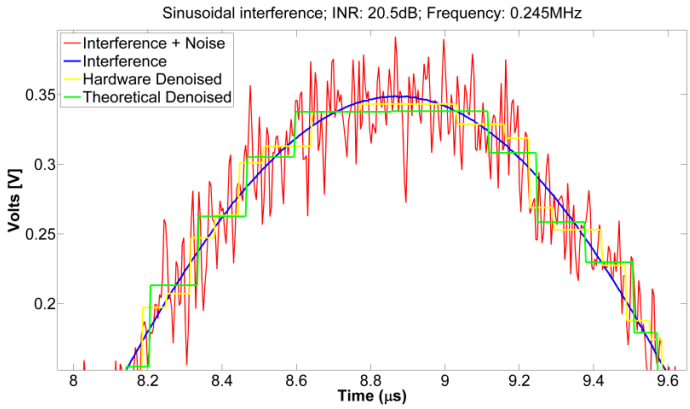

d.

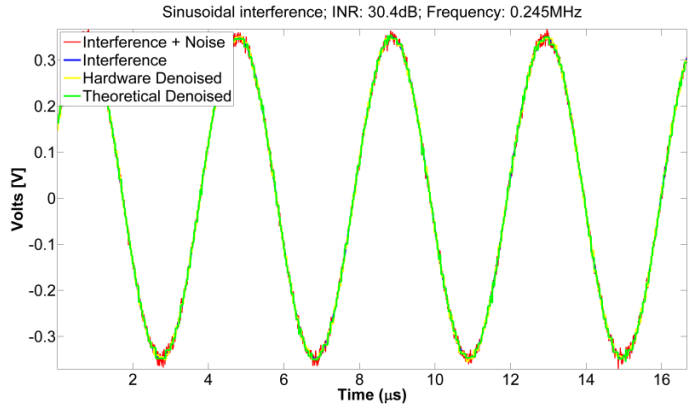

e.

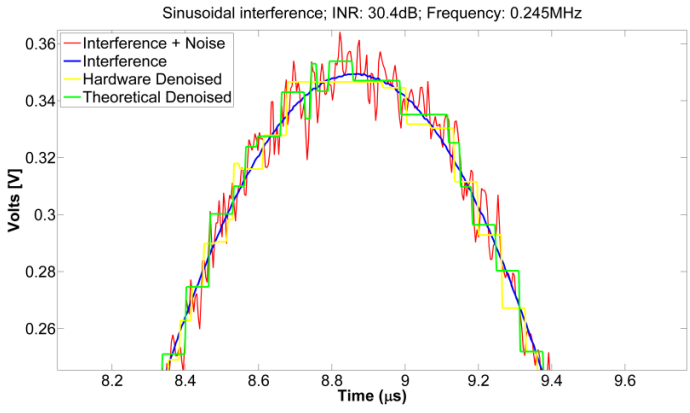

f.

Fig. 4.9 Real data vs. simulation for sinusoidal RFI mitigation using wavelets. Horizontal axis represents time in [μs]. Vertical axis magnitude is Volts. a) INR of 0.8 dB and frequency of 0.245 MHz. b) INR of 12.39 dB and frequency of 24.576 MHz. c) INR of 20.5 dB and frequency of 0.245 MHz. d) Zoom of Fig. 4.9c. e) INR of 30.4 dB and frequency of 0.245 MHz. f) Zoom of Fig. 4.9e.

Figure 4.10 shows that RFIs with larger INRs are easily detected, and mitigated with the wavelet denoising technique. However, it also allows rejecting RFI signals with lower INR, even if their power is below the noise power.

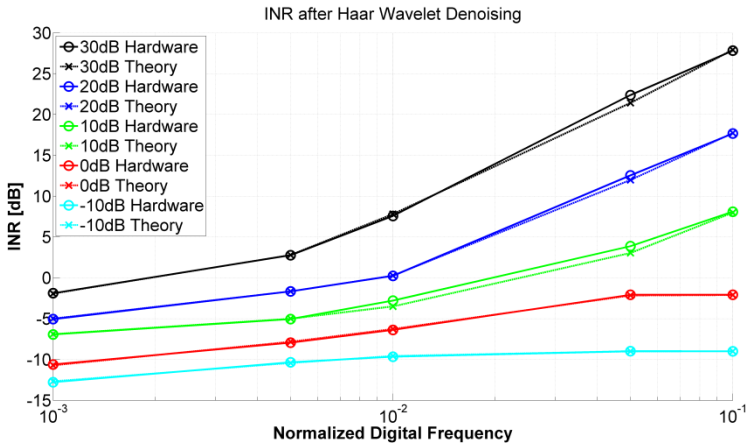

Fig. 4.10 INR after Haar Wavelet denoising for theory signal vs. hardware implemented of sinusoidal RFI mitigation using wavelets.

Sinusoidal Chirp signals are an extension of the sinusoidal case. The difference is that the frequency is changing with time, so when the instantaneous frequency is lower the rejection is better than when the instantaneous frequency is higher, as it can be noticed in Figs. 4.11a to 4.11j.

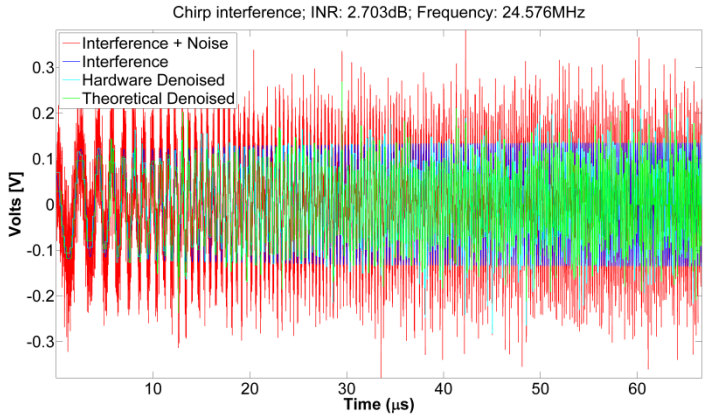

a.

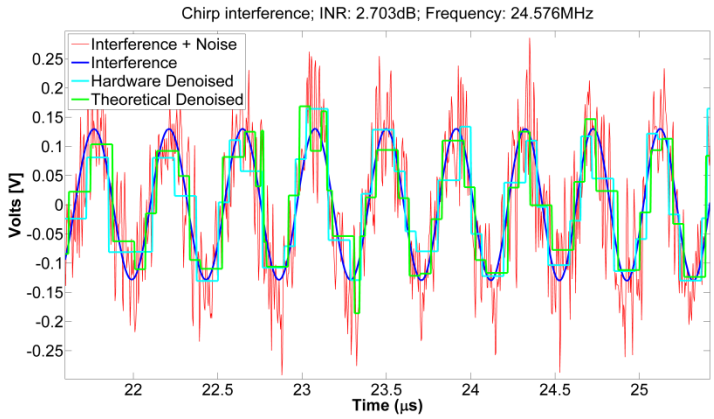
Chirp interference; INR: 2.703dB; Frequency: 24.576MHz
Interference + Noise
Interference
Hardware Denoised
Theoretical Denoised
Volts [V]
Time (μs)

b.

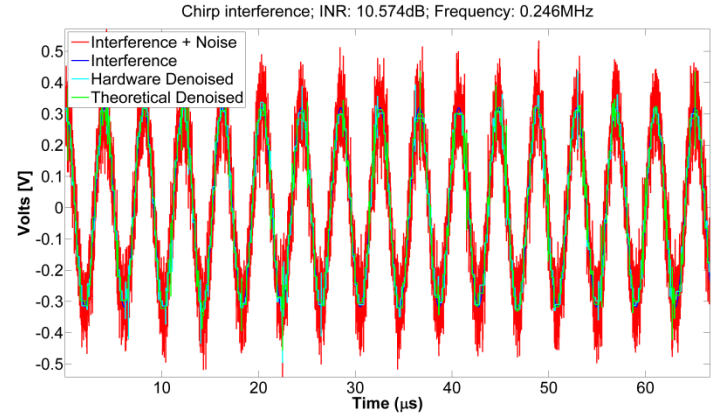
Chirp interference; INR: 10.574dB; Frequency: 0.246MHz
Interference + Noise
Interference
Hardware Denoised
Theoretical Denoised
Volts [V]
Time (μs)

c.

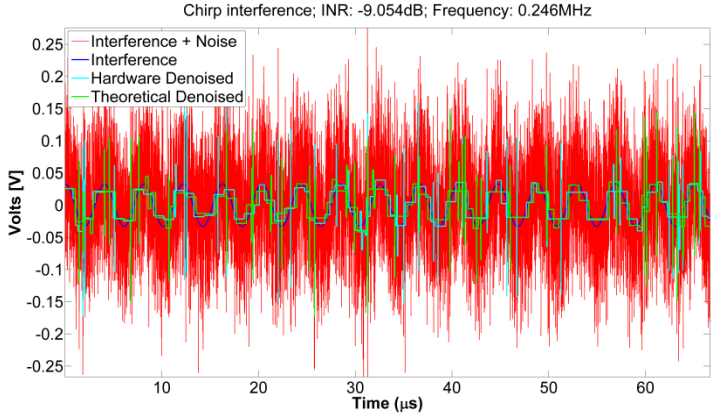
Chirp interference; INR: -9.054dB; Frequency: 0.246MHz
Interference + Noise
Interference
Hardware Denoised
Theoretical Denoised
Volts [V]
Time (μs)

d.

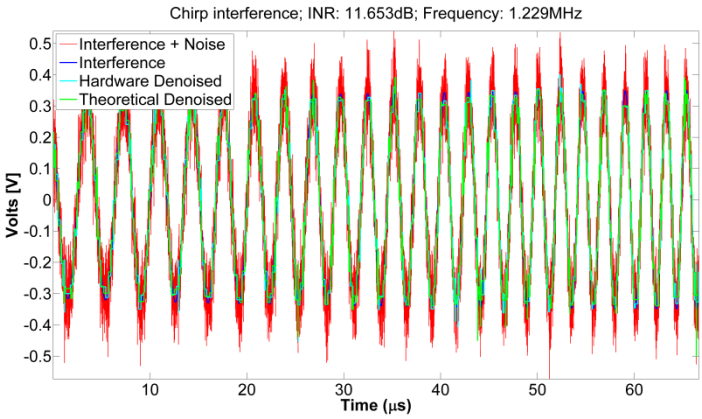
Chirp interference; INR: 11.653dB; Frequency: 1.229MHz
Interference + Noise
Interference
Hardware Denoised
Theoretical Denoised
Volts [V]
Time (μs)

e.

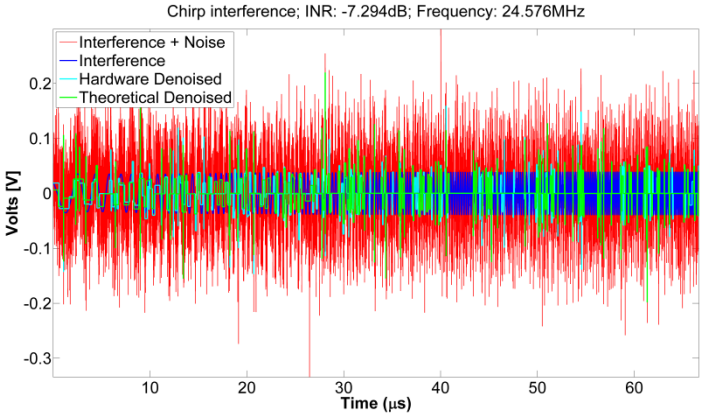
Chirp interference; INR: -7.294dB; Frequency: 24.576MHz
Interference + Noise
Interference
Hardware Denoised
Theoretical Denoised
Volts [V]
Time (μs)

f.

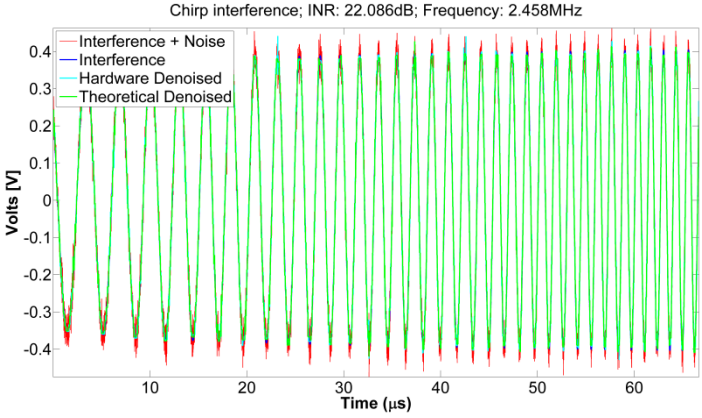
Chirp interference; INR: 22.086dB; Frequency: 2.458MHz
Interference + Noise
Interference
Hardware Denoised
Theoretical Denoised
Volts [V]
Time (μs)

g.

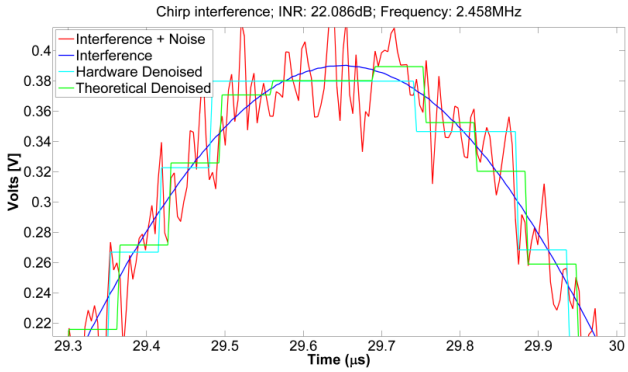

h.

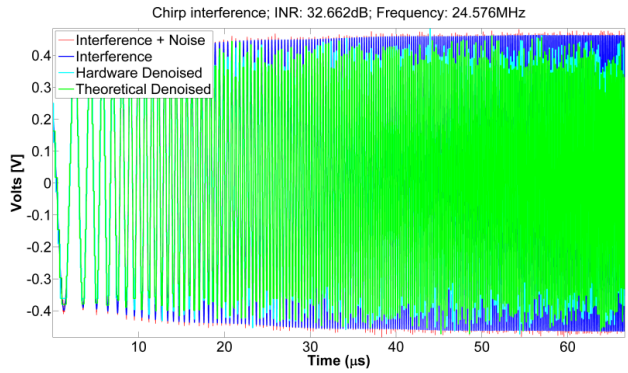

i.

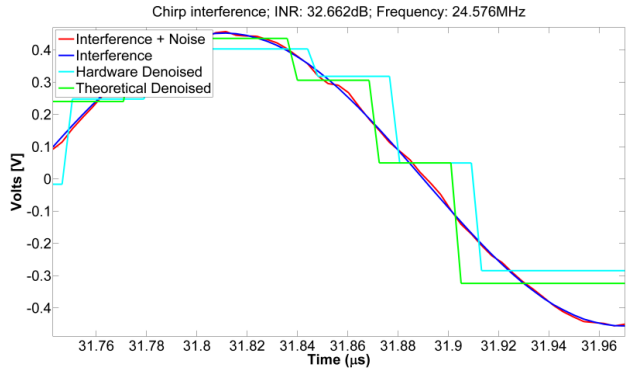

j.

Fig. 4.11 Real data vs. simulation for sinusoidal chirp RFI mitigation using wavelets. On the X axis, time is in microseconds. On the Y axis, signal amplitude is in Volts. a) INR of 2.703 dB and frequency of 24.576 MHz. b) Zoom of Fig. 4.11a. c) INR of 10.574 dB and frequency of 0.246 MHz. d) INR of -9.054 dB and frequency of 0.246 MHz. e) INR of 11.653 dB and frequency of 1.229 MHz. f) INR of 7.294 dB and frequency of 24.576 MHz. g) INR of 22.086 dB and frequency of 2.458 MHz. h) Zoom of Fig. 4.11g. i) INR of 32.662 dB and frequency of 24.576 MHz. j) Zoom of Fig. 4.11i.

Figure 4.12 leads to the same conclusion as Fig. 4.10: RFIs with larger INRs are easily detected, and mitigated with the wavelet denoising technique, but the technique also allows rejecting RFI signals with lower INR, even if their power is below the noise power.

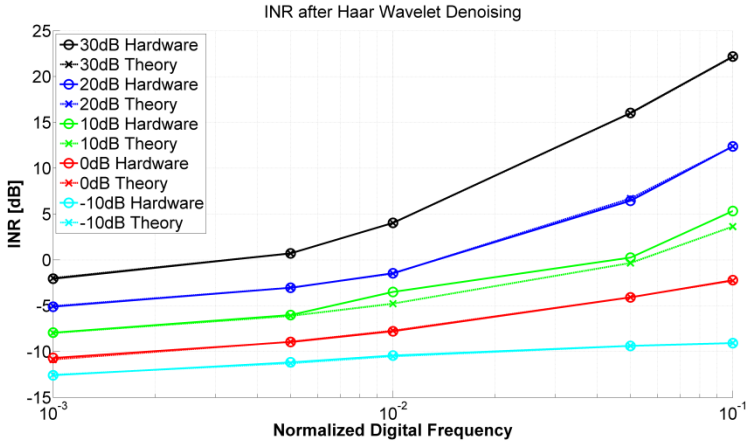

Fig. 4.12 INR after Haar Wavelet denoising for theory signal vs. hardware implemented of sinusoidal chirp RFI mitigation using wavelets.

Figures 4.13a to 4.13i show the experiments with PRN interferences. These types of interferences are more easily mitigated when they have few transitions from one level to another. This is because when it stays in the same level the wavelet adjusts faster than when the signal has many changes. For the interference power and frequency, the same conclusions as sinusoidal and chirps interferences can be applied.

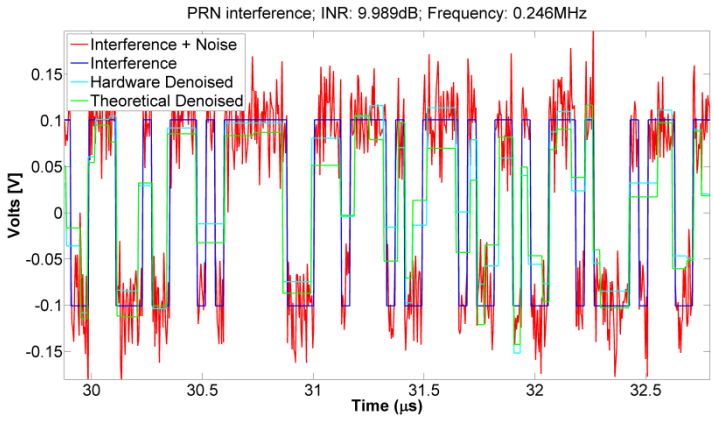

a.

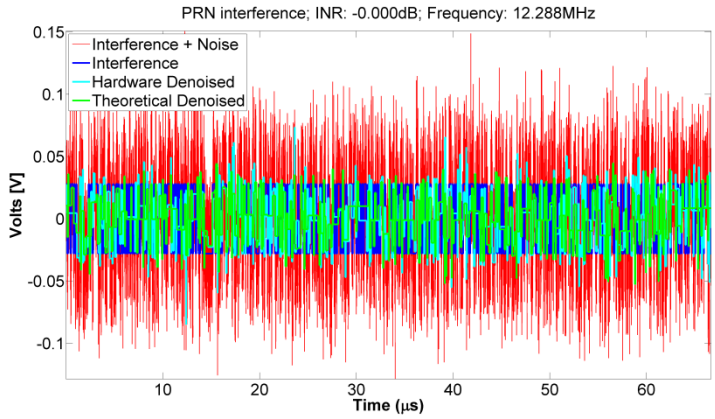
PRN interference; INR: -0.000dB; Frequency: 12.288MHz
Interference + Noise
Interference
Hardware Denoised
Theoretical Denoised
Volts [V]
Time (μs)

b.

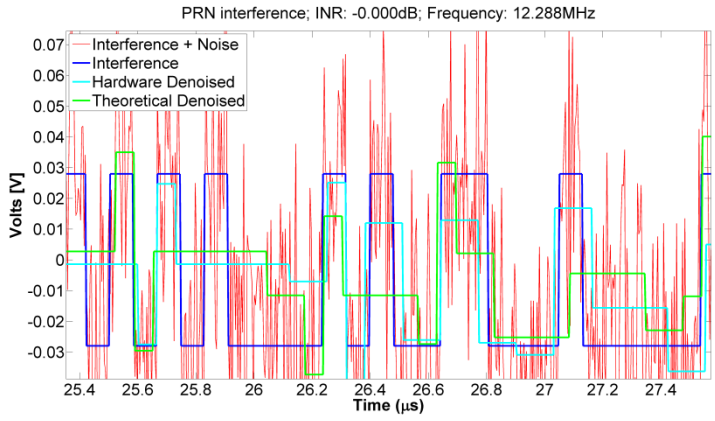
PRN interference; INR: -0.000dB; Frequency: 12.288MHz
Interference + Noise
Interference
Hardware Denoised
Theoretical Denoised
Volts [V]
Time (μs)

c.

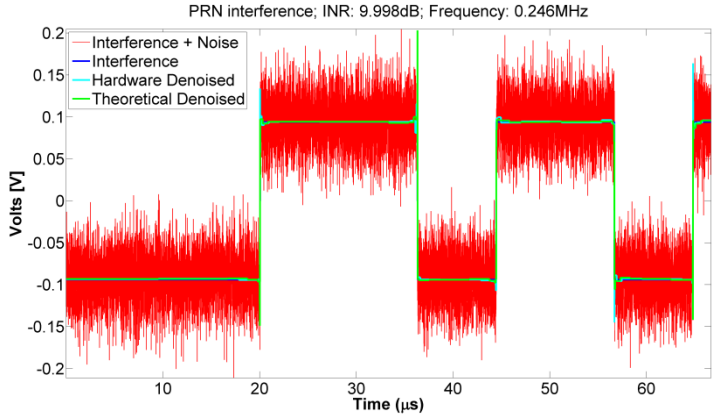
PRN interference; INR: 9.998dB; Frequency: 0.246MHz
Interference + Noise
Interference
Hardware Denoised
Theoretical Denoised
Volts [V]
Time (μs)

d.

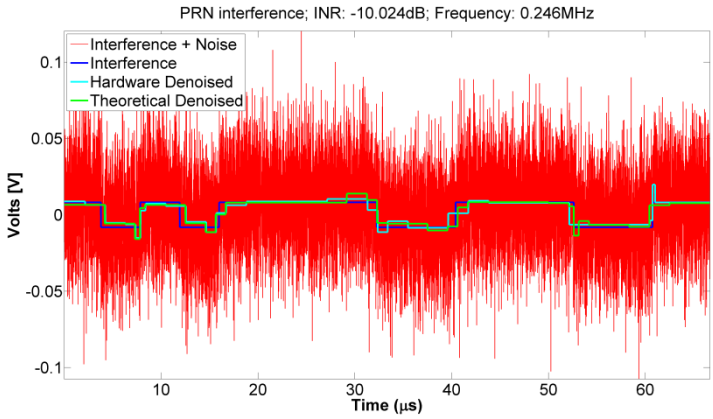
PRN interference; INR: -10.024dB; Frequency: 0.246MHz
Interference + Noise
Interference
Hardware Denoised
Theoretical Denoised
Volts [V]
Time (μs)

e.

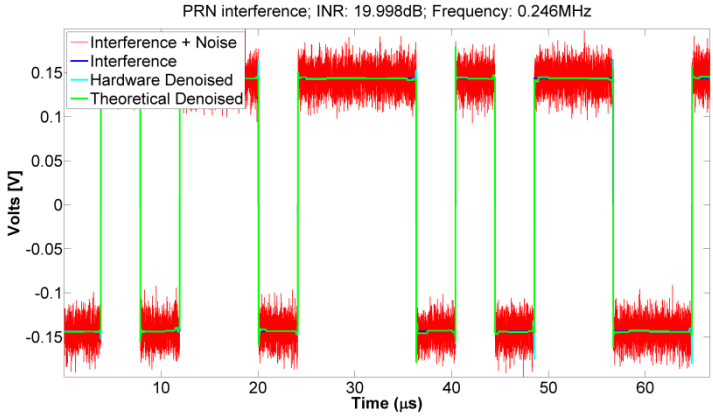
PRN interference; INR: 19.998dB; Frequency: 0.246MHz
Interference + Noise
Interference
Hardware Denoised
Theoretical Denoised
Volts [V]
Time (μs)

f.

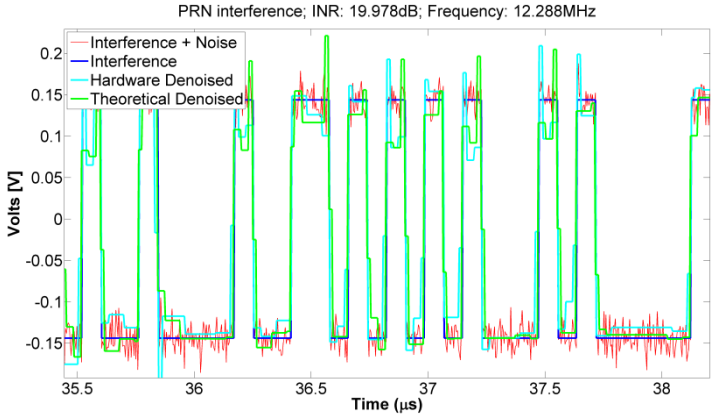
PRN interference; INR: 19.978dB; Frequency: 12.288MHz
Interference + Noise
Interference
Hardware Denoised
Theoretical Denoised
Volts [V]
Time (μs)

g.

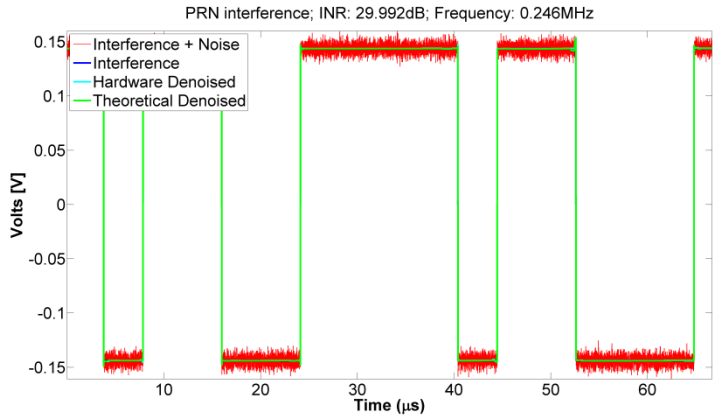

h.

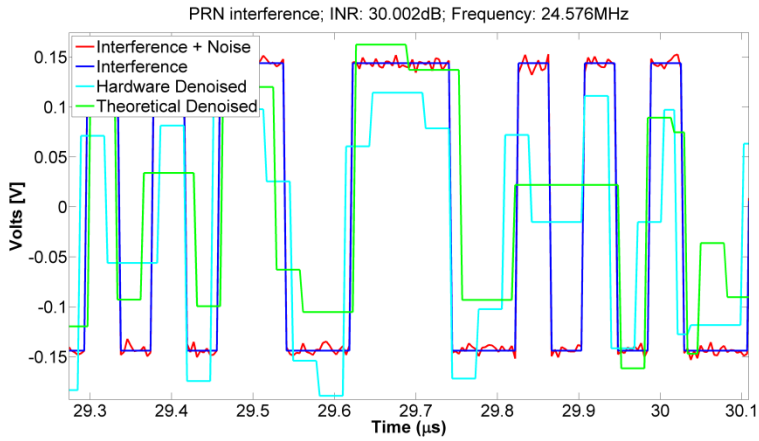

i.

Fig. 4.13 Real data vs. simulation for sinusoidal chirp RFI mitigation using wavelets. On X axis time in microseconds. On Y axis signal magnitude is Volts. a) INR of 9.989 dB and frequency of 0.246 MHz. b) INR of 0 dB and frequency of 12.288 MHz. c) Zoom of Fig. 4.13b. d) INR of 9.998 dB and frequency of 0.246 MHz. e) INR of -10.024 dB and frequency of 0.246 MHz. f) INR of 19.998 dB and frequency of 0.246 MHz. g) INR of 19.978 dB and frequency of 12.288 MHz. h) INR of 29.992 dB and frequency of 0.246 MHz. i) INR of 30.002 dB and frequency of 24.576 MHz.

4.6 CONCLUSIONS

The wavelet denoising technique performs better as the RFI INR or the number of samples increases until the system saturation point is reached. On the other hand, if a weak RFI wants to be mitigated, an oversampling is needed.

When estimating weak RFI, e.g. a sinusoidal signal with INR = -30 dB., an attenuation of up to 9 dB could be achieved. It requires at least 36,000 samples per signal period

(an approximate normalized digital frequency of $2.7x10^{-5}$ as in Fig. 4.6a) for effective threshold estimation [71]. This is not feasible for nowadays single FPGA's block RAM cells because it requires around 200 Megabits (Mb) memory [75] and in 2014 the most powerful Virtex UltraScale FPGA has 115 Mbits, at most. To overcome this problem, a FPGA board with a multibank DDR memory is used. The number of banks must be at least the pipeline levels multiplied by the read/write cycles of the memory. This improvement to the system was proposed in [75], and it allows the system to continuously acquire, process, and write the total amount of data needed to mitigate sinusoidal RFI with INR of ~30dB.

Another limitation for weak RFI mitigation (INR ~ -30dB) is the data acquisition hardware (e.g. for 8 dB attenuation, 1250 samples per signal period are needed, so a 250 MSPS ADC can process signals up to 200 KHz).

On the other hand, strong RFIs can be easily mitigated with this method (e.g. with only 100 samples per signal period, a 250 MSPS ADC can mitigate up to 19 dB interferences up to 2.5 MHz).

This RFI-mitigation system has been implemented in a Kintex 7 FPGA with an estimated latency between the sample and its interference mitigated of approximately 534 μs.

For chirp interferences, the same behaviour as for sinusoidal interferences happens. The RFI is more easily detected when the chirp instantaneous frequency is low, and it becomes more difficult when the frequency increases.

Chapter 5

ANTI-JAMMING HARDWARE FOR GNSS SIGNAL

In Chapters 2 and 3 the increase of the GNSS RFIs and their harmful effects in navigation has been presented. The most common sources of RFI are the so-called PPDs (jammers), so a way to deal with them is a required [46, 75-78]. During this PhD thesis, in collaboration with a Master thesis [46], RFI detection and mitigation algorithms for communications and navigation have been implemented in hardware. The results are presented in this chapter.

5.1 RFI DETECTION AND MITIGATION

The RFI detection criterion is based in the Neyman-Pearson hypothesis testing where a threshold value is defined to discriminate between RFI-free and RFI-contaminated data. Also a trade-off between the probability to correctly detect the RFI (probability of detection), and the probability to eliminate clean signal wrongly detected as RFI (probability of false alarm), must be taken into account [79, 80].

To mitigate the RFI induced by jammers, such as the one explained in Chapter 2, the first approach is in the Time-frequency domain, as explained in Chapter 1. Frequency Domain is obtained by applying the Short-Time Fourier Transform (STFT) to the data in time domain, and it is much easier implementation than Wavelet transform [81, 82]. The Fast Fourier Transform with Overlap-Add reconstruction [82-84] is implemented in the FPGA.

Normality tests have also been used to distinguish RFI free and contaminated samples [61, 84, 85].

5.2 GPS SIGNAL AND THERMAL NOISE APPROXIMATION

The implemented hardware is designed to work with the Coarse/Acquisition (C/A) code instead of the Precision (P) code, because most of the GPS receivers work with it. The main reason that jamming is an issue with any GPS receiver is that the signals coming from the satellites are very weak [76], from -120 dBm to -130 dBm outdoors, below the thermal noise floor, and indoors around 20 to 30 dB less. At room temperature, the thermal noise power within an approximate of 2 MHz bandwidth is about -110 dBm, already 10 to 20 dB higher than GPS signals. With such a weak signal, other signals in the same GPS frequency band can easily interfere it, and they do not have to be very strong in order to override the satellite signals.

Despite the weak signals received, GPS receivers can obtain the position information because the spread-spectrum signal properties of the GPS signals allow for a ~30 dB compression gain. Thus, considering the central limit theorem for the sum of two independent random variables and the difference of power between the GPS signal and the thermal noise, their sum can be approximated by the thermal noise itself. One way to understand this is to consider that the GPS signal is "masked" under the thermal

noise floor. Thereby, the received GPS signal can be considered to have constant power spectral density over its signal bandwidth and to be a Normal random variable with odd central moments equal to zero.

5.3 HARDWARE SET-UP

The hardware set-up can be seen in Fig. 5.1. The GPS signal is received through an active antenna with ~30 dB gain and powered at 5 V. Previously to the application of the RFI detection and mitigation algorithm, the received signal must be amplified, filtered, and down-converted from the L1 band to an Intermediate Frequency (IF), where it is sampled and digitized. The selected GPS filter is the SAW filter TA1575IG that has a 2.4 MHz bandwidth, center frequency at 1575.42 MHz and 2 dB insertion loss. The function of this filter is to reject thermal noise and RFI out of the GPS band. The down-conversion is performed with a Minicircuits mixer model ZFM-150-S+ connected to the signal generator R&S-SMR40 used as Local Oscillator (LO) set at a frequency of 1558.78 MHz, so, it leads to an Intermediate Frequency (IF) of 16.64 MHz. After that, the GPS signal is digitalized with the Analog-to-Digital Converter (ADC) ADS4249 at a sample rate of 245.76 MSPS, and a maximum input voltage of 2 Vpp (10 dBm). The conversion is performed with 14 bits, allowing a minimum signal power about -84 dBm (6.02 dB/bit). For this reason, the microwave amplifiers placed before the ADC have a large gain, to have a GPS signal power about -70 dBm. The complete hardware setup picture is shown in Fig. 5.1b with each component location and description to link it easily to the block diagram.

The RFI detection and mitigation algorithm is implemented in a Xilinx Kintex-7 XC7K325T-2FFG900C FPGA. A midrange FPGA is powerful enough to harbour several of the algorithms described in Chapter 1. After the GPS signal processing, the digital RFI cleaned signal is converted to analog, and then up-converted to the L1 frequency band.

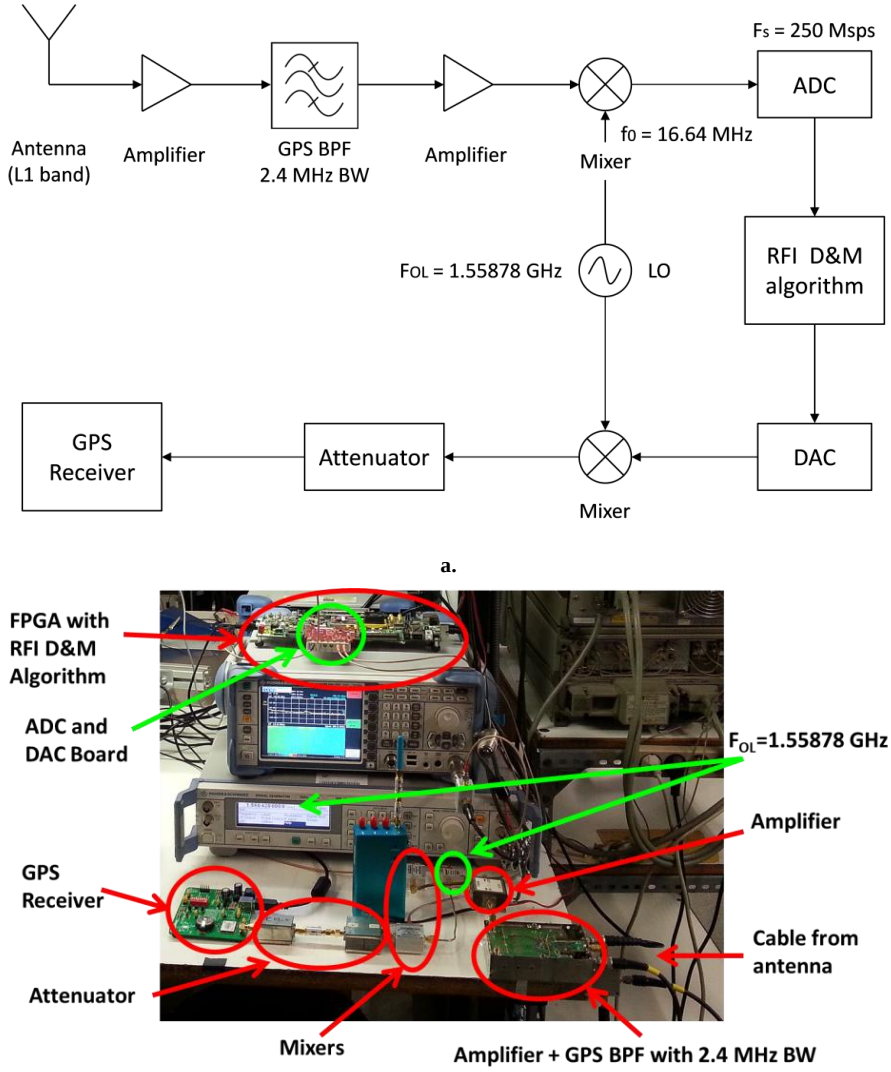

Fig. 5.1 GPS Anti-jamming System. a) Block Diagram. b) Corresponding hardware setup

This up- and down-conversion of the GPS signal carrier allows processing the signal digitally at a moderate sampling rate and makes the anti-jamming hardware transparent to any GPS receiver. The Digital-to-Analog Converter (DAC) is the DAC3283 with 16 bit conversion, an internal sampling clock of 491.52 MHz and a maximum output voltage of 1 Vpp. After that, the up-conversion is analogous to the down-conversion: it is performed with a ZFM-150-S+ mixer, and the same signal from

the R&S-SMR40 generator is used as Local Oscillator (LO). Finally, the RFI-cleaned signal is attenuated and connected to the commercial GPS receiver u-Blox LEA-5S-0-004.

5.4 RFI DETECTION AND MITIGATION ALGORITHM

As it can be seen in Fig. 5.2, the RFI detection and mitigation algorithm has three stages: the interpolator and decimator, the time-frequency decomposition, and the statistical filtering. The first two have two parts: the analysis that prepares the signal for the next stage, and the synthesis that reconditions the transformation of the analysis part. The first step of the algorithm consists of a digital Band-Pass Filter (BPF) that performs the decimation in the analysis part, and the interpolation in the synthesis part. This filter has the mission to remove the noise out of the GPS band that has been generated in the previous stages of the analog hardware and, thus, prevent aliasing when down-sampled. Moreover, it contributes to remove the remaining thermal noise, and high power RFI.

The BPF is a 2048 coefficients Finite Impulse Response (FIR) with a Dolph-Chebyshev window with parameter $\alpha = 3$. The filter has a central frequency of f_c = 16.64 MHz, and a bandwidth of B = 2.38 MHz. Thanks to the large number of coefficients and the nature of the Dolph-Chebyshev window, it is quite sharp in frequency domain (see Figure 5.3), and since it is a FIR filter instead of Infinite Impulse Response (IIR) filter it exhibits better phase properties [82].

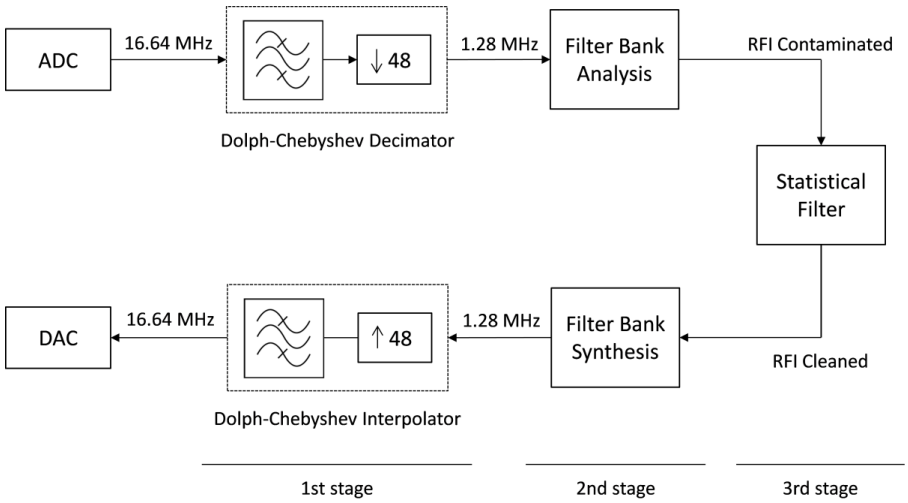

Fig. 5.2 Block diagram of the Anti-jamming detection and mitigation algorithm

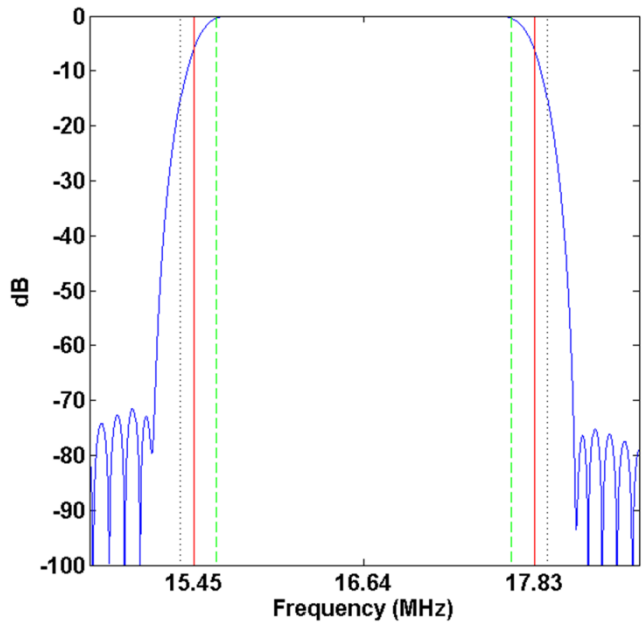

Fig. 5.3 FIR BPF response with a Dolph-Chebyshev window with parameter $\alpha = 3$

The down-sampling is performed with the undersampling method described in [83] with a decimation (and interpolation) ratio of $M = 48$, and using the 6^{th} alias image (the LO frequency was chosen properly for this purpose), as it can be seen in Fig. 5.4.

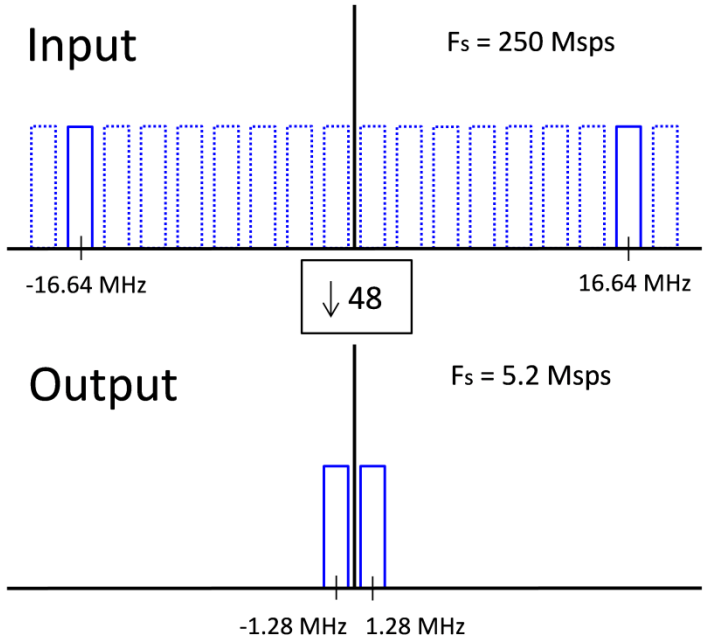

Fig. 5.4 Undersampling method with a decimation ratio of M=48

Then, the new Nyquist frequency f_n and the central frequency of the GPS band is f_0 are:

$$f_n = \frac{f_s}{2M} = \frac{245.76\ MHz}{2 \cdot 48} = 2.56\ MHz, \tag{5.1}$$

and

$$f_0 = \frac{f'_0}{2N_{alias}+1} = \frac{16.64\ MHz}{2 \cdot 6+1} = 1.28\ MHz. \tag{5.2}$$

The second stage is the time-frequency decomposition. The Filter Bank Sum technique was selected because it has an inverse function that allows the complete signal reconstitution, and it also needs less hardware resources than others when a few frequency channels are implemented. In this case, the number of filters in the bank is N = 5 because of the hardware constraints (leave FPGA area to implement other mitigation algorithms). These filters are designed in such a way that the sum of the Fourier transform of each of them gives a constant or almost a constant (see Figure 5.5), thus, the inverse of the filter bank analysis part is just the sum of the outputs of all the five channels. The first filter is low-pass FIR filter with 17-tap Hann window which has very good properties to implement the sum technique. The rest of the filters are equidistant translations in frequency of the first filter, which reminds to the

Discrete Fourier Transform, which are grouped in such a way so as to obtain five real filters as follows:

$$h_k[n] = v[n] \cdot e^{-i2\pi\frac{kn}{M}}, L = 2M + 1 \quad (5.3)$$

$$h_i^{FB}[n] = \frac{h_i[n]+h_{M-i}[n]}{2}, i = 0, \dots, 4 \quad (5.4)$$

The Filter Bank Sum condition is given by L = 2M + 1 for a Hann window. This it is the minimum value of L for which the condition is satisfied. With M = 8 translations in frequency, and eventually N = 5 filters in the bank, these filters have L = 17 coefficients. As it is shown in Fig. 5.5, the sum of the filters is almost a constant, and the maximum ripple is approximately ΔH = 0.5 dB which is acceptable for most applications.

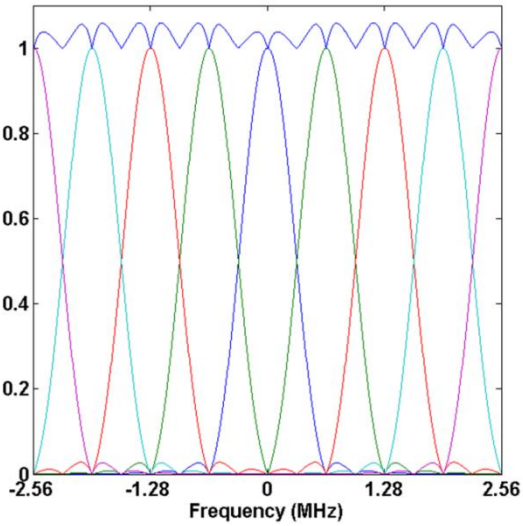

Fig. 5.5 Frequency response of the Filter Bank composed by eight Hann window filters grouped in five real filters. Filter Bank Sum condition is satisfied with a small ripple (blue signal on top).

Finally, the third stage applies a statistical filter to each of the channels generated previously, as shown in Fig. 5.6. First, a normality test is applied to a set of samples of the incoming data, in particular, the Kurtosis test. If the test determines that these samples behave to a Normal random variable (and then to the GPS signal) they are saved to the next step, otherwise, they are discarded. After that, a threshold value is calculated from the saved samples. This threshold is calculated as [85]:

$$th[n] = 3 \cdot \hat{\sigma} = 3 \cdot 1.4826 \cdot MAD(s_N[n]) = 4.4478 \cdot \tilde{s}_N[n] \quad (5.5)$$

where $\hat{\sigma}$ is a robust estimator of the standard deviation of a normal random variable [85], MAD is the Median Absolute Deviation, and $\tilde{s}_N$ is the statistical median of the previous saved samples. The calculated threshold value is compared to every sample of the incoming data and, if the sample is larger, it is considered to be a RFI, and then the output is set to zero. Otherwise, the value of the incoming sample is placed at the output of the statistical filter.

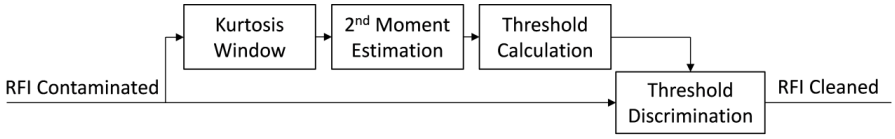

Fig. 5.6 Statistical Filter Block Diagram

5.5 FPGA ANTI-JAMMER PERFORMANCE

The RFI detection and mitigation algorithm has been tested with the signal of a real jammer [46]. This jammer signal generator creates a chirp signal as the following:

$$i(t) = \cos(2\pi(f_0 + f(t)) \cdot t + \varphi_0) \tag{5.6}$$

where φ_0 is arbitrary, f_0 = 1.57542 GHz the GPS carrier frequency and f(t) a sawtooth function with f_{min}(t) = -7.5 MHz, f_{max}(t) = 7.5 MHz and period T = 9 μs. When this signal interferes the GPS signal and the implemented algorithm is not working, the GPS receiver is unable to get the position data, as illustrated in Fig. 5.9 from the Section 5.6.

However, when the anti-jamming hardware is connected between the antenna and the receiver, GPS position can be retrieved (Fig. 5.11 from Section 5.6). First, the analog and the Dolph-Chebyshev digital BPF remove the part of the chirp signal that is out of the GPS band. Then, the continuous interference becomes a pulsed one, so during some periods of time the GPS signal is actually RFI-free.

After that, the GPS band is split into five sub-bands by the Bank Filter. Therefore, the chirp RFI is also split and spread over the five sub-bands. At some instant, the RFI is at one or two of the bands, but the rest of them are RFI-free and, because the chirp performs a frequency sweep, this condition is changing every sample with the period

of the RFI signal. Then, each sub-band is processed by a statistical filter which cleans the signal when it is contaminated by the RFI, and otherwise lets it pass through.

Figure 5.7 shows the performance of such filter. When the signal is not contaminated (jammer signal generator is turned off), the input and output of the filter are practically the same, and the normality test is successful (Kurtosis value is 3 plus an experimentally defined tolerance of ±0.5 needed because GNSS signals are actually not Gaussian and is established by comparing RFI-free and RFI-contaminated signals). Nevertheless, when the RFI appears, the normality test fails, and the threshold remains with a constant value.

Then, when the sample value is lower than the threshold, the output of the statistical filter is equal to the input, and so, it is RFI-free. Otherwise, the output signal is set to zero.

Finally, the output signals coming from the five statistical filters are added together in order to undo the Filter Bank transformation. After that, the rest of the hardware restores the processed GPS signal to its original carrier frequency through the stages stated in Section 5.3.

The anti-jamming hardware has been tested for several Signal-to-Interference Ratios (SIR), by changing the transmitted power. Results show that the RFI detection and mitigation algorithm is able to reject SIRs up to -50 dB.

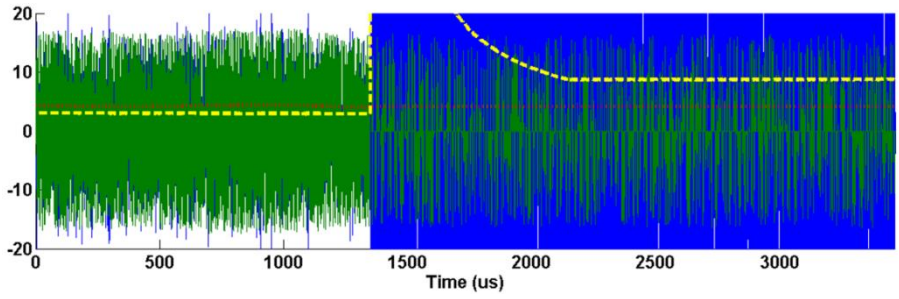

a.

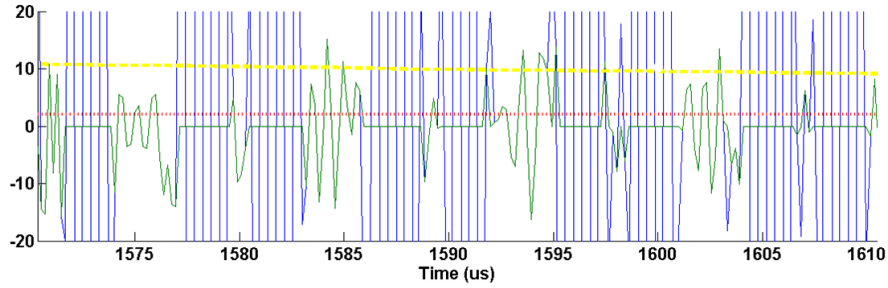

b.

Fig. 5.7 a) Input (blue) and output (green) signal of the statistical filter placed at the third filter of Bank Filter Sum with the evolution of the Kurtosis value (yellow dashed) and the value of the estimated standard deviation (red dotted). b) Zoom picture where it can be appreciated that the RFI is removed in the output signal.

5.6 TESTS

After showing the performance results, the different scenarios are shown here. There are four working combinations as shown in Figs. 5.8 to 5.11:

- Jammer off with Anti-jammer off
- Jammer on with Anti-jammer off
- Jammer off with Anti-jammer on
- Jammer on with Anti-jammer on

The normal GPS work is shown in Fig. 5.8 where the jammer and the anti-jammer are turned off, so the system can acquired a position from the satellites. Notice the signals in the oscilloscope and the spectrum analyser because turning on the jammer modifies them. In this mode the input signal is thermal noise plus the GPS signal that is below this level. In the PC monitor, the small blue bars are the GPS satellites received signal, in the other modes of operation a zoom will be presented to analyse it in detail.

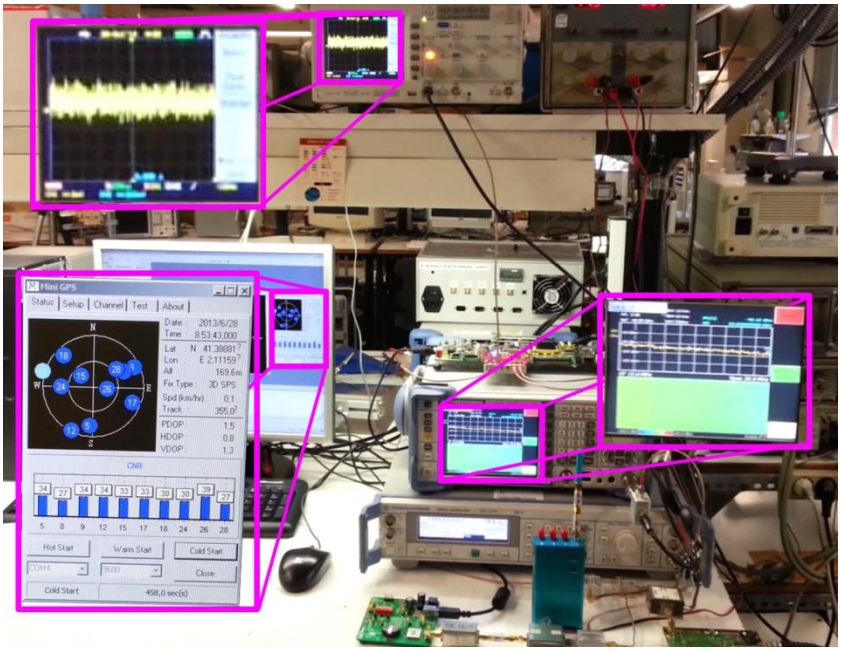

Fig. 5.8 Both jammer and anti-jammer are turn off. In the upper-left caption a zoom of the oscilloscope screen. In the down-left caption is a capture of the GPS tracking software. In the right caption is a zoom of the spectrum analyser screen.

In Fig. 5.9 the big problem is shown: no position can be determined because of the large interference signals inhibits the GPS system. Notice the large signal in the oscilloscope and the increment of noise in the spectrum analyser (for more detail view Chapter 2, where a large number of jammers have been analysed).

In Fig. 5.10 the system is working without any external interference, showing a clean signal in the oscilloscope, and the same noise level in the spectrum analyser. Figure 5.10 shows that the system lets the GPS with a fixed position.

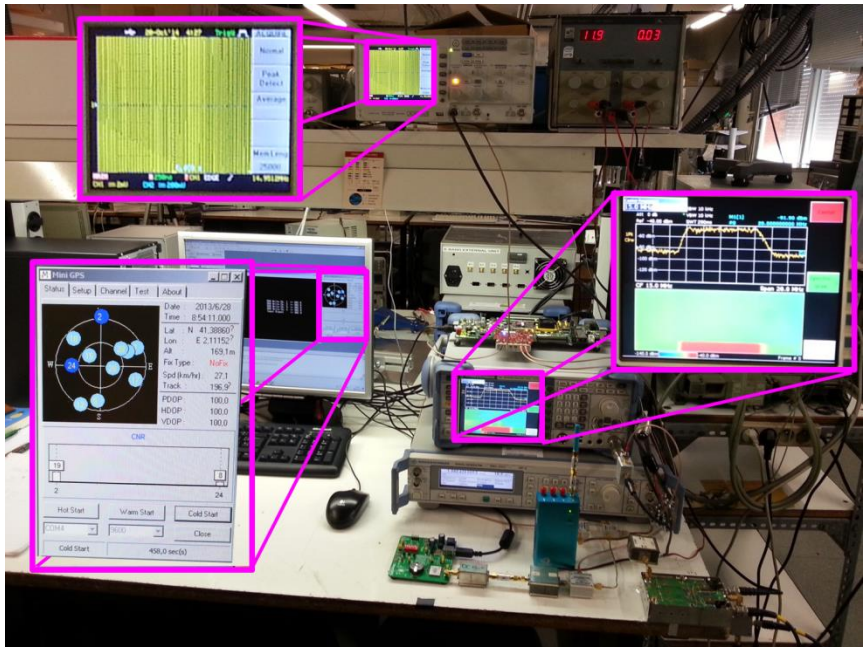

Fig. 5.9 Jammer is turned on while anti-jammer is turned off. In the upper-left caption a zoom of the oscilloscope screen. In the down-left caption is a capture of the GPS tracking software. In the right caption is a zoom of the spectrum analyser screen.

The powerful anti-jamming system capabilities are shown in Fig. 5.11 where the GPS position stills fixed even with the jammer turned on as noticed by its LED light, the spectrum analyser shows an increment in the noise level at that band and the oscilloscope shows a little disturbance in the signal.

Although the recovered signal is not the same as RFI-free, it still provides a Position, Navigation and Timing (PNT) solution, mitigating the effects of the jammer.

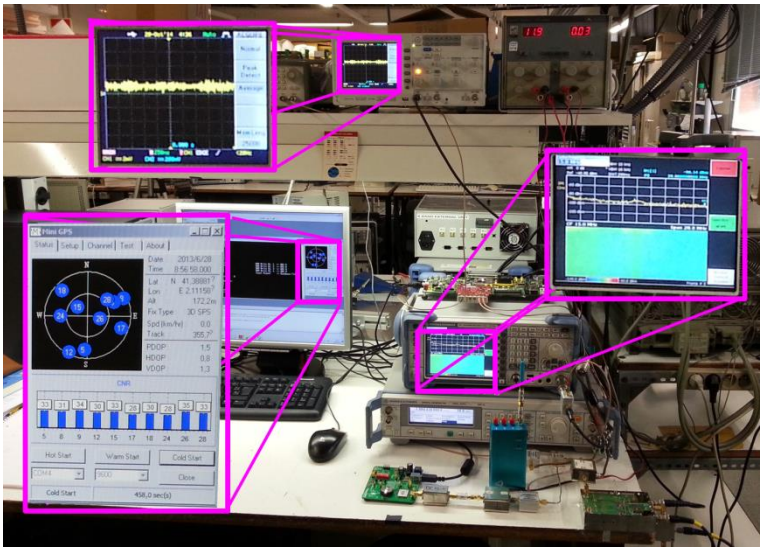

Fig. 5.10 Jammer is turned off while the anti-jamming system is turned on. Measurement of anti-jamming system with Spectrum Analyser, Oscilloscope and GPS tracking software.

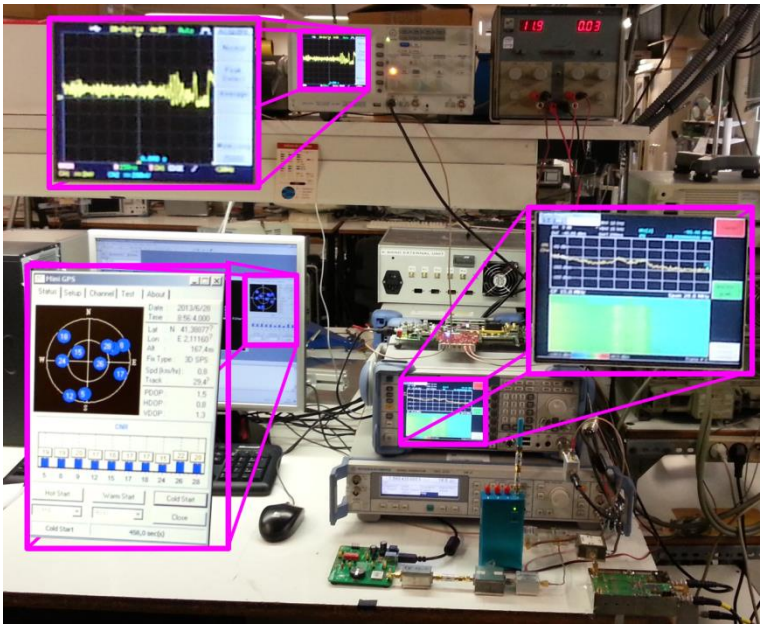

Fig. 5.11 Both jammer and anti-jammer are turned on. Measurement of anti-jamming system with Spectrum Analyser, Oscilloscope and GPS tracking software.

5.7 CONCLUSIONS

A system has been designed and implemented to mitigate the RFI problem of the GNSS systems. It uses a combination of the methods explained in the Chapter 1, mitigating RFIs with Interference to Signal Ratios (ISR) less or equal than 50 dB, for the GPS case that is below noise level. The tests have demonstrated that the system mitigates the effects of real jammer interference, allowing the GPS system to continue providing a PNT solution.

The device utilization summary of the Kintex 7 FPGA is shown in Table 5.1. It is noticeable that the percent of the device used is very low, with the exception of the Flip Flops (FF) at 100%, the Block RAM at 46% and the Global Clock Control Buffers (BUFGCTRLs) at 37%. This means that there is space remaining to implement more sophisticated algorithms in the future to improve RFI mitigation performance in the same system.

Table 5.1 Estimated Values of the Device Utilization Summary

Logic Utilization	Used	Available	Utilization
Number of Slice Registers	33125	407600	8%
Number of Slice LUTs	37597	203800	8%
Number of LUT-FF pairs used	44907	44907	100%
Number of bonded IOBs	205	500	29%
Number of Block RAM/FIFO	208	445	46%
Number of BUFG/BUFGCTRLs	9	32	37%
Number of DSP48E1s	63	840	7%

Chapter 6

CONCLUSIONS AND FUTURE RESEARCH LINES

The present Ph.D. dissertation is a contribution to the RFI detection and mitigation in Earth Observation. It continues the research started at UPC by Dr. Tarongí [80].
Different types of surveys have been performed to test the detection algorithms with real RFI data and GNSS jammers or personal privacy devices. As an innovation, real-time hardware implementation of some detection and mitigation algorithms has been performed.

6.1 CONCLUSIONS AND SUMMARY

RFI has become a severe problem to sensitive measuring devices. Their sources are increasing because most of them are originated by are human-made electrical devices. Several techniques for detecting and mitigating RFI have been proposed, but the optimal way is a combination depending on the interference type.

- Different jammers have been characterized to study their properties and effects in other systems. From the study of the data acquired, the most common signal of jammers appears to be a chirp. Sparks, a very common and unintentional source of RFI, are originated by spark plugs in motor vehicles, DC motors, high voltage installations, etc. They produce large bandwidth noise that can extend up to 3 GHz.
- Results of the time and frequency-domain surveys carried out with the MERITXELL radiometer demonstrate that the lower bands are more contaminated than the higher ones due to the frequency of operation of the wide variety of electronic devices. The higher ones seem to be cleaner, not only because the higher frequency, but also because of the much wider bandwidth, so a narrow band interference occupies a much smaller fraction of the band.
- Real-time RFI detection and mitigation techniques have been implemented in hardware. The wavelet denoising technique performs better as the RFI INR or the number of samples increases until the system overload point is reached. If a weak RFI wants to be mitigated, an oversampling is required. On the other hand, strong RFIs can be easily mitigated with this method. The designed and implemented system to mitigate the RFI problem of the GNSS has a remarkable influence. The tests have demonstrated that the system mitigates the effects of real jammer interference, allowing the GPS system to continue providing a PNT solution.

6.2 FUTURE RESEARCH LINES

- Synthetic aperture radiometers can be used in the future for enhanced RFI geolocalization due to their better angular resolution for the same array size.
- The novel wavelet denoise in real-time system demonstrate that interferences can be modelled without any a-priori knowledge of it. However, its use with large bandwidths (hundreds of MHz), requires subbanding with multiple FPGAs to process the incoming data as needed. In the coming years, the

research in new transistors (e.g. graphene, ...) will likely increment the processing capabilities, thus reducing the current system limitations.

- The system explained in Chapter 5 can be miniaturized to make it ready to market.

APPENDIX

A.1 ANTENNA

Navigation signals of the Global Positioning System (GPS) can be used as signals of opportunity for remote sensing of the atmosphere or the Earth's surface. A novel technique to be tested by a secondary payload aboard the PAZ mission, uses the signal depolarization when it passes through a scattering medium, such as a rain cell, to infer its properties [86, 87]. To perform polarimetric studies, specially manufactured antennas are required. In this work, an antenna array specifically designed for a low cross-polar is presented for polarimetric studies of hydrometeors at the GPS L1 band.

The antenna array operates at the GPS L1 band (1575.42 GHz central frequency) covering a 10 MHz full-bandwidth. The main specifications are directivity larger than 14 dB and across-polar better than -30 dB at the boresight.

The implemented antenna array is based on previous implementations of a 7 square patch elements distributed in the vertex and centre of an hexagon, as the ones used in [86, 87]. However, these designs used asymmetrically fed patches with just one probe (single polarization) or two probes (dual polarization). The asymmetry in the individual antenna element (micro strip patch) design led to a relatively low cross-polar level of just -20 dB. For the present design, a symmetrically fed square patch has been designed as the elementary antenna to build the array (Fig. A.1).

Fig. A.1. Front and back views of the antenna array (uncovered circuitry).

The antenna array was measured at the UPC Antenna Lab anechoic chamber premises [88]. The main figures of merit of the antenna array are summarized in Table A.1.

Table A.1. Main merit figures of the implemented antenna array

Directivity	14.8 dB
Cross-polar	<-30 dB (-35 dB at boresight)
Half Power Beam Width	45º
Gain	12.9 dB
Ohmic Efficiency	65%

It can be seen that the cross-polar is very low with a level of -35 dB at the boresight, and mostly below -30 dB elsewhere. The measured antenna ohmic losses are 1.9 dB (65% ohmic efficiency) derived from the antenna gain, which was estimated by using a calibrated Ridge horn antenna as a reference.

The output matching of the elementary antenna is shown in Fig. A.2, and its measured radiation patterns are presented in Fig. A.3a (standalone patch mounted on a 20 cm x 20 cm ground plane). The antenna array most relevant cuts of the measured radiation pattern are shown in Fig. A.3b

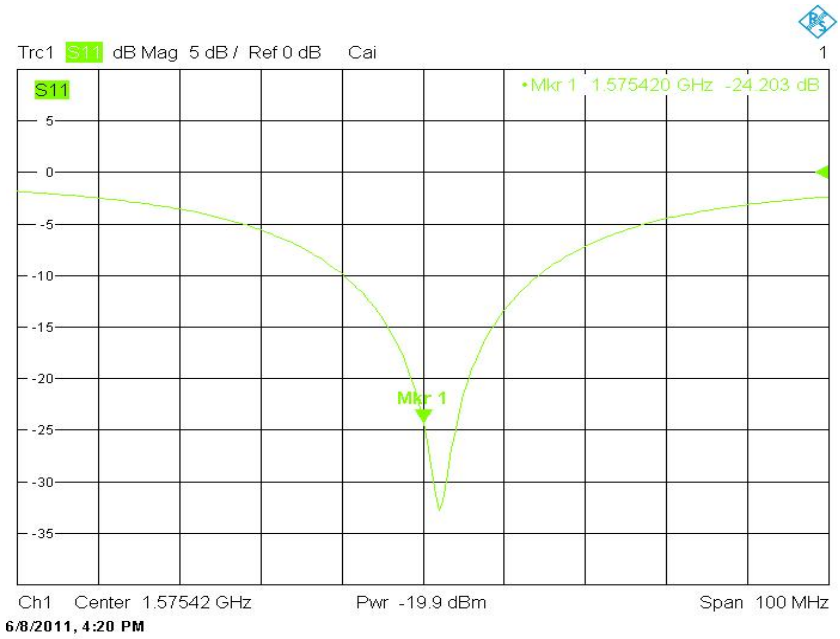

Fig. A.2. Measured output matching of the elementary antenna.

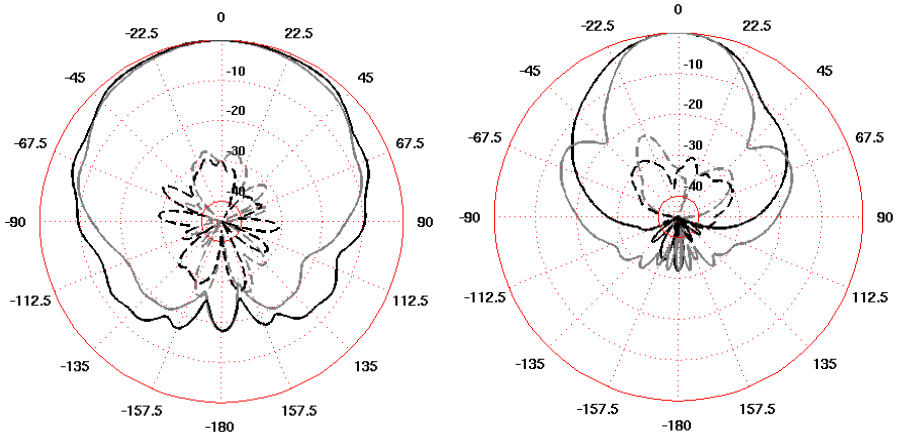

Fig. A.3. Measured radiation patterns of the a) elementary antenna, and b) full array. E-plane is in grey, H-plane is in black; solid lines are the co-polar patterns, and dashed lines correspond to the cross-polar patterns.

A.2 MOTOR CONTROLLER

When performing the PAZ campaign explained in A.1, the antenna was oriented by the AlfaSpid Rotator motor controller. During the first days of the campaign two big problems were detected: 1) As time increases, the angle bias increases sometimes around 10º per day; and 2) it was not possible to restart to a known position. Because no mechanical stop, the antenna hit the mast. The campaign was a long duration, continuous acquisition, so a system that restarts periodically to a known position and reduce the angle bias was necessary. Because the system was designed from the beginning, commands and status messages were implemented to facilitate the remote control. The circuit was so useful, that it was implemented for the other projects explained later.

A modular Motor Controller had been designed to control the instruments in azimuth and elevation coordinates. It can control two DC motors in both directions and counting the degree steps by an internal reed switch in the motors.

The rotor unit must be wired to the motor controller with two 4-wire cables, one for azimuth and the other one for elevation. The connections are in Table A.2:

Table A.2 Azimuth and Elevation controller cables

Azimuth	**Elevation**
1 Motor Drive Pin 1	5 Motor Drive Pin 1
2 Motor Drive Pin 2	6 Motor Drive Pin 2
3 Impulse Sense Pin 1	7 Impulse Sense Pin 1
4 Impulse Sense Pin 2	8 Impulse Sense Pin 2

The circuitry is operated from a 5 V power supply, while the motors and inductive sensors from a 24 V.

A.2.1 Microcontroller Module

The main control of the system is a microcontroller. As it can be seen in Fig. A.4 the microcontroller module schematic is designed to be compatible with the 40-pins PIC microcontrollers, at the moment the 16F877A, but it can be easily redesigned to accept any other microcontroller due to the modular design of the system.

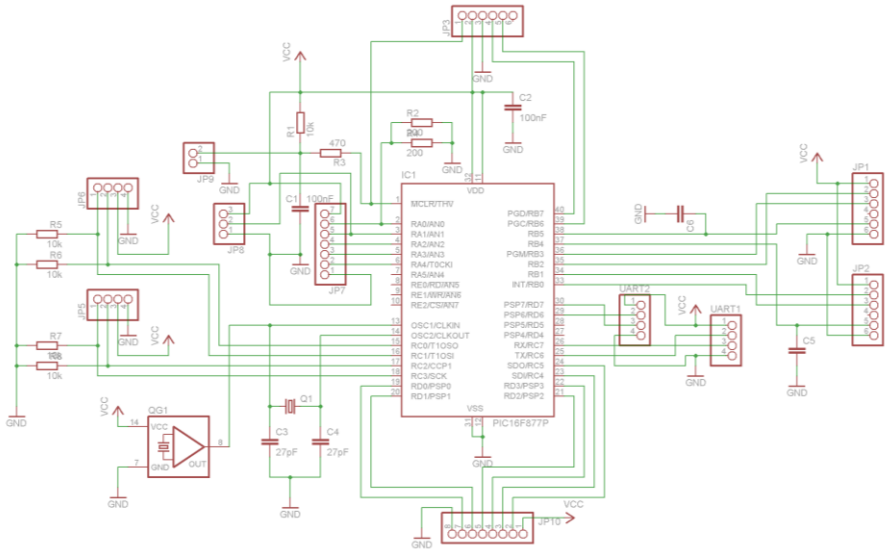

Fig. A.4 Microcontroller Module Schematic

As it can be seen in Fig. A.5 this module consists of a base socket for the microcontroller, programming pinheads and high precision crystal oscillator that can accept both configurations: crystal with capacitors or integrated version. Also provides a jumper to select if the motor reads one degree or half degree steps. The microcontroller reads the inductive sensors and the reed switches to know the position or calibrate the system, and outputs signal to the relays to move the motors in the desired direction. The communication is performed using the UART, where the microcontroller receives the following fixed length commands in ASCII:

- Goto position: Tells the controller to go to a specific direction. The format is "Wxxx yyy", where 'W' is a literal, xxx and yyy are the desired azimuth and elevation angles in degrees.
- Calibrate: Sends the motors to the initial position. The command is "R000 000", where 'R000 000' are literals and the microcontroller moves the motors to the initial position until it detects both inductive sensors in that position.
- Set position: Tells the controller to change the actual position values to the given ones. The format is "Sxxx yyy", where 'S' is a literal, xxx and yyy are the azimuth and elevation angles in degrees.

When moving, the controller returns useful information about the current position, and when it finishes executing the order it sends a message telling that.

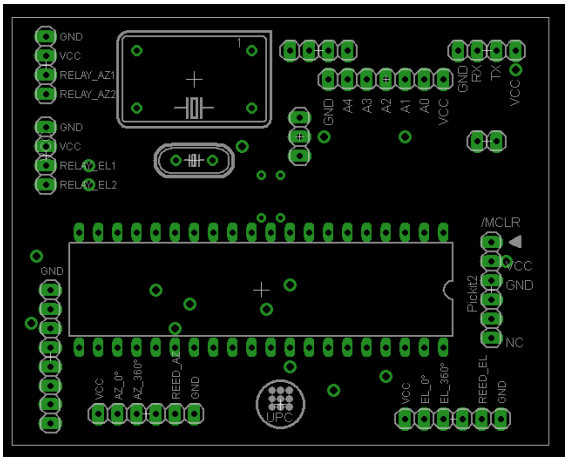

Fig. A.5 Microcontroller Module Components PCB

A.2.2 Serial Port Module

The RS232 to TTL converter is designed using a MAX3232 IC that acts as a signal level converter. As seen in Fig. A.6 it consists of the MAX3232, LEDs to monitor the transmission and reception channels, and a standard DB9 connector.

A.2.3 Relays Module

The Relays Module consists of two single pole double throw relays. As Fig. A.7 shows, every pole is connected to one terminal of the motor, the Normally Close (NC) terminal of each relay is connected to GND and the Normally Open (NO) terminal of each relay is connected to 24 V. This way, when one relay is activated, the pole connected to this relay will have 24 V, while the other one is to GND, allowing the current to flow in one direction and moving the DC motor. If the activated relay is the other one, the current will flow in the opposite direction, so the motor movement will also in the other direction. When both relays are active no current will flow because the potential in both poles will be 24 V and the difference is 0 V, as when both are inactive, and is 0 V on each pole. A protection diode is in parallel to each relay coil to protect the transistor and the digital circuitry from the reverse current caused by the

magnetic field when turning off the relay. The motor connections are also protected with a resistor, capacitor and varistor circuit because the motor's magnetic field returns a current when turned off.

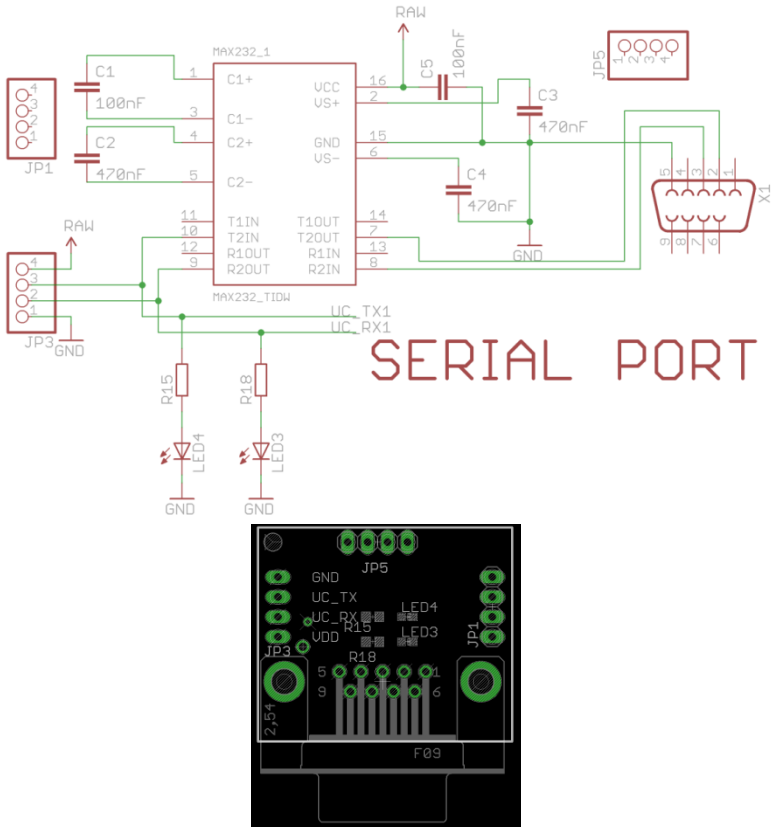

Fig. A.6 RS232 to TTL Serial Port Module Schematic and PCB

In Fig. A.8 the PCB of the relays module can be seen. It also has LEDs to see when each relay is activated. The complete system has two relay modules, one for azimuth and one for elevation.

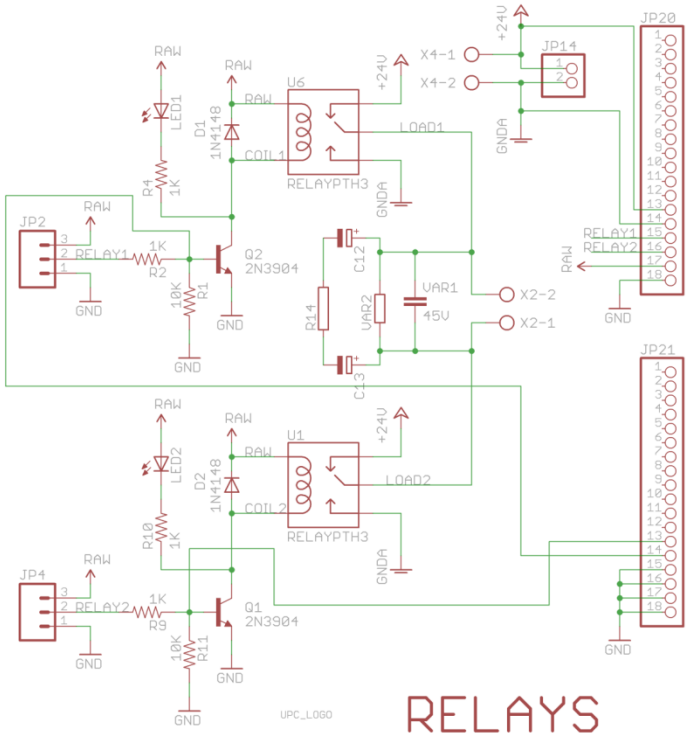

Fig. A.7 Relays Module Schematic

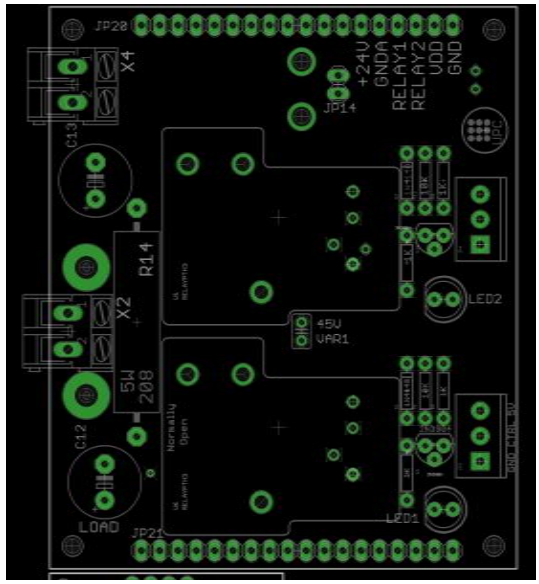

Fig. A.8 Relays Module PCB

A.2.4 Sensors Input Module

In the motor controller there are two types of sensors: inductive and reed switch. The inductive sensors (shown in Fig. A.9) are activated when a ferromagnetic material passes in the sensing distance, in this case 8 mm, and serve as points for calibrating the system providing a start position and the end position limits.

Fig. A.9 Inductive sensor: Brown cable = 24 Volts, Blue cable = GND and Black cable = output signal open collector type

The reed switches are incorporated with the motors and serve to count the steps. When a magnet passes nearby, the contact inside the reed switch is close, allowing the current to flow and be detected by the circuit. Depending on the motors, these steps can be one or half degree.

The sensors input module is shown in Fig. A.10 and it consists of four optically isolated inputs. The first three where inductive sensors can be connected in different configurations because have jumpers to select the supply and ground to connect depending if is open collector or open emitter. The fourth input is designed to send a GND signal to one of the reed switch pins, and when it is activated, the current flows turning on the optocoupler LED. Because of the long distances, all inputs are filtered to mitigate noise produced by the transmitting lines. The output signals are levelled to the microcontroller VCC, in the current case 5 V.

In Fig. A.11 the Sensors inputs module PCB is shown, and it can be noticed that the inputs can be easily changed by screw terminal blocks, the optocoupler can be replaced also. JP6, JP7, JP8, JP9, JP10 and JP11 allow the different sensors

configurations. The motor controller has two of these modules, one for azimuth and one for elevation.

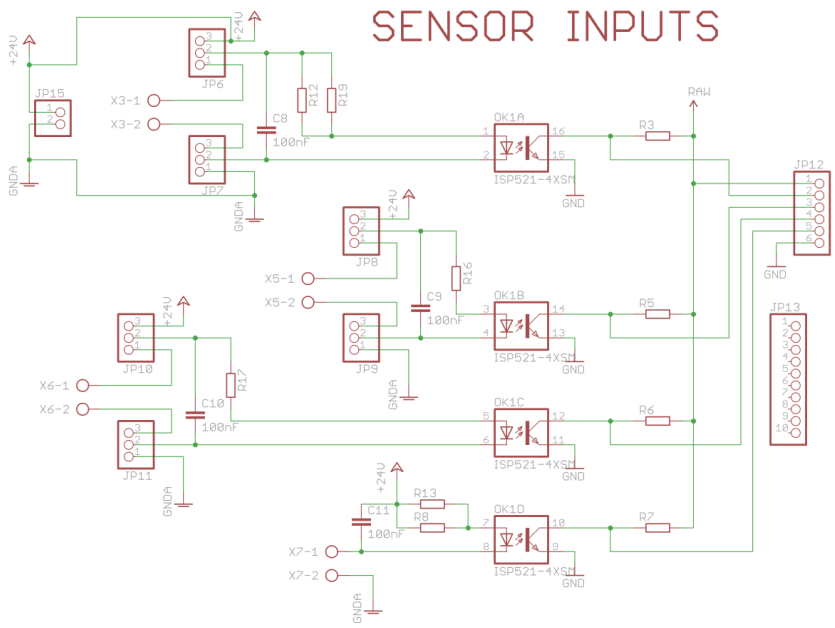

Fig. A.10 Sensors Inputs Module Schematic

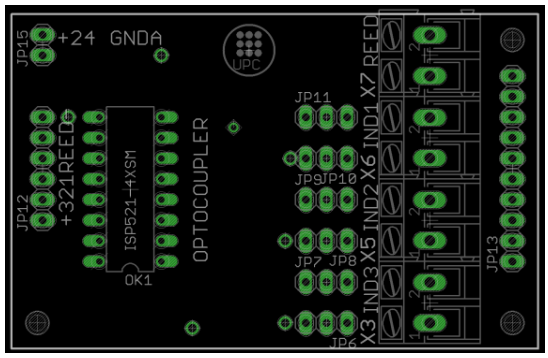

Fig. A.11 Sensors Inputs Module PCB

A.2.5 Hardware Protection Module

Due to problems with other commercial motor controllers where they lose the location, a very robust protection has been added to the system as seen in Fig. A.12. The inductive sensors, already coupled to the circuit by the Sensors Input Module,

enable or disable the movement in its direction with higher priority than the microcontroller. This is done by an AND logic gate, where the input is zero when the inductive sensor is active, disabling the movement in that direction and only allowing to turn on the other relay for moving in the opposite direction. An inverter or signal buffer can be placed depending if the inductive sensor is active low or active high. At the output, to activate the system manually, push buttons have been added and connected to an OR logic gate, activating the motors in any moment and with higher priority than the inductive sensors so caution should be taken when using this mode.

The PCB of the protection module is shown in Fig. A.13 where all the connections can be noticed, a total of four inductive sensors and the corresponding four push buttons for movement.

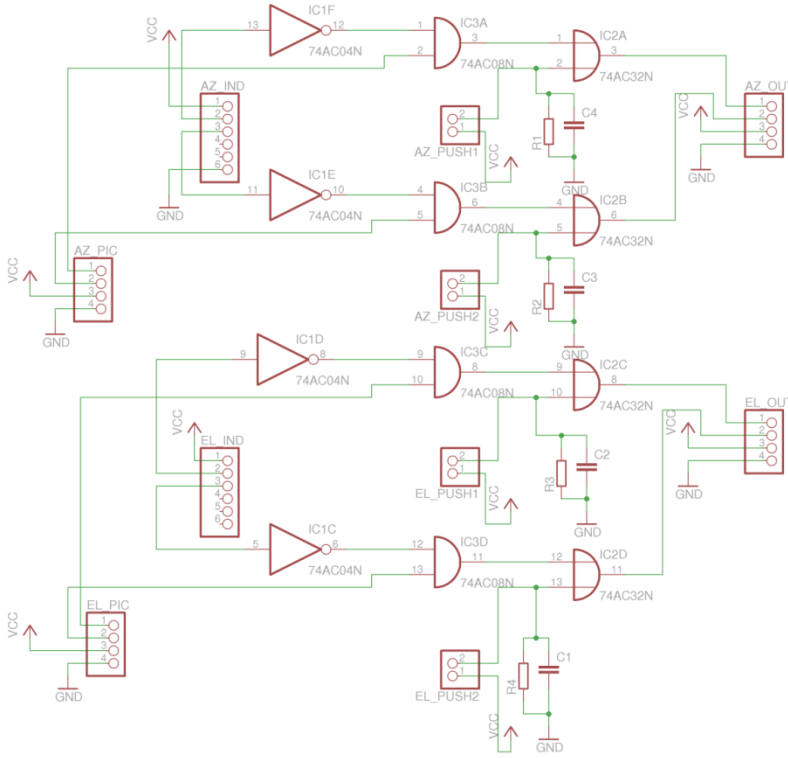

Fig. A.12 Logic Gates Protection Module Schematic

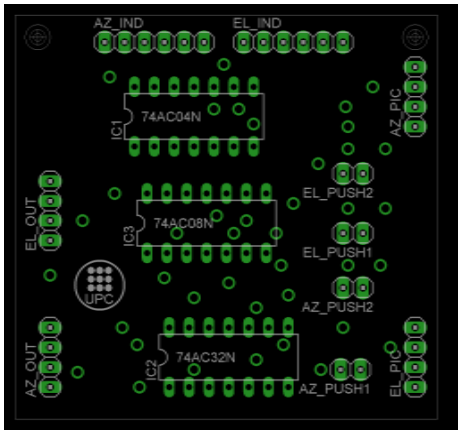

Fig. A.13 Logic Gates Protection Module Components PCB

A.2.6 System Setup

All system pieces are shown in Fig. A.14 the modules with the bottom view are in the left, and the base for mounting them are in the right. The system allows an easy prototyping and change of any damaged component during experiments.

The complete mounted motor controller is shown in Fig. A.15 a very robust and flexible system with excellent performance in the different experiments it has been used.

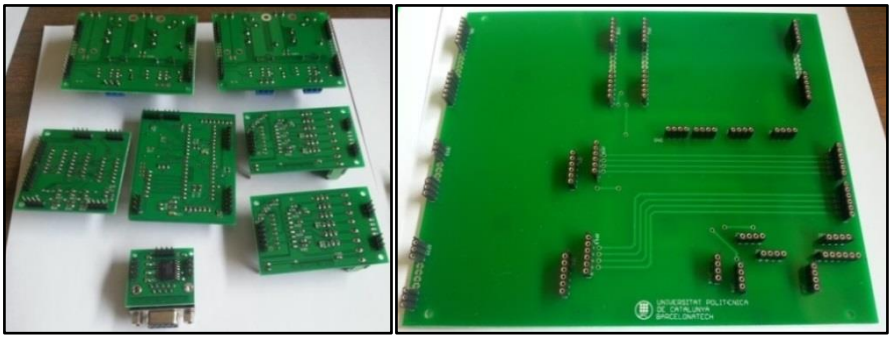

Fig. A.14 Bottom View of the Motor Controller Modules and Mounting Base for the PCBs

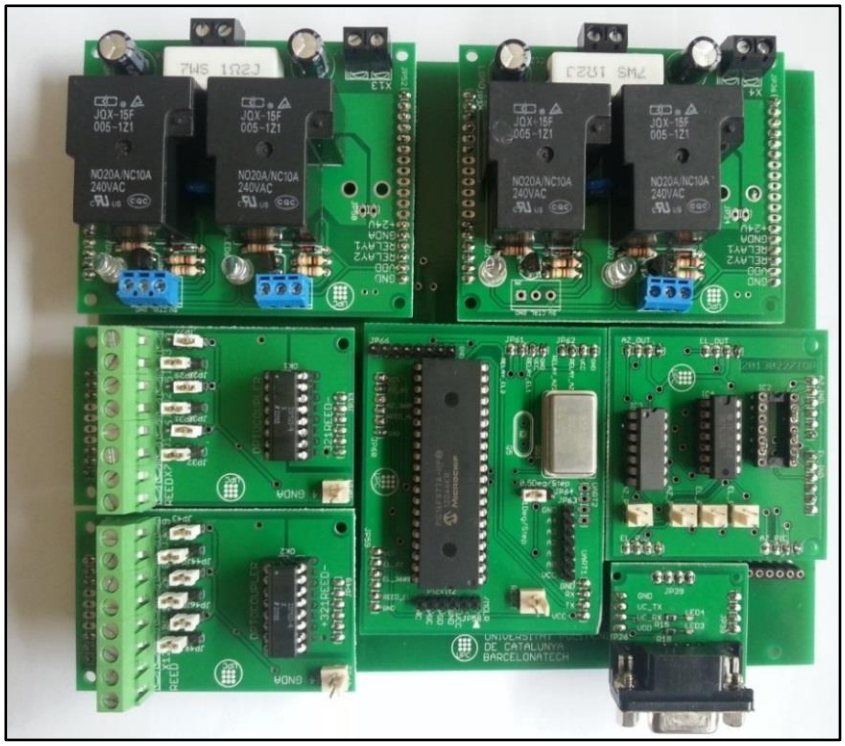

Fig. A.15 Motor Controller Complete Mounted System

A.2.7 Experiments with the motor controller

The experiments where the motor controller had been used are shown in Fig. A.16 and include the low cross-polar Antenna and LAURA 2.0 at Turò de l'Home, Parabolic dish antenna for soil moisture experiments in Tarragona [89] and the RFI Polar Survey at RSLAB rooftop in Barcelona City.

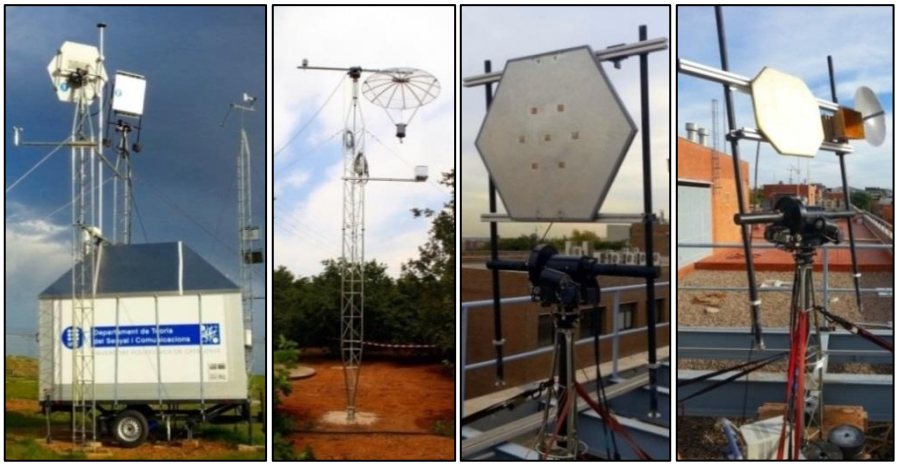

Fig. A.16 Experiments that use the designed motor controller. From left to right: GPS antenna and LAURA 2.0 at Turò de l'Home, Parabolic dish antenna in Tarragona and Multiband survey at RSLAB rooftop (GPS antenna in third figure and L, C and X antennas in the most right figure).

A.3 WIND PROTECTION AND EXTERNAL WATCHDOG CIRCUIT

To increase robustness and provide protection in the harsh environment at Turò de l'Home where temperatures goes below 0º and wind speed can go faster than 80 kilometres per hour, the systems there counted with a heated anemometer and an external watchdog system to reset the main computer in case of hang up.

The anemometer used in the system is the model 3R KWS from Darrera [90], and it is shown in Fig. A.17. It can measure wind speed with high accuracy due to its free friction technology. The structure is constructed in aluminium to provide high durability in harsh environments. The internal heater turns on automatically when temperature is below 4ºC, avoiding ice or snow accumulation, and allowing measuring at very low temperatures. Internal circuit is protected against overvoltage and polarity inversion. The specifications are shown in Table A.3.

Fig. A.17 3R KWS anemometer

Table A.3 Anemometer Technical Specifications

Range	0.4 to 40 m/s
Resolution	0.1 m/s
Accuracy	±1%
Supply Voltage	12 to 36 VDC
Current	20 mA (max.)
Heater Voltage	24 VAC/DC
Heater Current	850 mA (max.)
Output Signal	Current loop 4 to 20 mA
Operating Temperature	-40ºC to 70ºC
Dimensions	∅ 212 x 130 mm

The external watchdog circuit shown in Fig. A.18 consists of different blocks: a Universal Serial Bus (USB) microcontroller, a current to voltage converter to read anemometer signal, and another microcontroller to activate the reset relay in case no signal is received during the programmed time. The USB microcontroller is in charge of communicating the main computer with the system. It receives commands indicating to restart the watchdog timer, manual relay activation, read anemometer temperature through the conversion circuit and radiometer power supply reset by a solid state relay shown in Fig. A.19. One great advantage of this relay is the high AC power that can be controlled by a microcontroller signal in the other part of the relay, optically isolated one from another.

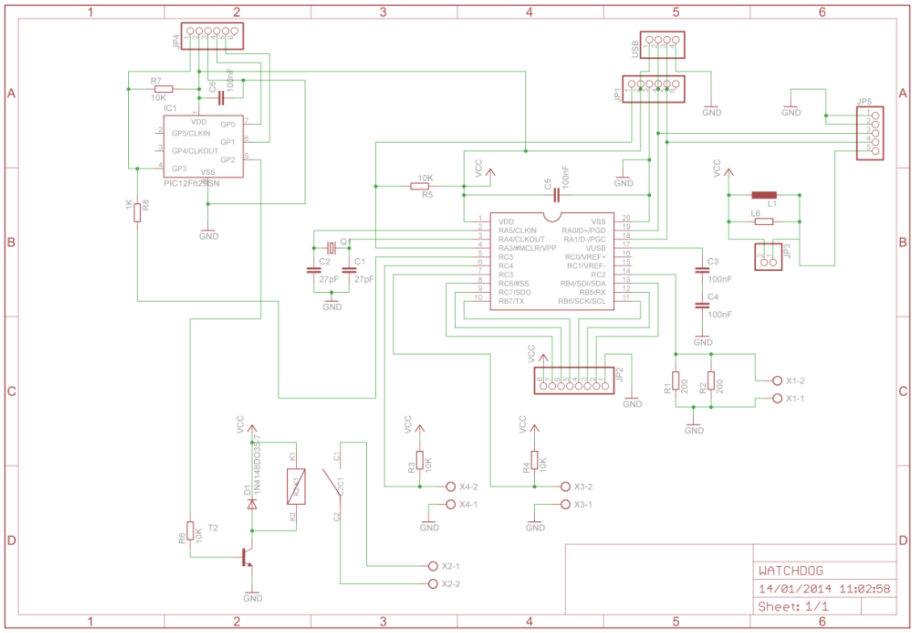

Fig. A.18 External Watchdog circuit. It consists of one USB microcontroller, one reed relay to reset the main PC, the current to voltage conversion for the anemometer signal and an independent microcontroller that activates the relay when no signal is received.

Fig. A.19 Celduc SO842074 Solid State Relay. The control signal is from 3 to 32 VDC. The output channel accepts from 12 to 275 VAC at 25 A.

The current to voltage converter is a simple resistor circuit consisting of two 200 Ω resistors in parallel, so when the current passes through them (4 to 20 mA) produces a voltage of 400 to 2000 mV that is easily readable by the microcontroller ADC and then converted to the corresponding wind speed.

The microcontroller connected to the relay is a very simple circuit that counts a predefined time and if no reset occurs from the other microcontroller, it activates the relay that has a direct connection to the main computer hardware reset button.

Figure A.20 shows the circuit board. It counts with programming connectors, USB connector and terminal blocks to connect PC Reset, radiometer power supply relay and the anemometer reading signal.

The anemometer sensor (thin blue and thin black cables) is also connected to this board, and the heaters cables, the blue one with black lines and the thick black, are connected directly to the power supply (+24 V and GND accordingly).

While the Watchdog PCB is presented in Fig. A.20, Fig. A.21 shows the complete mounted system. The USB connector is a type B to increase robustness.

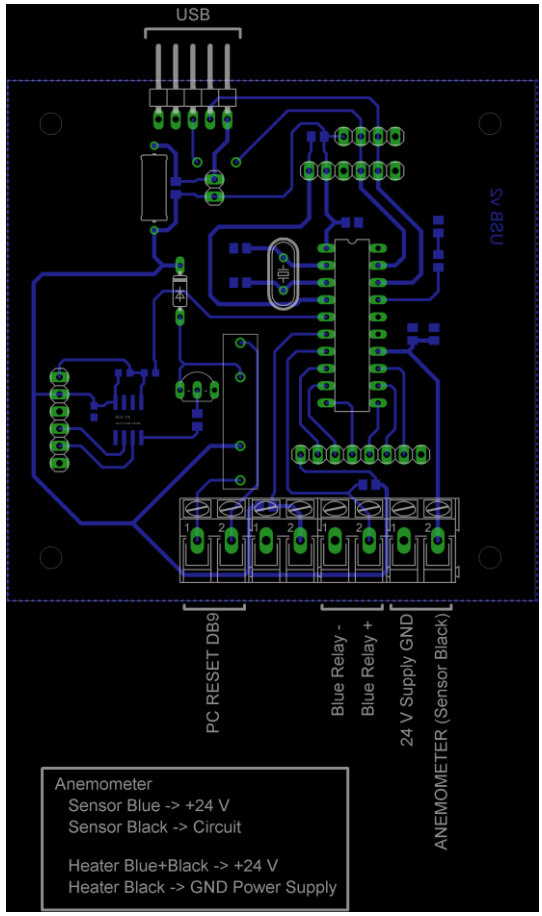

Fig. A.20 External Watchdog board. It has all the connectors for the USB, anemometer, radiometer supply and PC reset.

The reset connector has two cables that go from the reed relay in the watchdog board to the reset pushbutton on the main computer, allowing the circuit to reset it. The anemometer connector has 4 cables, two of them from the heater that go directly to the power supply, and the other two that are the sensor that goes to the converter. The motor controller sensors connector brings the sensors connections from outside to the Sensors Input module of the motor controller explained on section A.2.4. Azimuth and elevation connectors are dedicated to the azimuth and elevation motors accordingly. Both of them have four connectors, the first two to control the DC motor and the other two are the reed switch sensors for counting steps. The motor controller serial port is where it connects to the main computer serial port. The blue relay is a

solid state relay that switches on and off the radiometers power supply if reset is needed. The cables in the radiometer connector go to this relay. Power supplies are 5 and 24 VDC, at 3 and 12 A accordingly. The motor controller is the one explained in section A.2

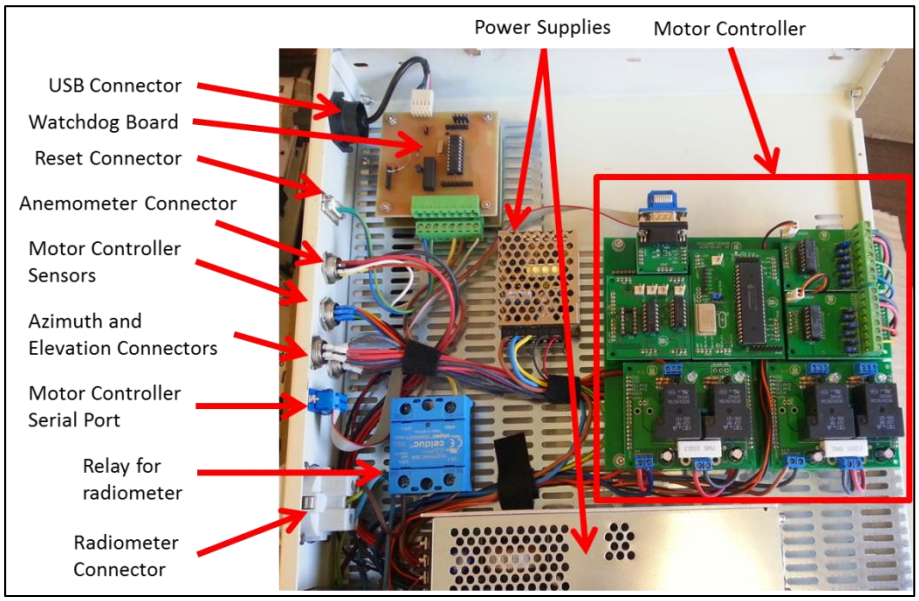

Fig. A.21 Control System for LAURA 2.0. All components are mounted on a box, with all the connectors in one side of it for easy access.

A.4 MERITXELL

MERITXELL (Multi-frequency Experimental Radiometer with Interference Tracking for eXpEriments over Land and the Littoral) [91] is a step forward advancing the understanding of the potentials of combining data from different sensors: microwave radiometers, multi-spectral and TIR cameras, and GNSS Reflectometers. It is also being used in testing radio frequency interference (RFI) detection and mitigation algorithms for microwave radiometry.

The MERITXELL is a multi-frequency dual-polarization Dicke radiometer including eight protected bands used for passive remote sensing: L-band (1.400-1.427 GHz), S-band (2.69-2.70 GHz), C-band (7.14-7.23 GHz), X-band (10.68-10.70 GHz), K-band (18.6-18.8 and 23.6-24.0 GHz), Ka-band (36.0-37.0 GHz), and W-band (86.0-92,0 GHz) as seen on Table A.4.

Table A.4 MERITXELL microwave radiometer bands and antenna parameters.

Band	Central frequency	Bandwidth	Antenna beamwidth	Main beam efficiency
L	1.4135 GHz	27 MHz	~25º	98 %
S	2.695 GHz	10 MHz	~25º	98 %
C	7.185 GHz	90 MHz	~25º	98 %
X	10.69 GHz	20 MHz	~5º	95 %
K	18.7 GHz	200 MHz	~5º	95 %
K	23.8 GHz	400 MHz	~5º	95 %
Ka	36.5 GHz	1 GHz	~5º	95 %
W	89 GHz	6 GHz	~5º	95 %

The antennas for the first three bands are arrays of 4 x 4 microstrip patch antennas with a ~25° beamwidth. The other antennas are Fresnel lens antennas with a corrugated horn at its focus to achieve a Gaussian beam with ~5° beamwidth. The radiometer is designed as a Dicke radiometer and to add flexibility and simplify the design, a Rohde & Schwarz R&S-FSP40 spectrum analyser with an extension for W-band is used as an intermediate frequency stage, as a filter and power detector for all bands. Figure A.22 shows a block diagram of the instrument.

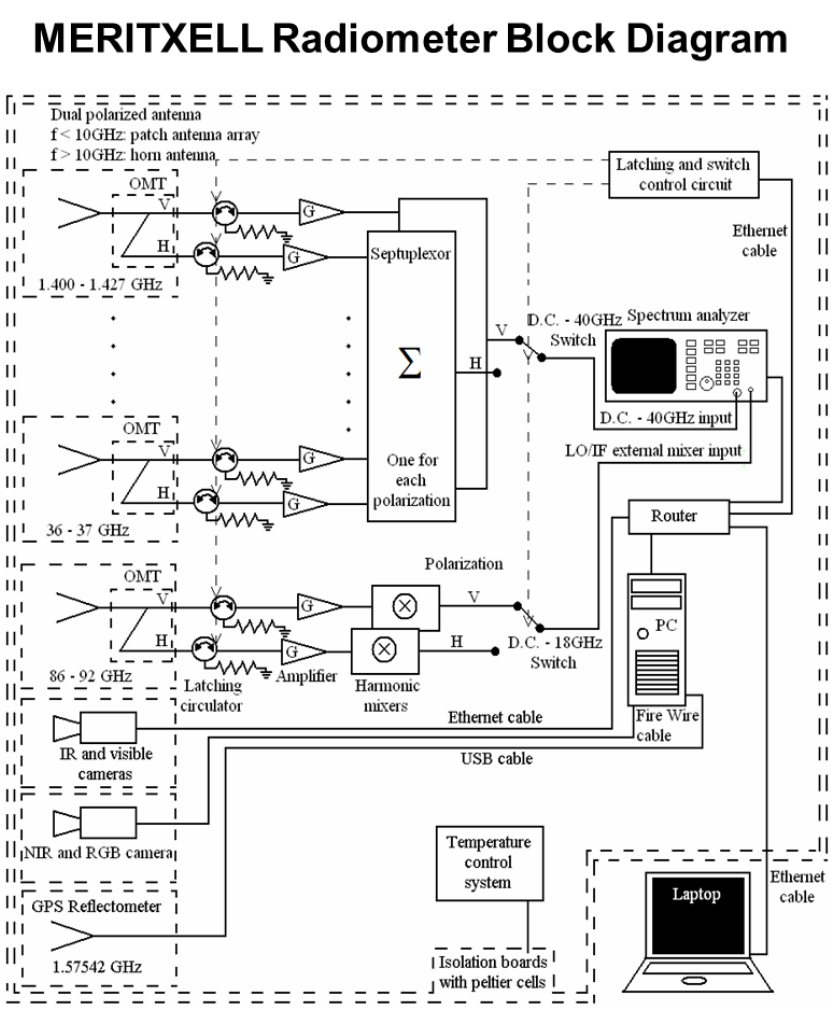

Fig. A.22 Block diagram of MERITXELL radiometer used in this work (from [86]).

The instrument also includes a video camera, a multispectral camera with four spectral bands centred at ~0.45 μm, ~0.54 μm, ~0.62 μm, and ~0.80 μm, and a Thermal Infrared camera operating in the 8-14 μm spectral range, and a GNSS-R instrument. The antennas and cameras can be seen in Fig. A.23

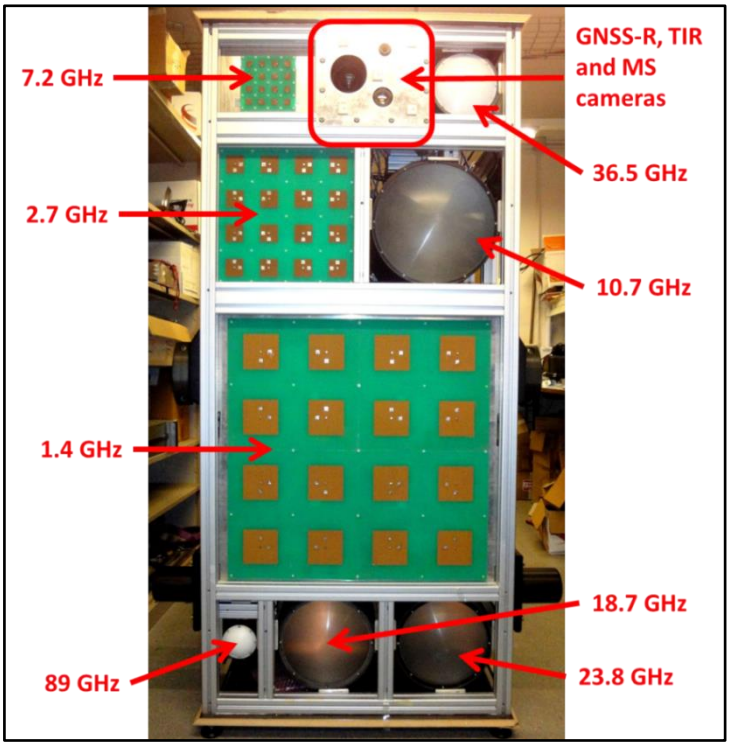

Fig. A.23 Front view of MERITXELL Radiometer

The radiometer is first calibrated following the conventional hot load - cold load technique. The detection of sinusoidal RFI with the spectrum analyser is straightforward, since it shows up as a peak when it is programmed in the usual way to sweep in time in different sub-bands of user-defined bandwidth ("resolution bandwidth"). Pulsed RFI can be also detected since the spectrum analyser can also work acquiring signals in the time domain (in-phase and quadrature components). Besides, it can generate real-time histograms and statistics of the measured signal, allowing directly the use of some of the previously described algorithms. Furthermore, off-line data processing is also possible using the sampled signals which are stored in an internal hard disk or transferred via Ethernet to a remote computer. This is the method followed in this work, since it offers the largest flexibility, and allows processing the same data in different ways.

A.4.1 Housing

The MERITXELL radiometer will be placed in the same truck as the PAUSA radiometer, as can be seen in Fig. A.24. It can move the instruments in azimuth and elevation.

Fig. A.24 PAUSA and MERITXELL radiometers housing. In the left is the PAUSA radiometer on the top of the mast. In the right is the housing with the added control cabin.

A.4.2 Electrical Part

The instrument's power input is 220 V at 50 Hz. AC as shown in Fig. A.25a. There are also four Magnetic Circuit Breakers (MCB) shown in Fig. A.25b used to protect the components detailed in Table A.5. In Fig. A.25c appears some of the DC power supplies that convert the 220 VAC to feed the DC components.

A.4.3 Temperature part

The temperatures are maintained using peltier units and heaters. It gets stable around 30 minutes from a room temperature of 30ºC as shown in Fig. A.26a. The temperature sensing system uses plug and play sensors, so when a sensor is disconnected, a special value is sent to the computer and is plotted in Fig. A.26b, where in the first 6 minutes, all the sensors where disconnected and connected again to demonstrate this effect, but in the processing program those values are discarded. The overall temperature sensors mean is 42.33 ºC and the overall temperature sensors σ_T = 1.94 ºC. The standard deviation for each sensor is presented in Table A.6

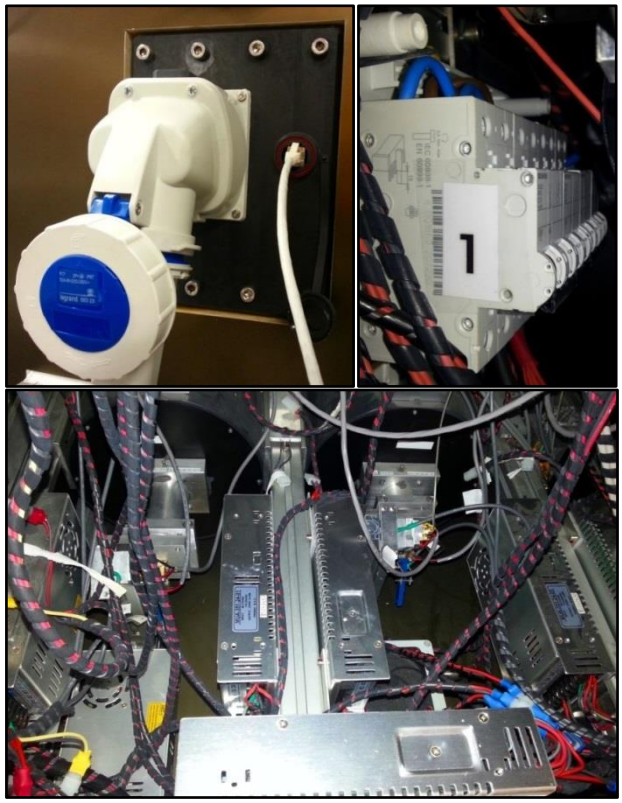

Fig. A.25 MERITXELL Power path. a) Power input. b) MCBs. c) DC power supplies.

Table A.5 MCB connected components.

MCB number	Component
1	Heaters
2	Computer, spectrum analyser, Ethernet switch, cameras, temperature and switches microcontrollers, and PID.
3	Amplifiers and RF switches.
4	Peltier cells, fans, and Pulsatron.

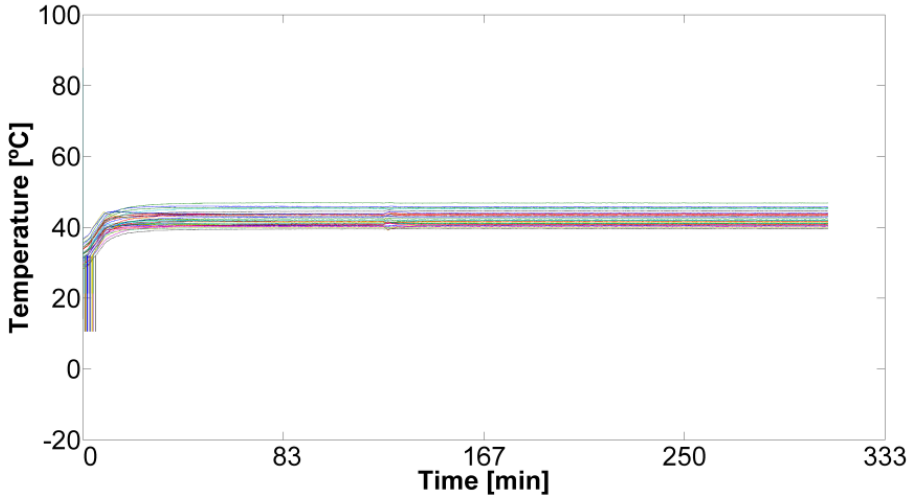

a.

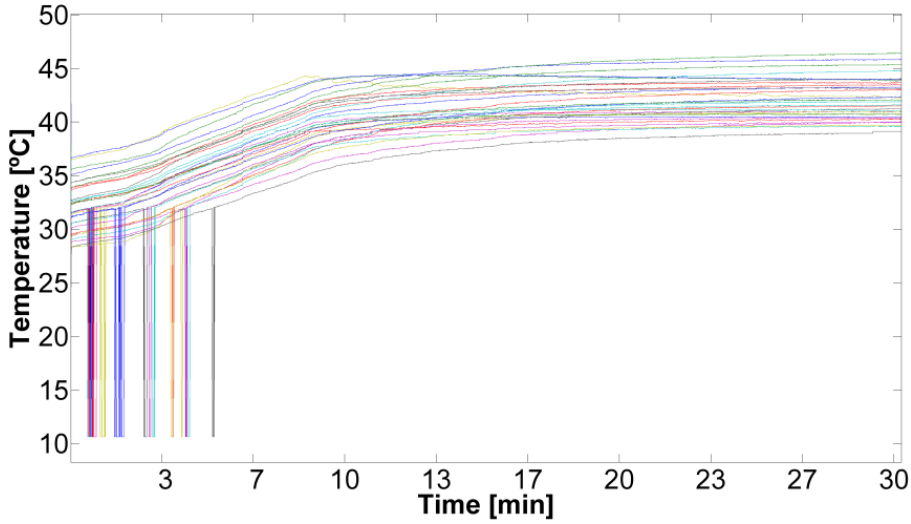

b.

Fig. A.26 MERITXELL temperature stabilization graphic. Figure A.26b is a zoom of Fig. A.26a.

Table A.6 Temperature standard deviation on the amplifiers and loads.

Sensor Number	Sensor Location	σ (in ºC)
0	7.2 GHz H Load	0.04
1	7.2 GHz V Amplifier	0.04
2	7.2 GHz V Load	0.06
3	7.2 GHz H Amplifier	0.04
4	36.5 GHz V Amplifier	0.04
5	36.5 GHz H Amplifier	0.05
6	36.5 GHz H Load	0.07
7	36.5 GHz V Load	0.03
8	23.8 GHz H Amplifier	0.05
9	23.8 GHz V Load	0.06
10	23.8 GHz H Load	0.05
11	23.8 GHz V Amplifier	0.09
12	2.7 GHz V Load	0.14
13	2.7 GHz H Load	0.05
14	2.7 GHz V Amplifier	0.05
15	2.7 GHz H Amplifier	0.04
16	10.6 GHz H Amplifier	0.06
17	10.6 GHz V Amplifier	0.09
18	10.6 GHz H Load	0.11
19	10.6 GHz V Load	0.15
20	18.7 GHz V Amplifier	0.09
21	18.7 GHz H Amplifier	0.12
22	18.7 GHz H Load	0.12
23	18.7 GHz V Load	0.11
24	90.5 GHz V Amplifier	0.04
25	90.5 GHz V Load	0.04
26	90.5 GHz H Amplifier	0.03
27	90.5 GHz H Load	0.05
28	1.4 GHz V Load	0.06
29	1.4 GHz H Amplifier	0.05
30	1.4 GHz V Amplifier	0.04
31	1.4 GHz H Load	0.06

A.4.4 Radio Frequency Paths

The incoming signals enter by the antennas and then go to its respective amplifiers that play a critical role in signal conditioning. Its specifications and radiometric sensitivity are presented below.

A.4.4.1 Amplifiers Specifications

The amplifiers specifications are presented in Tables A.7 to A.14:

Table A.7 Specs at 23°C for model # AMF-4F-01400143-04-13P:

RF Frequency Range	1.400 – 1.427 GHz
Gain	60.0 dB min.
Gain Flatness	± .050 dB max.
Noise Figure	0.40 dB max.
Input/Output VSWR	1.5:1 max.
Power Out 1 dB Compression	+13.0 dBm min.
DC Power	200 mA nominal @+15 V
Connectors	SMA female

Table A.8 Specs at 23°C for model # AMF-5F-02690270-05-10P:

RF Frequency Range	2.690 – 2.700 GHz
Gain	60.0 dB min.
Gain Flatness	± 0.50 dB max.
Noise Figure	0.50 dB max.
Input/Output VSWR	1.50:1 max.
Power Out 1 dB Compression	+10.0 dBm min.
DC Power	200 mA nominal @+15 V
Connectors	SMA female

Table A.9 Specs at 23°C for model # AMF-6F-07140723-07-10P:

RF Frequency Range	7.145 – 7.235 GHz
Gain	60.0 dB min.
Gain Flatness	± 0.50 dB max.
Noise Figure	0.70 dB max.
Input/Output VSWR	2.00:1 max.
Power Out 1 dB Compression	+10.0 dBm min.
DC Power	250 mA nominal @+15 V
Connectors	SMA female

Table A.10 Specs at 23°C for model # AMFW-7S-10601070-65K-10P:

RF Frequency Range	10.60 – 10.70 GHz
Gain	60.0 dB min.
Gain Flatness	± 0.50 dB max.
Noise Temperature	65 °K max.
Input/Output VSWR	2.00:1 max.
Power Out 1 dB Compression	+10.0 dBm min.
DC Power	275 mA nominal @+15 V
Connectors, Input	WR90
Output	SMA female

Table A.11 Specs at 23°C for model # JSWK44-18601880-15-8P:

Operating Temperature	0 – 60°C
RF Frequency Range	18.6 – 18.8 GHz
Gain	60 dB min.
Gain Flatness	± 0.5 dB max.
Noise Figure	1.5 dB max.
Input VSWR	2:1 max.
Output VSWR	2:1 max.
Power Out 1 dB Compression	+8 dBm min.
DC Power	325 mA nominal @ +15V
Connectors, Input	WR42
Output	K female

Table A.12 Specs at 23°C for model # JSWK44-23602400-19-8P:

Operating Temperature	0 – 60°C
RF Frequency Range	23.6 – 24 GHz
Gain	60 dB min.
Gain Flatness	± 1.0 dB max.
Noise Figure	1.9 dB max.
Input VSWR	2:1 max.
Output VSWR	2:1 max.
Power Out 1 dB Compression	+8 dBm min.
DC Power	350 mA nominal @ +15V
Connectors, Input	WR42
Output	K female

Table A.13 Specs at 23°C for model # JSWK44-36003700-26-8P:

Operating Temperature	0 – 60°C
RF Frequency Range	36 – 37 GHz
Gain	60 dB min.
Gain Flatness	± 1.8 dB max.
Noise Figure	2.6 dB max.
Input/Output VSWR	2:1 max.
Power Out 1 dB Compression	+8 dBm min.
DC Power	350 mA nominal @ +15V
Connectors, Input	WR28
Output	K female

Table A.14 Specs at 23°C for model # VLNA-8906-6060:

RF Frequency Range	86 - 92 GHz
Gain	60 dB min.
Gain Flatness	±1.0 dB (typ)
Noise Figure	6.0 dB (typ)
Power Out 1 dB Compression	+3 dBm min.
Input/Output VSWR	2:1 (typ)
DC Power	300 mA (typ) @ +8 V
RF Connectors	WR-10 , with UG387/U Mod Flange

A.4.4.2 Radiometric Stability

In order to determine the best range of integration time for optimum use of the system, the characterization of the different channels noise and stability has been perform measuring the Allan's variance [92]. The Allan's variance measurements for all the bands are shown in Fig. A.27, and the optimum integration time and radiometric resolution for all the amplifiers are presented in Table A.15.

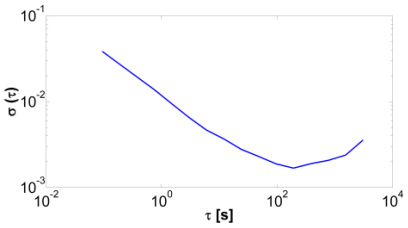

a.

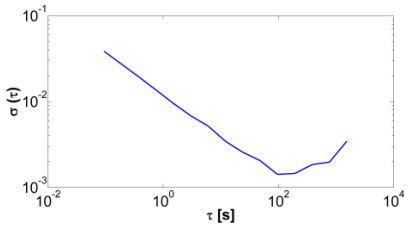

b.

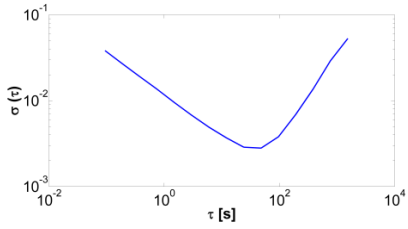

c.

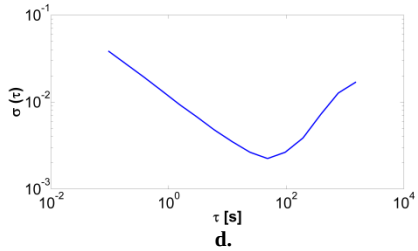

d.

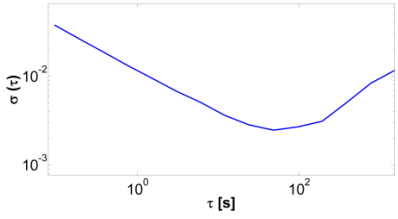

e.

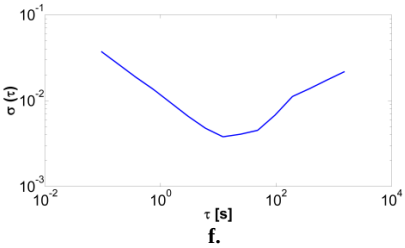

f.

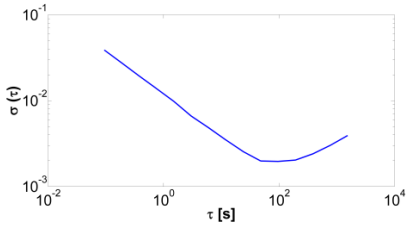

g.

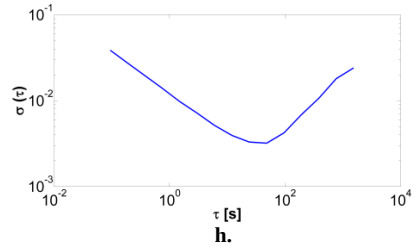

h.

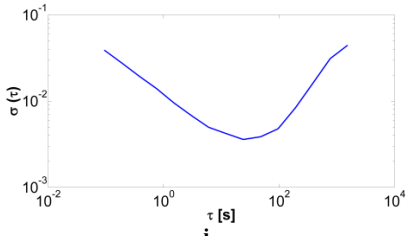

i.

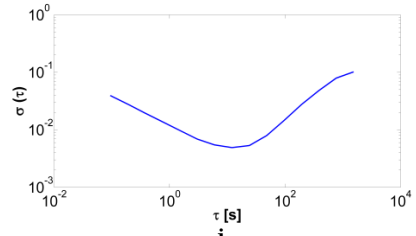

j.

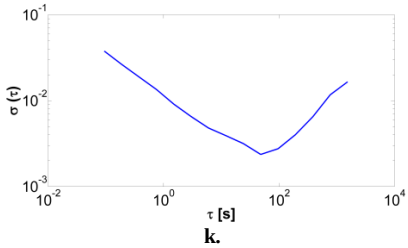

k.

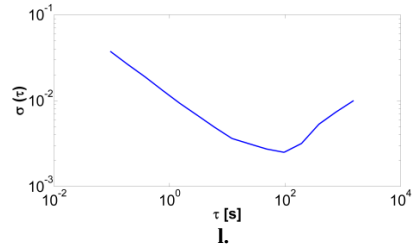

l.

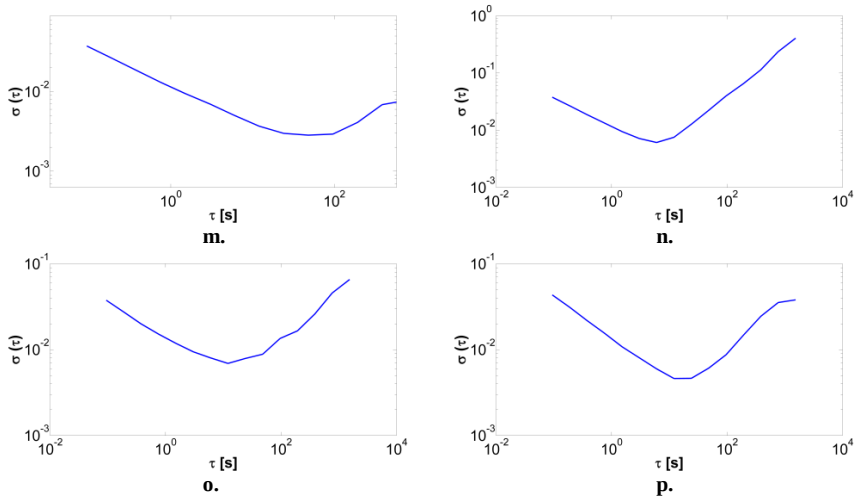

Fig. A.27 MERITXELL Allan variance for different RF paths with 50 Ohms load:
L-Band (1.40 GHz - 1.427 GHz) a) Horizontal polarization. b) Vertical Polarization.
S-Band (2.69 GHz - 2.70 GHz) c) Horizontal polarization. d) Vertical Polarization.
C-Band (7.14 GHz - 7.23 GHz) e) Horizontal polarization. f) Vertical Polarization.
X-Band (10.6 GHz - 10.7 GHz) g) Horizontal polarization. h) Vertical Polarization.
K-Band (18.6 GHz - 18.8 GHz) i) Horizontal polarization. j) Vertical Polarization.
K-Band (23.6 GHz - 24.0 GHz) k) Horizontal polarization. l) Vertical Polarization.
Ka-Band (36 GHz - 37 GHz) m) Horizontal polarization. n) Vertical Polarization.
W-Band (86 GHz - 92 GHz) o) Horizontal polarization. p) Vertical Polarization.
Table A.15 Integration time and radiometric resolution for all the amplifiers

Table A.15 Integration time and radiometric resolution for all the amplifiers

	Horizontal Polarization		**Vertical Polarization**	
Central Frequency	**Integration Time (s)**	**Radiometric Sensitivity**	**Integration Time (s)**	**Radiometric Sensitivity**
L-Band (1.4135 GHz)	192	1.68×10^{-3}	192	1.456×10^{-3}
S-Band (2.695 GHz)	48	2.799×10^{-3}	48	2.24×10^{-3}
C-Band (7.185 GHz)	48	2.47×10^{-3}	48	4.511×10^{-3}
X-Band (10.65 GHz)	48	1.98×10^{-3}	48	3.194×10^{-3}
K-Band (18.7 GHz)	24	3.586×10^{-3}	24	5.329×10^{-3}
K-Band (23.8 GHz)	48	2.361×10^{-3}	96	2.499×10^{-3}
Ka-Band (36.5 GHz)	48	2.84×10^{-3}	6	6.108×10^{-3}
W-Band (89 GHz)	12	6.907×10^{-3}	12	4.609×10^{-3}

As conclusion from the Table A.15, the general trend is that the lower frequency bands amplifiers allow higher integration times and have more radiometric sensitivities than higher frequency bands.

A.4.5 Instruments

A.4.5.1 Spectrum Analyser

The FSP40 Rohde & Schwarz spectrum analyser shown in Fig. A.28, is used as a common power detector back-end stage. The instrument is controlled remotely using an Ethernet connection.

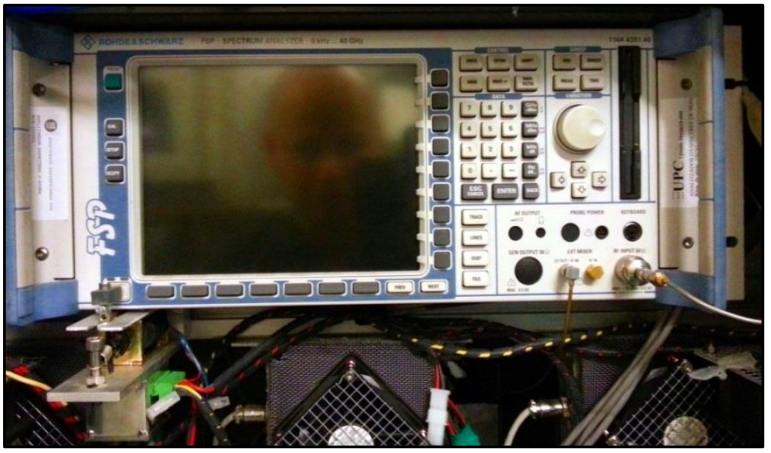

Fig. A.28 Rohde & Schwarz spectrum analyser

The Pulsatron shown in Fig. A.29 is constructed using a solenoid and a returning spring to switch the power button because the spectrum analyser does not have a Wake On Local Area Network (WOL) feature.

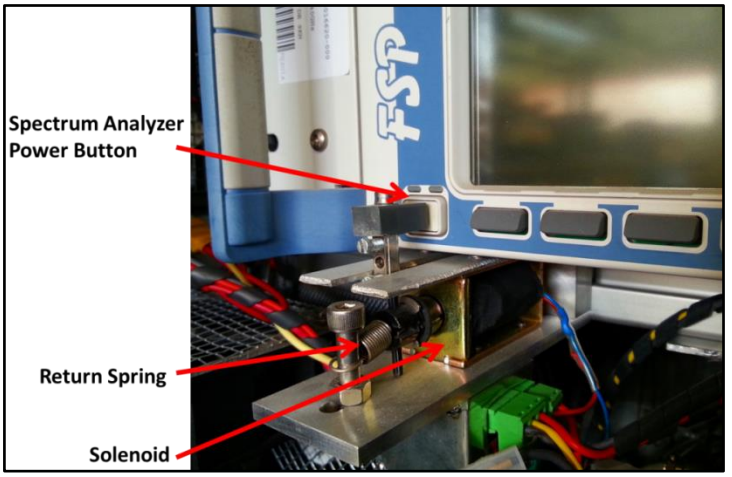

Fig. A.29 MERITXELL PULSATRON System to turn on and off the Spectrum Analyser remotely.

A.4.5.2 Cameras

There are three cameras included in the system in order to obtain optical data in addition to the radiometric captures.

A.4.5.2.1 MS-4100 Camera Module

The multispectral camera shown in Fig. A.30 uses a beam splitting prism and three CCD sensors to acquire images in 3-5 spectral bands within the 400-1100 nm sensitivity of the sensors.

Performance Specifications are taken from the provided datasheet and are show in Table A.16.

Table A.16 Performance Specifications for MS-4100 Camera

Image device	1-inch Interline Transfer CCD
Picture elements	1920(H) x 1080(V)
Pixel size	7.4 x 7.4 um
Pixel clock rate	25 MHz
Sensing area	14.2 x 8 mm
Frame rate	10 frames/second
Digital image output	8 bits x 4 taps or 10 bits x 3 taps, CameraLink, EIA-644 (LVDS) or RS-422
Signal /noise	60 dB
Lens mount	Nikon Bayonet Mount
Electronic shutter	Range: 1/10,000 - 1/10 sec. , controlled via RS-232 input
Gain selection Range:	0-36 dB, controlled via RS-232 input
External trigger input	Edge or level , three modes
External trigger source	BNC or Frame Grabber (optical isolator on BNC)
Exposure control	Manual or automatic
White-balance	Manual or semi-automatic
Noise reduction	Correlated double sampling
Usability features	Digital crosshairs, colour-plane multiplexing
Operating temperature	0-50 C
Operating voltage	12 VDC
Power consumption	15 Watts
Weight	1.8 kg
Programmable functions	Gain, exposure time, multiplexing, trigger modes, custom processing
Video Preview	Progressive scan RGB (1280 x 1024 max display resolution), Gamma correction, 2x and 4x digital zoom
Camera Back Dimensions	149 x 89 x 97mm

Fig. A.30 MS-4100 multispectral camera.

A.4.5.2.2 Infrared Camera

An infrared camera measures and images the emitted infrared radiation from an object. The model used is the A320 from Flir and has a spectral range of 7.5 – 13 μm. Using this camera the accuracy of the physical temperature of the bodies measured by the radiometer is increased. The camera can be seen in Fig. A.31

Fig. A.31 Flir A320 infrared camera.

A.4.5.2.3 Visible Camera

A visible camera is used to obtain real-time imagery. The model is a Q series IP camera controlled over Ethernet and is shown in Fig. A.32.

Fig. A.32 Q model IP camera.

A.4.5.3 Inclinometer

Because the emissivity of the bodies strongly depends on the incidence angle of the measuring instrument, an inclinometer capable of measuring azimuth and elevation angle of the MERITXELL is incorporated inside and controlled by the internal computer. The specifications are detailed in Table. A.17 and the instrument is shown in Fig. A.33.

Table A.17 DXL360S inclinometer specifications.

Accuracy	DXL360S ± (0.08° + 1%)
Measuring range	Single axis 360°, Dual axis ±40°
Resolution	DXL360S 0.01°
Response time	<0.4 second
Audio sound	60dB @ 30cm
Operating temperature	0 to 50°C
Storage temperature	-10 to 60°C
User Interface	Mono-colour LCD with backlight
Supply Power	Rechargeable Li-Ion Battery, 3.7Volt.
Charger port	5V 500mA Mini type-B USB port
Power Consumption	Standby 200uA, Operation 20mA.
Standby Battery Life	2000 hours
Operating Battery Life	40 hours
Dimensions (in mm)	66(L) x 64(W) x 29(H)

Fig. A.33 DXL360S inclinometer.

A.4.5.4 Temperatures Monitor and Switch Control over Ethernet

MERITXELL radiometer has a modular design, with the blocks connected by the Ethernet protocol. A circuit is designed to monitor the temperatures and control the switches. Its schematic is shown in Fig. A.34, the circuit board in Fig. A.35, and the system in Fig. A.36.

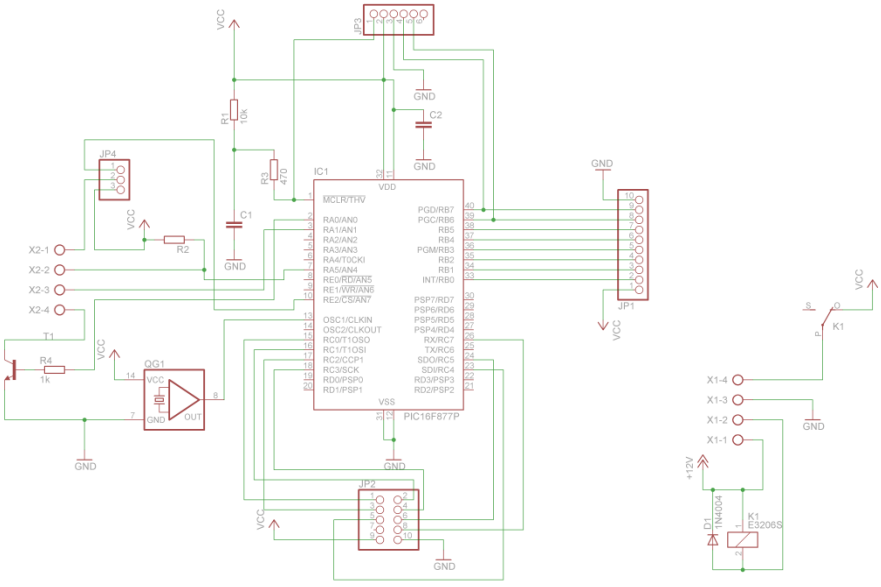

Fig. A.34 Temperature monitor and Switch Control Schematic

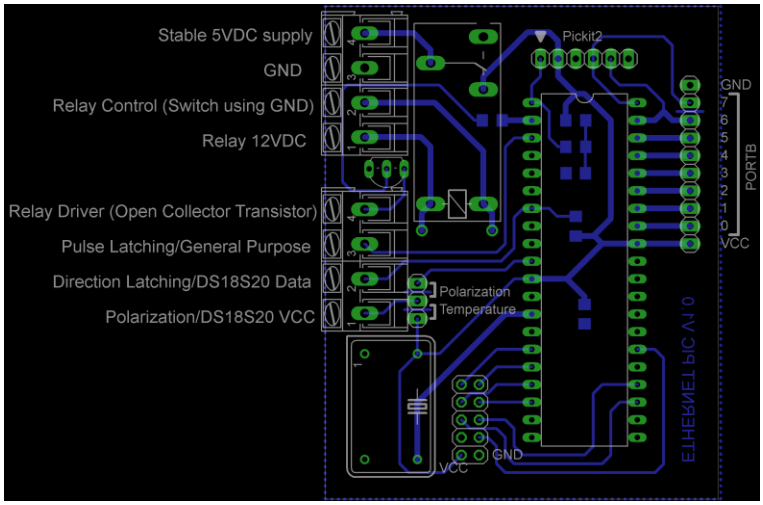

Fig. A.35 Temperature monitor and Switch Control circuit board

In order to periodically measure the temperatures of the matched loads and the amplifiers of every radiometric subband and polarization, 32 DS18B20 digital thermometers (one for each of the 16 amplifiers and 16 matched loads) are used.

The DS18B20 digital thermometer provides 9-bit to 12-bit Celsius temperature measurements. It communicates over a 1-Wire bus designed by Maxim, using only one wire for transmitting and receiving data. It has an operating temperature range of -55°C to +125°C and is accurate to ±0.5°C over the range of -10°C to +85°C. Each DS18B20 has a unique 64-bit serial code, which allows multiple DS18B20s to function on the same 1-Wire bus.

These electronic components are controlled by a C-programmed PIC microcontroller. This way, temperatures of the matched load and the amplifiers are monitored and may be used to calibrate and correct the radiometric measurements.

Switches and latching circulators select the polarization and the radiometric input (antenna or matched load) for the different measurement bands. To control the 6 switches and 10 latching circulators that select the radiometric input, and the 2 switches that select the polarization, another PIC microcontroller is used. The software for both PICs is implemented in the same code, but using the selection jumper JP4 shown in Figs. A.34 and A.35, the boards can act as a Temperature monitor or as a Switch controller. The chosen microcontroller is the 16F877A from the

microchip family, and the Ethernet control is performed by the Mikroelektronika Ethernet Board, as shown in Fig. A.36.

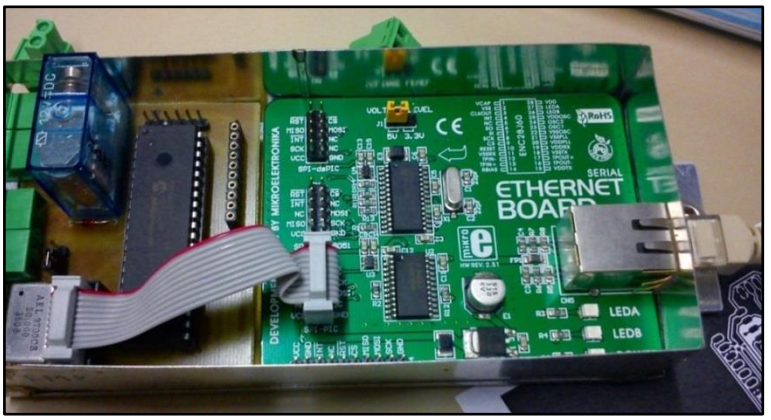

Fig. A.36 Temperature monitor and Switch Control implemented circuit

A.4.5.5 Computer devices

In order to simplify the instruments control, a computer is included to communicate via Ethernet through a sixteen port Ethernet switch. Only the inclinometer and the multispectral camera are connected directly to the USB and to the PCI ports accordingly. The computer is located over the spectrum analyser as it can be seen in Fig. A.37a and the Ethernet switch in Fig. A.37b

Fig. A.37 Computer devices: a) Computer over spectrum analyser. b) Ethernet Switch.

A.4.6 MERITXELL Control Software

MERITXELL custom control software is used to:

1) Spectrum analyser data capture as show in Fig. A.38,
2) Temperature monitor, switch control and spectrum analyser turn on and off as shown in Fig. A.39.

Data capture software has many options to control the spectrum analyser. Instrument configuration part sends the resource descriptor in order to connect the spectrum analyser with the PC. It also has the options to reset the instrument and leave the screen blank while measuring.

Configurable parameters for spectrum capture are central frequency, span, sweep time, resolution bandwidth, video bandwidth and measure repeat times.

IQ measure configurable parameters include central frequency, reference level, sampling rate, bandwidth, number of samples, step frequency (zero to stay at the same frequency or different to set an increment) and measure repeat times.

Data can be saved in Binary or Text format. Binary is very fast and more compact than Text, but Text is easy for human reading. The trace detector is also selectable.

The software also includes a Script Editor, in order to perform different type of measurements.

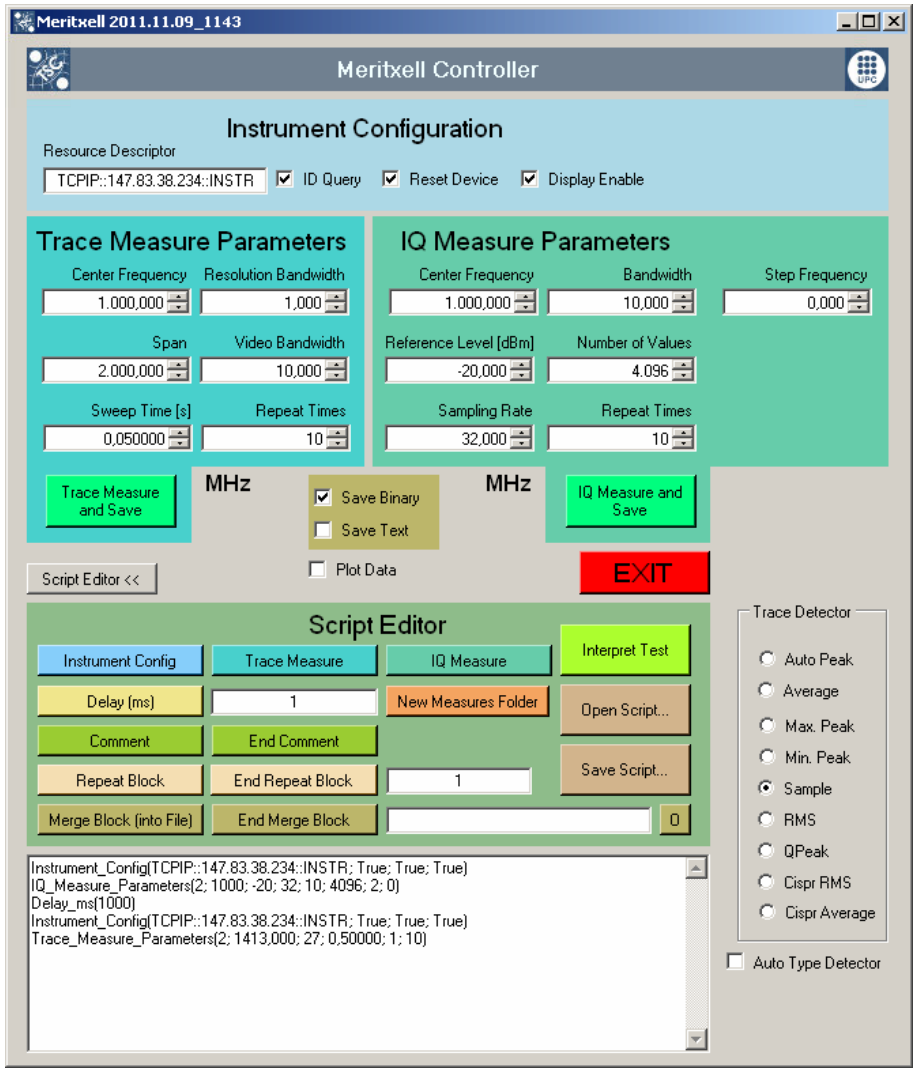

Fig. A.38 MERITXELL Main Control Software

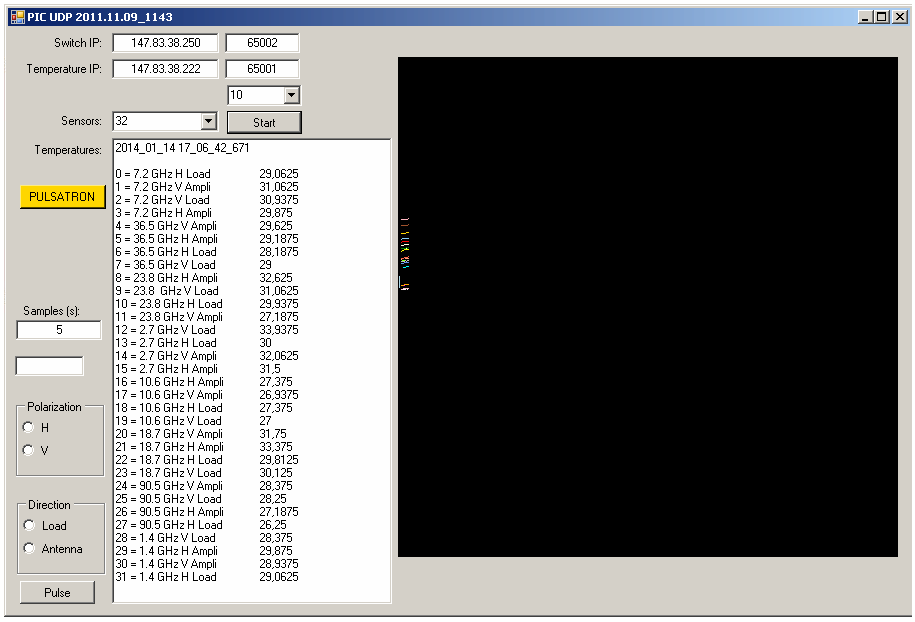

Fig. A.39 MERITXELL Temperature monitor and Switch Control Software

The control software also includes a part for communicating with the PIC microcontrollers through Ethernet protocol. Both microcontrollers have their own IP address and port. This software polls the temperature sensors by sending to the microcontroller the unique address of the sensor and reading the response. Then it converts to decimal reading and shows in the textbox with the corresponding name. Also in the black square the signals are plotted just as reference to see if the sensors are OK. Sampling time is configurable in seconds. The Polarization (horizontal or vertical) and direction (load or antenna) is selectable in this software too. The PULSATRON button is used to turn on or off the Spectrum analyser. The control software also includes a part for communicating with the PIC microcontroller.

A.5 TANGREAT COMMERCIAL JAMMER

In this work, the characterized GPS Jammer is from the TANGREAT manufacturer. It has been used to study the effects of jamming signals and also to develop and test the mitigating algorithms with real data. The specifications shown next are taken from the webpage [93] and shown in Fig. A.40:

Name: GPS Anti-tracking jammers
Model: TG-121G
Features: TG-121G is a Portable GPS Jammers, Handheld GPS Jammer, Handheld Global GPS Jammers, Anti-tracking jammers
•Highly portable.
•Palm Sized
•On/Off switch make it use more user-friendly.
•Higher efficient jamming effect by the high power 2.0 watt design.
•Optional cover to make the jammer easier to carry.

Type	Output Port	Frequency	Radius range
Global	GPSL1	1500-1600 MHz	5-15M @ depending on the mobile service provider's network condition
	GPSL2	1220-1230 MHz	
	GPSL3	1200-1210Mhz	
	GPSL4	1250-1280Mhz	
	GPSL5	1170-1180Mhz	
Colours: Light Blue			
Power supply: AC110-240V **12V** **Built-in Battery**:1800mA/h			

Total output Power: 2 watt
Device Size: 113*60*31mm Package Size: 209*52*86mm
Net Weight: 0.275Kg Gross Weight: 0.775Kg
Colour: Sky blue
Built-in battery time : 1 hour
Signal source: Synthesized Operation
Temperature: -10℃ to +50℃
Humidity: 5% to 80%
Feature and Advantage:
1.Charging while working.
2. Each band can work separately or simultaneously.
3.Built-in fans and Wind slots on two sides design and inside coolers make a constant cooling working.

Application: Prevent Commercial tracking, Killer track, Illegal location tracking.

Although they claim a 5 to 15 meters of distance, this information is not accurate because in open air the distance is much higher, and the mobile service provider's network condition doesn't affect the GPS satellites transmission.

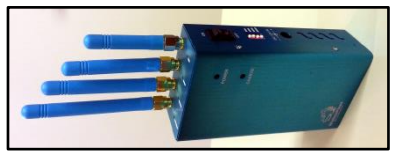

Fig. A.40 TG-121G Tangreat GPS jammer.

LIST OF PUBLICATIONS

JOURNAL ARTICLES

Forte, G.F.; Querol, J.; Camps, A.; Vall-llossera, M., "Real-Time RFI Detection and Mitigation System for Microwave Radiometers," *Geoscience and Remote Sensing, IEEE Transactions on* , vol.51, no.10, pp.4928,4935, Oct. 2013
doi: 10.1109/TGRS.2013.2267595

Forte, G.F.; Tarongi Bauza, J.M.; dePau, V.; Vall llossera, M.; Camps, A., "Experimental Study on the Performance of RFI Detection Algorithms in Microwave Radiometry: Toward an Optimum Combined Test," *Geoscience and Remote Sensing, IEEE Transactions on* , vol.51, no.10, pp.4936,4944, Oct. 2013
doi: 10.1109/TGRS.2013.2273081

Ramos-Perez, I.; Camps, A.; Bosch-Lluis, X.; Rodriguez-Alvarez, N.; Valencia-Domènech, E.; Park, H.; **Forte, G.**; Vall-llosera, M., "PAU-SA: A Synthetic Aperture Interferometric Radiometer Test Bed for Potential Improvements in Future Missions". Sensors 2012, 12, 7738-7777.

Ramos-Perez, I.; **Forte, G.F.**; Camps, A.; Bosch-Lluis, X.; Valencia, E.; Rodriguez-Alvarez, N.; Park, H.; Vall-llosera, M., "Calibration, Performance, and Imaging Tests of a Fully Digital Synthetic Aperture Interferometer Radiometer," *Selected Topics in Applied Earth Observations and Remote Sensing, IEEE Journal of* , vol.5, no.3, pp.723,734, June 2012
doi: 10.1109/JSTARS.2012.2193118

Ramos-Perez, I.; Bosch-Lluis, X.; Camps, A.; Gonzalez, V.; Rodriguez-Alvarez, N.; Valencia, E.; Hyuk Park; Vall llosera, M.; **Forte, G.**, "Optimum Intercalibration Time in Synthetic Aperture Interferometric Radiometers: Application to SMOS," *Geoscience and Remote Sensing Letters, IEEE* , vol.9, no.4, pp.774,777, July 2012
doi: 10.1109/LGRS.2011.2181483

CONFERENCE PROCEEDINGS

Forte, G.F.; Querol, J.; Park, H.; Camps, A., "Digital back-end for RFI detection and mitigation in Earth observation," *Geoscience and Remote Sensing Symposium (IGARSS), 2013 IEEE International* , vol., no., pp.1908,1911, 21-26 July 2013
doi: 10.1109/IGARSS.2013.6723177

Forte, G.F.; Camps, A.; Ramos, I.; Vall-llossera, M., "Digital back-end for RFI detection and mitigation in microwave radiometers," *Geoscience and Remote Sensing Symposium (IGARSS), 2012 IEEE International* , vol., no., pp.2953,2955, 22-27 July 2012
doi: 10.1109/IGARSS.2012.6350706

Forte, G.F.; Camps, A.; Tarongi, J.M.; Vall-llossera, M., "Study of radio frequency interference effects on radiometry bands in urban environments," *Geoscience and Remote Sensing Symposium (IGARSS), 2012 IEEE International* , vol., no., pp.1069,1072, 22-27 July 2012
doi: 10.1109/IGARSS.2012.6351364

Forte, G.F.; Tarongi, J.M.; Camps, A., "Hardware implementation of a wavelet-based radio frequency interference mitigation algorithm for microwave radiometers,"*Geoscience and Remote Sensing Symposium (IGARSS), 2011 IEEE International* , vol., no., pp.2241,2244, 24-29 July 2011
doi: 10.1109/IGARSS.2011.6049653

Tarongi, J.M.; **Forte, G.F.**; Camps, A., "Experimental study of radio-frequency interference detection algorithms in microwave radiometry," *Geoscience and Remote Sensing Symposium (IGARSS), 2011 IEEE International* , vol., no., pp.4213,4216, 24-29 July 2011
doi: 10.1109/IGARSS.2011.6050160

Ramos-Perez, I.; **Forte, G.**; Bosch-Lluis, X.; Camps, A.; Valencia, E.; Rodriguez-Alvarez, N.; Park, H.; Vall-llossera, M., "First results of the PAU-SA synthetic aperture radiometer," *Geoscience and Remote Sensing Symposium (IGARSS), 2011 IEEE International* , vol., no., pp.3633,3636, 24-29 July 2011
doi: 10.1109/IGARSS.2011.6050011

Ramos-Perez, I.; **Forte, G.**; Camps, A.; Bosch-Lluis, X.; Rodriguez-Alvarez, N.; Valencia, E.; Park, H.; Vall-llossera, M., "Validation and experimental tests of the PAU-synthetic aperture radiometer," *Geoscience and Remote Sensing Symposium (IGARSS), 2012 IEEE International* , vol., no., pp.4656,4659, 22-27 July 2012
doi: 10.1109/IGARSS.2012.6350427

Camps, A.; **Forte, G.**; Ramos, I.; Alonso, A.; Martinez, P.; Crespo, L.; Alcayde, A., "Recent advances in land monitoring using GNSS-R techniques," *Reflectometry Using GNSS and Other Signals of Opportunity (GNSS+R), 2012 Workshop on* , vol., no., pp.1,4, 10-11 Oct. 2012
doi: 10.1109/GNSSR.2012.6408255

Alonso-Arroyo, A.; **Forte, G.**; Camps, A.; Park, Hyuk; Pascual, D.; Onrubia R.; Jove, R., "Soil moisture mapping using forward scattered GPS L1 signals," *Geoscience and Remote Sensing Symposium (IGARSS), 2013 IEEE International* , vol., no., pp.843,846, 21-26 July 2013

Depau, V.; Tarongi, J. M.; **Forte, G.F.**; Camps, A., "Preliminary performance study of different radio-frequency interference detection and mitigation algorithms in microwave radiometry," *Microwave Radiometry and Remote Sensing of the Environment (MicroRad), 2012 12th Specialist Meeting on* , vol., no., pp.1,4, 5-9 March 2012
doi: 10.1109/MicroRad.2012.6185257

Camps, A.; Rodriguez-Alvarez, N.; Valencia, E.; **Forte, G.**; Ramos, I.; Alonso-Arroyo, A.; Bosch-Lluis, X., "Land monitoring using GNSS-R techniques: A review of recent advances," *Geoscience and Remote Sensing Symposium (IGARSS), 2013 IEEE International* , vol., no., pp.4026,4029, 21-26 July 2013
doi: 10.1109/IGARSS.2013.6723716

Carreno-Luengo, H.; Camps, A.; Perez-Ramos, I.; **Forte, G.**; Onrubia, R.; Diez, R., "^{3}Cat-2: A P(Y) and C/A GNSS-R experimental nano-satellite mission," *Geoscience and Remote Sensing Symposium (IGARSS), 2013 IEEE International* , vol., no., pp.843,846, 21-26 July 2013
doi: 10.1109/IGARSS.2013.6721290

Ramos-Perez, I.; Bosch-Lluis, X.; Camps, A.; Valencia, E.; Rodriguez-Alvarez, N.; Vall-llossera, M.; **Forte, G.**, "On-ground tests and measurements of the Passive Advanced Unit Synthetic Aperture (PAU-SA)," *Geoscience and Remote Sensing Symposium (IGARSS), 2010 IEEE International* , vol., no., pp.3114,3117, 25-30 July 2010
doi: 10.1109/IGARSS.2010.5649195

FORTHCOMING 2014

J. Querol, **G. F. Forte**, A. Camps, "Study of RFI Signals in Protected GNSS Bands generated by common electronic devices", *Geoscience and Remote Sensing Symposium (IGARSS), 2014 IEEE International. Forthcoming 2014.*

Alonso-Arroyo, A.; Camps, A.; Monerris, A.; Rüdiger, C.; Walker, J.; **Forte**, **G.;** Pascual, D.; Park, H.; Onrubia, R., "The Dual-Polarization GNSS-R Interference Pattern Technique", *Geoscience and Remote Sensing Symposium (IGARSS), 2014 IEEE International. Forthcoming 2014.*

Alonso-Arroyo, A.; Camps, A.; Monerris, A.; Rüdiger, C.; Walker, J.; **Forte**, **G.;** Pascual, D.; Park, H.; Onrubia, R., "The Light Airborne Reflectometer For GNSS-R Observations (Largo) Instrument: Results From Airborne And Rover Field Campaigns", *Geoscience and Remote Sensing Symposium (IGARSS), 2014 IEEE International. Forthcoming 2014.*

Camps, A.; Marchan-Hernandez, J.; Bosch-Lluis, X.; Rodriguez-Alvarez, N.; Ramos-Perez, I.; Valencia, E.; Tarongi, J.; Park, H.; Carreno-Luengo, H.; Alonso-Arroyo, A.; Pascual, D.; Onrubia, R.; **Forte**, **G.;** Querol, J., "Review of GNSS-R Instruments and Tools Developed at the Universitat Politecnica de Catalunya-Barcelona Tech", *Geoscience and Remote Sensing Symposium (IGARSS), 2014 IEEE International. Forthcoming 2014.*

Carreno-Luengo, H.; Camps, A.; Querol, J.; **Forte**, **G.;** Onrubia, R.; Díez, R., "A Stratospheric Balloon GNSS-R Experiment: The 3CAT-2 Project In DLR/SNSB BEXUS", *Geoscience and Remote Sensing Symposium (IGARSS), 2014 IEEE International. Forthcoming 2014.*

AUTHOR COPYRIGHT PERMISSIONS

The copyrighted material included in this dissertation is under permission of the authors: Phillip Ward and Jorge Querol. A reproduction of the permission letters are in the following pages.

April 1, 2014

Phil W. Ward

Dear Phil Ward:
I am completing a doctoral dissertation at Universitat Politècnica de Catalunya-Barcelona Tech (UPC) entitled "Contributions to Radio Frequency Interference Detection and Mitigation in Earth Observation." I would like your permission to reprint in my dissertation excerpts from the following:

> [43] P. W. Ward, "RFI Situational Awareness in GNSS Receivers: Design Techniques and Advantages," *Proceedings of the 63rd Annual Meeting of The Institute of Navigation*, Cambridge, MA, April 2007, pp. 189-197.

The excerpts to be reproduced are: [

The wide spreading of smartphones with GNSS capabilities and connected to the internet make them a great tool for detecting interferences, more specifically the ones affecting GNSS. Even though the individual measurements are of poor accuracy, the crowd consensus yields good accuracy. The concept is proposed in [43], and its feasibility is analyzed in [3], the explanation here is taken from those two references.

There are numerous advantages to RFI situational awareness in a GNSS receiver design. One unique advantage is that it provides the noise floor information required to perform an adaptive initial search and acquisition process. The design continues to operate even when the RFI level is so high that the GNSS receiver is incapable of acquiring and tracking satellites, an RFI situation that cannot be determined by most of today's GNSS receivers, even most military receivers. This robustness in RFI situational awareness measurement permits the GNSS receiver to inform the user that it will most likely be unable to acquire the signals and why. The jamming measurement is obtained by the measurement of the GNSS receiver RF front-end gain using measurements obtained from the automatic gain control (AGC). The preferred embodiment of the jamming meter is the digital gain control of the AGC. This gain control is derived from the analog-to-digital converter (ADC) process that normally occurs at the intermediate frequency (IF) of the GNSS receiver. In the absence of RFI, the AGC gain is set by the thermal noise power level (N). The digital value of N becomes the jamming reference level; not the GPS satellite signal power (S), which is well below N at the IF. When RFI occurs, the digital gain control acts to attenuate the gain of the AGC amplifier in order to keep the RMS amplitude of the AGC amplifier output at a constant level. That AGC operating point is normally selected to provide the least amount of quantization noise in the ADC that follows the AGC. In the presence of RFI, the new digital value is now a measure of the jamming power (J) plus N. This can be converted to a useful measure of the RFI level called the jamming-to-noise power ratio (J/N). Therefore, the AGC digital gain control reading can be a J/N meter as a natural by-product of the AGC gain control. The J/N meter technique works because the AGC control voltage does not change from the measurement of N unless an RFI is present at the IF. The gain of a modern AGC amplifier is linear in decibels (dB), so reading the AGC digital gain control value provides a precise linear measure in dB of the RFI power level, thus providing RFI situational awareness. An estimate of J/S can be made from this measurement assuming a uniform level of S for all satellites plus certain GNSS receiver front

end parameters. The estimation of J/S from the measure of J/N cannot account for differences in S for each satellite, but if the initial search fails and the J/N meter says that RFI is not the problem, and then the receiver can reasonably conclude that the GNSS signals must all be critically attenuated. When and if the receiver is tracking a subset of the GNSS constellation, it can accurately measure the carrier-to-noise power ratio in a 1 Hz noise bandwidth, $C/N_0 = S/N_0$, for each satellite being tracked. It can then estimate J/S more accurately for each satellite based on S/N_0 and certain GNSS receiver design parameters.

With this system, a solar event may trigger large numbers of phones, but the flat J/N versus location response can be used to rule out a localized jamming event. A real jamming event will tend to have a geographic center with many high J/N values over a fairly restricted area.]

The requested permission extends to any future revisions and editions of my dissertation, including non-exclusive world rights in all languages, and to the prospective publication of my dissertation by the Universitat Politècnica de Catalunya-Barcelona Tech, that may produce and sell copies of my dissertation on demand and may make my dissertation available for free internet download at my request. These rights will in no way restrict republication of the material in any other form by you or by others authorized by you. Your signing of this letter will also confirm that you own the copyright to the above-described material, or that you otherwise have sufficient rights to the material in order to grant the requested permission.

To grant this permission, please sign this letter where indicated below and return it to me a scanned copy. Please contact me should you have any questions or need additional information. I will contact Logan Scott because parts of the excerpts are from his publication. Thank you very much.

Sincerely,

Giuseppe Forte

PERMISSION GRANTED FOR THE USE REQUESTED ABOVE:

(For individuals): Logan N. Nash -or-

[Name of individual]

Date: 4/6/2014

(For companies)

[Name of company]

By: Navward GPS Consulting

Title: President

Date: 4/6/2014

March 31, 2014

Jorge Querol
Estimated Jorge Querol,

I am completing my doctoral dissertation at the Universitat Politècnica de Catalunya-Barcelona Tech entitled 'Contributions to Radio Frequency Interference Detection and Mitigation in Earth Observation'.

As the collaboration I made with you to produce your Master Thesis entitled "Implementation of Radio Frequency Interference Detection And Mitigation Algorithms For Communications And Navigation" I seek your permission to adapt and include it as a chapter in my dissertation.

The requested permission extends to the prospective publication of my dissertation by the Universitat Politècnica de Catalunya-Barcelona Tech in its digital archival repository, and other dissertation databases. The rights you provide me will in no way restrict your use of your work or by others authorized by you. Your signing of this letter will also confirm that you own the copyright to the above-described material.

If you are agreeable to this arrangement, I would be most grateful if you would please sign this letter below.

Best regards,

Giuseppe Forte

PERMISSION GRANTED FOR THE USE REQUESTED ABOVE:

(For individuals): JORGE QUEROL BORRAS
[Name of individual]
Date: 31/03/2014

-or-

(For companies)
[Name of company]
By: _____
Title: _____
Date: _____

BIBLIOGRAPHY

[1] "Handbook of Frequency Allocations and Spectrum Protection for Scientific Uses", Panel on Frequency Allocations and Spectrum Protection for Scientific Uses, Committee on Radio Frequencies, National Research Council, ISBN: 0-309-10301-0, 2007.

[2] M. Balch, "Complete Digital Design: A Comprehensive Guide to Digital Electronics and Computer System Architecture", McGraw Hill Professional, ISBN-13: 978-0071737708, pp. 413-417, Jun 20, 2003

[3] L. Scott, "J911: The Case for Fast Jammer Detection and Location Using Crowdsourcing Approaches," Proceedings of the 24th International Technical Meeting of The Satellite Division of the Institute of Navigation (ION GNSS 2011), Portland, OR, September 2011, pp. 1931-1940

[4] A. Broumandan, A. Jafarnia-Jahromi, V. Dehghanian, J. Nielsen, G. Lachapelle, , "GNSS spoofing detection in handheld receivers based on signal spatial correlation,"*Position Location and Navigation Symposium (PLANS), 2012 IEEE/ION* , vol., no., pp.479,487, 23-26 April 2012 doi: 10.1109/PLANS.2012.6236917

[5] SMOS Blog Centre d'Etudes Spatiales de la BIOsphere, http://www.cesbio.upstlse.fr/SMOS_blog/?p=233, last visited: 29 Nov. 2013.

[6] E. G. Njoku, P. Ashcroft, T. K. Chan, and L. Li, "Global survey and statistics of radio-frequency interference in AMSR-E land observations," *IEEE Trans. Geoscience. Remote Sens.*, vol. 43, no. 5, pp. 938–947, May 2005.

[7] S. W. Ellingson and J. T. Johnson, "A polarimetric survey of radiofrequency interference in C- and X-bands in the continental United States using WindSat radiometry," *IEEE Trans. Geoscience. Remote Sens.*, vol. 44, no. 3, pp. 540–548, Mar. 2006.

[8] M. Younis, J. Maurer, J. Fortuny-Guasch, R. Schneider,W.Wiesbeck, and A. J. Gasiewski, "Interference from 24-GHz automotive radars to passive microwave earth remote sensing satellites," *IEEE Trans. Geoscience. Remote Sens.*, vol. 42, no. 7, pp. 1387–1398, Jul. 2004.

[9] B. Güner, J. T. Johnson, and N. Niamsuwan, "Time and frequency blanking for radio frequency interference mitigation in microwave radiometry," *IEEE Trans. Geoscience. Remote Sens.*, vol. 45, no. 11, pp. 3672–3679, Nov. 2007.

[10] J. M. Tarongí, G. Forte, and A. Camps, "Experimental study of radio frequency interference detection algorithms in microwave radiometry," in *Proc. IEEE IGARSS*, Vancouver, BC, Canada, Jul. 24–29, 2011, pp. 4213–4216.

[11] J. M. Tarongí and A. Camps, "Radio frequency interference detection and mitigation algorithms based on spectrogram analysis," *Algorithms*, vol. 4, no. 4, pp. 239–261, Oct. 2011. [Online]. Available: http://www.mdpi.com/1999-4893/4/4/239

[12] S. Misra, P. N. Mohammed, B. Güner, C. S. Ruf, J. R. Piepmeier, and J. T. Johnson, "Microwave radiometer radio-frequency interference detection algorithms: A comparative study," *IEEE Trans. Geoscience. Remote Sens.*, vol. 47, no. 11, pp. 3742–3754, Nov. 2009.

[13] P. A. Fridman and W. A. Baan, "RFI mitigation methods in radio astronomy," *Astronomy. Astrophysics*, vol. 378, no. 1, pp. 327–344, Oct. 4, 2001.

[14] B. Winkel, J. Kerp, and S. Stanko, "RFI detection by automated feature extraction and statistical analysis," *Astronomische Nachrichten*, vol. 328, no. 1, pp. 68–79, Jan. 2007.

[15] A. R. Offringa, A. G. de Bruyn, M. Biehl, S. Zaroubi, G. Bernardi, and V. N. Pandey, "Post-correlation radio frequency interference classification methods," *Monthly Notices R. Astronomy. Soc.*, vol. 405, no. 1, pp. 155–167, Jun. 2010.

[16] C. M. Jarque and A. K. Bera, "A test for normality of observations and regression residuals," *Int. Stat. Rev.*, vol. 55, no. 2, pp. 163–172, Aug. 1987.

[17] C. M. Urzua, "On the correct use of omnibus tests for normality," *Economy. Letters*, vol. 53, no. 3, pp. 247–251, Dec. 1996.

[18] G. Poitras, "More on the correct use of omnibus tests for normality," *Economy. Letters*, vol. 90, no. 3, pp. 304–309, Mar. 2006.

[19] R. B. D'Agostino, A. Belanger, and R. B. D'Agostino, Jr., "A suggestion for using powerful and informative tests of normality," *Amer. Stat.*, vol. 44, no. 4, pp. 316–321, Nov. 1990.

[20] H. W. Lilliefors, "On the Kolmogorov–Smirnov test for normality with mean and variance unknown," *J. Amer. Stat. Assoc.*, vol. 62, no. 318, pp. 399–402, Jun. 1967.

[21] R. B. D'Agostino and M. A. Stephens, *Goodness-of-Fit Techniques*, 1st ed. New York, NY, USA: Marcel Dekker, 1986, pp. 122–133.

[22] A. Trujillo-Ortiz, AnDartest: Anderson–Darling test for assessing normality of a sample data, Apr. 27, 2007. [Online]. Available: http://www.mathworks.com/matlabcentral/fileexchange/14807-andartest, last visited: March 27, 2014.

[23] S. S. Shapiro and M. B. Wilk, "An analysis of variance test for normality (complete samples)," *Biometrika*, vol. 52, no. 3/4, pp. 591–611, Dec. 1965.

[24] J. P. Royston, "Approximating the Shapiro–Wilk W-test for non-normality," *Stat. Comput.*, vol. 2, no. 3, pp. 117–119, Sep. 1992.

[25] J. P. Royston, "An extension of Shapiro and Wilk'sWtest for normality to large samples," *J. R. Stat. Soc. Ser. C (Appl. Stat.)*, vol. 31, no. 2, pp. 115– 124, 1982.

[26] "Cramér–von Mises test," *Encyclopedia of Mathematics*. [Online]. Available: http://www.encyclopediaofmath.org/index.php?title=Cram%C3%A9r-von_Mises_test&oldid=26398, last visited: March 27, 2014.

[27] C. C. Lin and G. S. Mudholkar, “A simple test for normality against asymmetric alternatives,” *Biometrika*, vol. 67, no. 2, pp. 455–461, Aug. 1980.

[28] H. Tong, *Non-Linear Time Series: A Dynamical System Approach*, 1st ed. New York, NY, USA: Oxford Univ. Press, 1990, pp. 324–325.

[29] H. G. Thode Jr., *Testing for Normality*, 1st ed. New York, NY, USA: Marcel Dekker, 2002, pp. 88–89.

[30] Chi-Square Distribution. [Online]. Available: http://www.itl.nist.gov/div898/handbook/eda/section3/eda3666.htm, last visited: March 27, 2014.

[31] G.M. Nita and D.E. Gary, “Statistics of the Spectral Kurtosis Estimator,” Publications of the Astronomical Society of the Pacific, vol. 122, May. 2010, pp. 595-607

[32] S.S. Sobjaerg, J. Svoboda, J.E. Balling, N. Skou, "Detection of radio-frequency interference in microwave radiometers using spectral kurtosis," in *Proc. IEEE IGARSS*, Munich, Germany, Jul. 23–27, 2012, pp. 7141-7144

[33] R. D. De Roo and S. Misra, “Effectiveness of the sixth moment to eliminate a Kurtosis blind spot in the detection of interference in a radiometer,” in *Proc. IEEE IGARSS*, Boston, MA, USA, Jul. 7–11, 2008, vol. 2, pp. II-331–II-334.

[34] B. Guner, M. T. Frankford, and J. T. Johnson, “On the Shapiro–Wilk test for the detection of pulsed sinusoidal radio frequency interference,” in *Proc. IEEE IGARSS*, Boston, MA, USA, Jul. 7–11, 2008, vol. 2,pp. II-157–II-160.

[35] J.P. Royston, “An extension of Shapiro and Wilk’s W test for normality to large samples,” *Applied .Statistics 1982*, Vol. *31*, No. 2, pp. 115–124.

[36] J. M. Tarongi and A. Camps, “Normality analysis for RFI detection in microwave radiometry,” *Remote Sens.*, vol. 2, no. 1, pp. 191–210, Dec. 2009.

[37] A. Camps, J. Gourrion, J. M. Tarongí, M. Vall Llossera, A. Gutiérrez, J. Barbosa, and R. Castro, “Radio-frequency interference detection and mitigation algorithms for synthetic aperture radiometers,” *Algorithms*, vol. 4, no. 3, pp. 155–182, Aug. 2011.

[38] S. S. Kristensen, J. Balling, N. Skou, and S. S. Søbjærg, “RFI in SMOS data detected by polarimetry,” in *Proc. IEEE IGARSS*, Munich, Germany, Jul. 23–27, 2012, pp. 3320–3323.

[39] A. Camps and J. M. Tarongi, “RFI mitigation in microwave radiometry using wavelets,” *Algorithms*, vol. 2, no. 3, pp. 1248–1262, Sep. 2009.

[40] B. Widrow, J.R. Glover Jr., J.M. McCool, J. Kaunitz, C.S. Williams, R.H. Hearn, J.R. Zeidler, E. Dong Jr., R.C. Goodlin, "Adaptive noise cancelling: Principles and applications, "*Proceedings of the IEEE* , vol.63, no.12, pp. 1692- 1716, Dec. 1975

[41] C. Barnbaum and R. F. Bradley, "A New Approach to Interference Excision in Radio Astronomy: Real-Time Adaptive Cancellation", The Astronomical Journal, Vol. 116(5), pp. 2598-2614, Nov. 1998.

[42] Novatel GAJT Anti-Jam Antenna. [Online]. Available: http://www.novatel.com/products/gnss-antennas/gajt/#contentTab1, last visited: March 27, 2014.

[43] A. Leshem, A.J. van der Veen, and A.J. Boonstra, "Multichannel interference mitigation techniques in radio astronomy", Astrophysical Journal Supplements, Vol. 131(1), pp. 355-374, Nov. 2000.

[44] S. Misra, C. S. Ruf, "Analysis of Radio Frequency Interference Detection Algorithms in the Angular Domain for SMOS," Geoscience *and Remote Sensing, IEEE Transactions on*, Vol. 49(12), pp. 1-10, Dec. 2011.

[45] P. W. Ward, "RFI Situational Awareness in GNSS Receivers: Design Techniques and Advantages," *Proceedings of the 63rd Annual Meeting of The Institute of Navigation*, Cambridge, MA, April 2007, pp. 189-197.

[46] J. Querol, Implementation of Radio Frequency Interference Detection and Mitigation Algorithms for Communications and Navigation. Master thesis, Universitat Politècnica de Catalunya, Barcelona Tech, 2013.

[47] T. Kraus, R. Bauernfeind and B. Eissfeller. "Survey of in-car jammers – analysis and modelling of the RF signals and IF samples (suitable for active signal cancelation)", Proceedings of the 24th International Technical Meeting of The Satellite Division of the Institute of Navigation ION/ GNSS, pages 430-435, Portland, OR. 2011

[48] R.H. Mitch, R.C. Dougherty, M.L. Psiaki, S.P. Powell, B.W. O'Hanlon, J.A. Bhatti, and T.E. Humphreys. "Signal characteristics of civil GPS jammers", Proceedings of the 24th International Technical Meeting of The Satellite Division of the Institute of Navigation (ION/GNSS), pages 1907-1919, Portland, OR. 2011

[49] S. Pullen, and G. Gao. "GNSS jamming in the name of privacy", Inside GNSS, March-April 2012 volume, pages 34-43

[50] The Economist. GPS jamming: No jamming tomorrow. Technology Quarterly, March 2011.

[51] C. Smith, D. Collins. "3G Wireless Networks", page 136. McGraw-Hill Osborne Media; second edition (November 16, 2006). ISBN-13: 978-0072263442

[52] W. Nethercot, "Car-ignition interference," Wireless Eng., p. 25 1, Aug. 1949.

C. C. Eaglesfield, "Car ignition radiation," Wireless Eng., p. 17, Jan. 1951.

[53] G. F. Newell, "Ignition interference at frequencies below 100 Mc/s: The mechanism of its production," B.B.C. Quarterly, vol. 9, p. 175, Aug. 1954.

[54] R. R. Burgett, R. E. Massoll, and D. R. Van Uum, "Relationship between spark plugs and engine-radiated electromagnetic interference," IEEE Trans. EMC, vol. 16, Aug. 1974.

[55] R. A. Shepherd, J. C. Gaddie, and D. L. Nielson, "New techniques for suppression of automobile ignition noise," IEEE Trans. VTG, vol. 25, p. 2, Feb. 1976.

[56] H. P. Hsu and D. C. Schlick, “Effect of distributor gap on radiated ignition interference,” 1969 EMC Symposium. Rec., p. 319, June 1969.

[57] J. Thomson, “The influence of charged metallic points on the spark discharge,” Phil. Mag., S. 7, vol. 5, p. 5313, Mar. 192

[58] Ellingson, S.W.; Hampson, G.A.; Johnson, J.T.; "Design of an L-band microwave radiometer with active mitigation of interference," Geoscience and Remote Sensing Symposium, 2003. IGARSS '03 Proceedings. 2003 IEEE International, vol.3, no., pp. 1751- 1753, 21-25 July 2003

[59] Niamsuwan N., Johnson J. T., and Ellingson S. W., “Examination of a simple pulse blanking technique for RFI mitigation” Radio Science, vol. 40, June 2005.

[60] Johnson, J.T.; Potter, L.C.; "Performance Study of Algorithms for Detecting Pulsed Sinusoidal Interference in Microwave Radiometry," IEEE Transactions Geoscience and Remote Sensing, vol.47, no.2, pp.628-636, Feb. 2009

[61] De Roo, R.D.; Misra, S..; Ruf, C.S.; "Sensitivity of the Kurtosis Statistic as a Detector of Pulsed Sinusoidal RFI," IEEE Transactions on Geoscience and Remote Sensing, vol.45, no.7, pp.1938-1946, July 2007

[62] G. F. Forte, A. Camps, J. M. Tarongi, and M. Vall-llossera, “Study of radio frequency interference effects on radiometry bands in urban environments,” in Proc. IEEE IGARSS, Jul. 22–27, 2012, pp. 1069–1072.

[63] Camps, A.; Font, J.; Vall-llossera, M.; Gabarro, C.; Corbella, I.; Duffo, N.; Torres, F.; Blanch, S.; Aguasca, A.; Villarino, R.; Enrique, L.; Miranda, J.J.; Arenas, J.J.; Julia, A.; Etcheto, J.; Caselles, V.; Weill, A.; Boutin, J.; Contardo, S.; Niclos, R.; Rivas, R.; Reising, S.C.; Wursteisen, P.; Berger, M.; Martin-Neira, M.; , "The WISE 2000 and 2001 field experiments in support of the SMOS mission: sea surface L-band brightness temperature observations and their application to sea surface salinity retrieval," Geoscience and Remote Sensing, IEEE Transactions on , vol.42, no.4, pp. 804- 823, April 2004

[64] Villarino, R.; Fernandez, J.; Camps, A.; Vall-llossera, M.; Corbella, I.; Duffo, N.; Torres, F.; , "Design and test of the L-band automatic radiometer (LAURA) temperature control," *Geoscience and Remote Sensing Symposium, 2005. IGARSS '05. Proceedings 2005 IEEE International*, vol.7, pp. 4902- 4905, 25-29 July 2005

[65] Cardellach, E.; Rius, A.; Cerezo, F.; Garcia-Primo, M.A.; de la Torre-Juarez, M.; Cucurull, L.; Ector, D.; , "Polarimetric GNSS Radio-Occultations for heavy rain detection," *Geoscience and Remote Sensing Symposium (IGARSS), 2010 IEEE International* , pp.3841-3844, 25-30 July 2010

[66] O. Nogués-Correig, E. Cardellach Galí, J. Sanz Campderròs, and A. Rius. “A GPS-Reflections Receiver That Computes Doppler/Delay Maps in Real Time”. *IEEE Transactions on Geoscience Remote Sensing*, 45(1):156-174, January 2007.

[67] Spanish National Frequency Allocation Table (last visited April 22, 2014) http://www.minetur.gob.es/telecomunicaciones/espectro/paginas/cnaf.aspx

[68] J.F. Kenney and E.S. Keeping, "Kurtosis," in Mathematics of Statistics, 3rd ed. Princeton, NJ: Van Nostrand, 1962, ch. 1, Sec. 7.12, pp. 102-103

[69] J. Querol, G. F. Forte, A. Camps, "Study of RFI Signals in Protected GNSS Bands generated by common electronic devices", *Geoscience and Remote Sensing Symposium (IGARSS), 2014 IEEE International. Forthcoming 2014.*

[70] J.S. Walker, A Primer on Wavelets and Their Scientific Applications, 2nd ed.; Chapman & Hall/CRC: Boca Raton, FL, USA, 2008: Chapters 1-2.

[71] G.F**.** Forte, J. Querol, A. Camps, M. Vall-llossera, "Real-Time RFI Detection and Mitigation System for Microwave Radiometers," *IEEE Transactions on Geoscience and Remote Sensing*, vol.51, no.10, pp.4928-4935, Oct. 2013

doi: 10.1109/TGRS.2013.2267595

[72] MATLAB tutorial on denoising (Last visited January 21th, 2014): http://www.mathworks.com/access/helpdesk/help/toolbox/wavelet/index.html?/access/helpdesk/help/toolbox/wavelet/ch06_a12.html

[73] D. L. Donoho, I. M. Johnstone. "Adapting to Unknown Smoothness via Wavelet Shrinkage". *Journal of the American Statistical Association* (Journal of the American Statistical Association (December 1995), Vol.90, No.432) pp. 1200-1244. doi:10.2307/2291512. JSTOR 2291512.

[74] G.F. Forte, J. Querol, H. Park, A. Camps, "Digital back-end for RFI detection and mitigation in earth observation," *Geoscience and Remote Sensing Symposium (IGARSS), 2013 IEEE International*, vol., no., pp.1908,1911, 21-26 July 2013

doi:10.1109/IGARSS.2013.6723177

[75] G.F. Forte, A. Camps, I. Ramos, M. Vall-llossera, "Digital back-end for RFI detection and mitigation in microwave radiometers," *Geoscience and Remote Sensing Symposium (IGARSS), 2012 IEEE International* , vol., no., pp.2953-2955, 22-27 July 2012
doi: 10.1109/IGARSS.2012.6350706

[76] A. Thiel and M. Ammann, "Anti-Jamming techniques in u-blox GPS receivers," White paper, 2009.

[77] R. Rifkin and J. Vaccaro, "Comparison of narrowband adaptive filter technologies for GPS," in IEEE Position Location and Navigation Symposium, 2000, pp. 125,131.

[78] A. Kandangath, "Jamming Mitigation Techniques for Spread Spectrum Communication Systems," 2000.

[79] H. Poor, "An Introduction to Signal Detection and Estimation." Springer Texts in Electrical Engineering, Springer, 2010.

[80] J. Tarongí, Radio Frequency Interference in Microwave Radiometry: Statistical Analysis and Study of Techniques for Detection and Mitigation. PhD thesis, Universitat Politècnica de Catalunya, BarcelonaTech, 2012.

http://www.tdx.cat/bitstream/handle/10803/117023/TJTB1de1.pdf?sequence=1

[81] S. Mallat, A Wavelet Tour of Signal Processing. Wavelet Tour of Signal Processing, Elsevier Science, 1999.

[82] A. Oppenheim and R. Schafer, Discrete-time signal processing. Prentice-Hall signal processing series, Prentice Hall, 2010.

[83] R. Crochiere and L. Rabiner, Multirate digital signal processing. Prentice-Hall Signal Processing Series, Prentice Hall PTR, 1983.

[84] D. Manolakis, V. Ingle, and S. Kogon, Statistical and Adaptive Signal Processing: Spectral Estimation, Signal Modelling, Adaptive Filtering, and Array Processing. The Artech House Signal Processing Library, Artech House, Nordwood, MA, 2000.

[85] I. Pitas and A. Venetsanopoulos, Nonlinear Digital Filters: Principles and Applications. Kluwer international series in engineering and computer science: VLSI, computer architecture, and digital signal processing, Springer, 1990.

[86] E. Valencia, A. Camps, X. Bosch-Lluis, N. Rodriguez-Alvarez, I. Ramos-Perez, F. Eugenio and J. Marcello, "On the Use of GNSS-R Data to Correct L-Band Brightness Temperatures for Sea-State Effects: Results of the ALBATROSS Field Experiments", IEEE Transactions on Geoscience and Remote Sensing, vol.49, no.9, pp.3225,3235, Sept. 2011

doi: 10.1109/TGRS.2011.2159224

[87] A. Rius, O. Nogues-Correig, S. Ribo et al., “Altimetry with GNSS-R interferometry: first proof of concept experiment”, GPS Solutions, vol. 16, Issue 2, pp. 231-241, April 2012.

[88] Universitat Politècnica de Catalunya, Antenna Anechoic Chamber www.tsc.upc.edu/antennalab

[89] Camps, A.; Forte, G.; Ramos, I.; Alonso, A.; Martinez, P.; Crespo, L.; Alcayde, A., "Recent advances in land monitoring using GNSS-R techniques," *Reflectometry Using GNSS and Other Signals of Opportunity (GNSS+R), 2012 Workshop on* , vol., no., pp.1,4, 10-11 Oct. 2012
doi: 10.1109/GNSSR.2012.6408255

[90] Darrera 3R KWS Heated Anemometer http://www.darrera.com/detalle-producto.php?d=1&id=68

[91] J. M. Tarongi and A. Camps, "Multifequency Experimental Radiometer with Interference Tracking for Experiments over Land and Littoral: MERITXELL", International Geoscience and Remote Sensing Symposium IGARSS 2009, pp. IV-653-IV-656, Cape Town, South Africa, 13-17 Jul. 2009.

[92] D. W. Allan, “Statistics of Atomic Frequency Standards.” Proc. IEEE, vol 54, No.2, Feb. 1966, pp. 221-230.

[93] Tangreat GPS Jammer http://www.tangreat.com/en/product-detail-60.html

LIST OF ACRONYMS

AC	Alternating Current
ADC	Analog to Digital converter
AGC	Automatic Gain Control
BPF	Band Pass Filter
BUFG	Global Clock Buffer
BUFGCTRL	Global Clock Control Buffer
C/A	Coarse/Acquisition
CDMA	Code Division Multiple Access
DC	Direct Current
DOA	Direction of Arrival
DSP	Digital Signal Processor
EMI	Electro Magnetic Interference
FF	Flip Flop
FIR	Finite Impulse Response
FMC	FPGA Mezzanine Card
FPGA	Field Programmable Gate Array
GBAS	Ground Based Augmentation System
GLONASS	Global'naya Navigatsionnaya Sputnikovaya Sistema
GNSS	Global Navigation Satellite System
GPS	Global Positioning System
GSM	Global System for Mobile Communications
IF	Intermediate Frequency
IIR	Infinite Impulse Response
INR	Interference to Noise Ratio
IOB	Input Output Block
IQ	In-phase and Quadrature
ISR	Interference to Signal Ratio

JNR	Jamming to Noise Ratio
KS	Kilo Samples
LHCP	Left Hand Circular Polarization
LO	Local Oscillator
LUT	Look Up Table
MAD	Median Absolute Deviation Mb Megabits
MCB	Magnetic Circuit Breaker
MERITXELL	Multi-frequency Experimental Radiometer with Interference Tracking for eXpEriments over Land and the Littoral
P	Precision
PIC	Peripheral Interface Controller
PNT	Position, Navigation and Timing
PPD	Personal Privacy Device
R_b	Resolution Bandwidth
RFI	Radio Frequency Interference
RHCP	Right Hand Circular Polarization
RMS	Root Mean Square
SIR	Signal to Interference Ratio
STFT	Short Time Fourier Transform
SURE	Stein's Unbiased Risk Estimate
TPR	Total Power Radiometer
USB	Universal Serial Bus
WOL	Wake on Local Area Network